Technical University of Denmark

DTU

Wind tunnel tests of the NACA 63-415 and a modified NACA 63-415 airfoil

Bak, Christian; Fuglsang, P.; Johansen, J.; Antoniou, I.

Link back to DTU Orbit

DTU Library
Technical Information Center of Denmark

Wind Tunnel Tests of the NACA 63-415 and a Modified NACA 63-415 Airfoil

Christian Bak, Peter Fuglsang, Jeppe Johansen, Ioannis Antoniou

Abstract

This report contains 2D measurements of the NACA 63-415 and a NACA 63-415 airfoil with modified leading edge called NACA 63-415-Risø-D. The aerodynamic properties were derived from pressure measurements on the airfoil surface and in the wake. The VELUX open jet wind tunnel was used having a background turbulence intensity of 1%, an inlet flow velocity of 40 m/s which resulted in a Reynolds number of 1.6×10^6. The airfoil sections had a chord of 0.600 m and 0.606 m for NACA 63-415 and NACA 63-415-Risø-D, respectively. The span was 1.9 m and end plates were used to minimise 3D flow effects. The measurements comprised both static and dynamic inflow where dynamic inflow was obtained by pitching the airfoil in a harmonic motion. We tested the influence of leading edge roughness, stall strips and vortex generators.

For smooth surface conditions the modified airfoil showed an increase in lift-drag ratio before stall at $\alpha=8°$ from 67 to 72. Furthermore, the maximum lift increased from 1.33 to 1.37 while the minimum drag was maintained. Double stall was observed on the NACA 63-415 airfoil, but not on the modified airfoil. This was reflected in the standard deviation of both lift and drag in stall which was significantly lower for the modified airfoil indicating smooth and stable stall conditions. No significant differences were observed for dynamic stall. Test on both airfoil sections with zigzag tape at the leading edge towards the pressure side showed that the insensitivity to roughness was improved significantly for the modified airfoil. However, if zigzag tape was mounted at the leading edge towards the suction side less improvement was observed. Mounting of stall strips at and near the leading edge showed that only if they were mounted at the very vicinity of the leading edge the airfoil characteristics were affected significantly. If the stall strips were mounted on the pressure side downstream of approximately 1 % chord length only little influence was seen for positive angles of attack.

Contents

Nomenclature

c	[m]	Airfoil chord
h	[m]	Jet height
k		Reduced frequency
Δp	[Pa/m]	Pressure loss
p	[Pa]	Static pressure
p_o	[Pa]	Total pressure head
q	[Pa]	Dynamic pressure
s		Airfoil surface co-ordinate
t	[s]	Pitch motion time
x		Co-ordinate in chord direction
y		Wake rake vertical co-ordinate, airfoil vertical co-ordinate

A	[°]	Pitch motion amplitude
C_D		Drag coefficient
C_L		Lift coefficient
C_M		Moment coefficient
C_N		Normal force coefficient
C_P		Airfoil pressure coefficient
C_T		Tangential force coefficient
Re		Reynolds number
T	[°C]	Air temperature
V	[m/s]	Velocity

α	[rad] [°]	Angle of attack
ε		Speed-up factor
ρ	[kg/m^3]	Air density
ω	[rad/s]	Pitch motion angular velocity

Subscripts

1-3	Pitot tube measurement
a	Airfoil section measurement
atm	Atmospheric value
j	Jet outlet measurement
m	Mean value
min	Minimum value
max	Maximum value
p	Pressure measurement
t	Measured value (uncorrected)
w	Wake rake measurement
∞	Free stream reference for normalisation of airfoil forces

1 Summary of results

Measurements of C_L and C_D for NACA 63-415 and NACA 63-415 with modified leading edge, NACA 63-415-Risø-D, were carried out in the *VELUX* wind tunnel. For smooth surface conditions, leading edge roughness on suction side and leading edge roughness on pressure side results are shown in Figure 1-1, Figure 1-2 and Figure 1-3, respectively.

The two airfoils have very similar characteristics at smooth surface conditions. However, from $\alpha = 6°$ C_L is higher and C_D is slightly lower for the modified airfoil. Furthermore, the modified airfoil does not show double stall in contrast to the NACA 63-415 airfoil where double stall is observed at $\alpha = 20.7°$.

With leading edge roughness at the suction side C_L is lower and C_D is higher compared to the smooth airfoils. However, the driving force, C_T, is up to 8% higher for the modified airfoil than for the NACA 63-415 airfoil until $\alpha = 15°$. For $\alpha > 15°$ C_T is lower for the modified airfoil. With leading edge roughness at the pressure side C_L is significantly higher and C_D is significantly lower for all angles of attack for the modified airfoil compared with the NACA 63-415 airfoil. This resulted in an increase of the maximum driving force coefficient for the modified airfoil of 40% compared to the NACA 63-415. Thus, the modified airfoil is more insensitive to leading edge roughness.
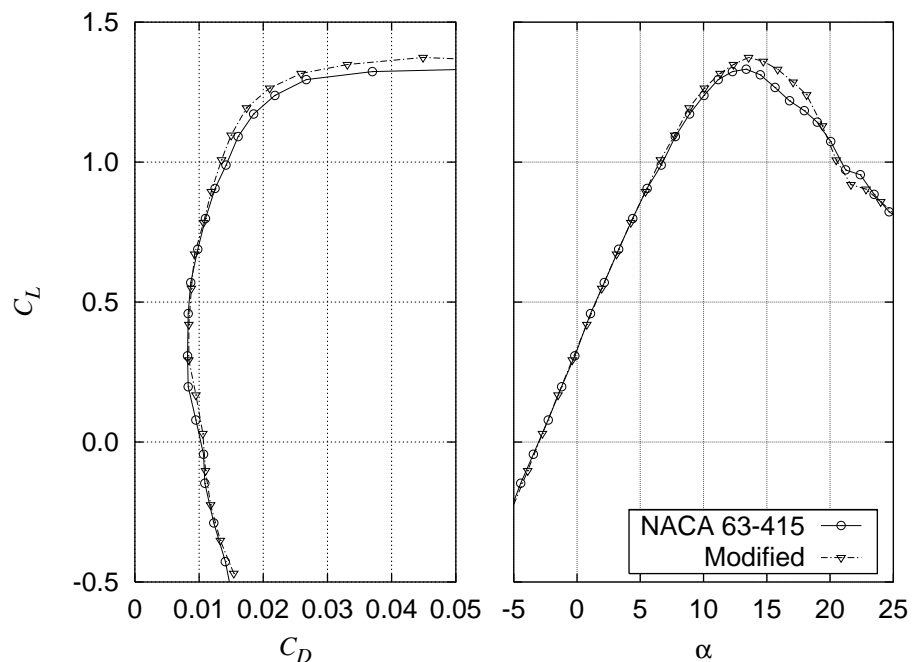
Figure 1-1 C_L,-C_D for NACA 63-415 and NACA 63-415-Risø-D with smooth surface.
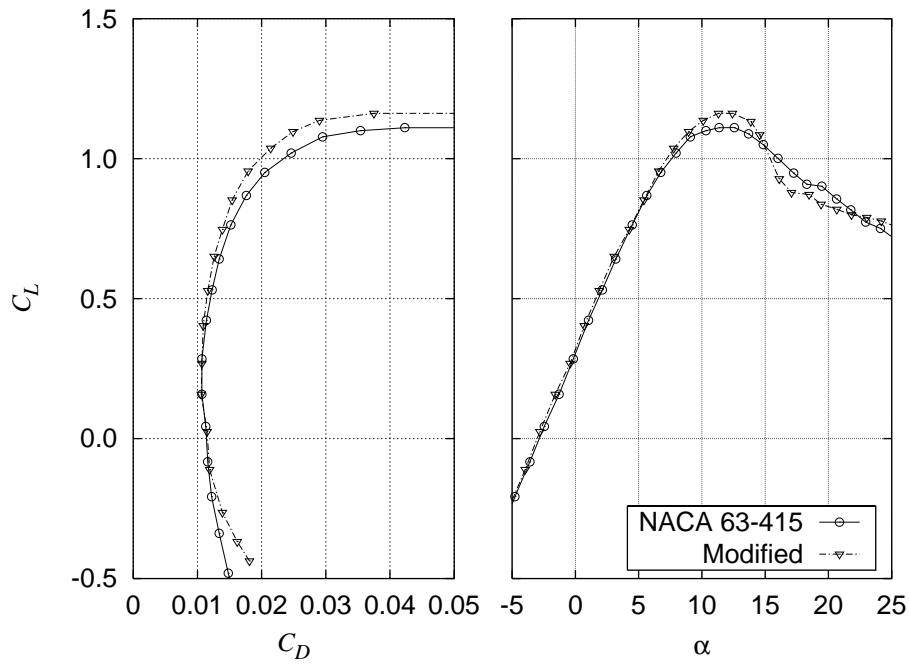
Figure 1-2 C_L-C_D for NACA 63-415 and NACA 63-415-Risø-D with LER at the suction side.
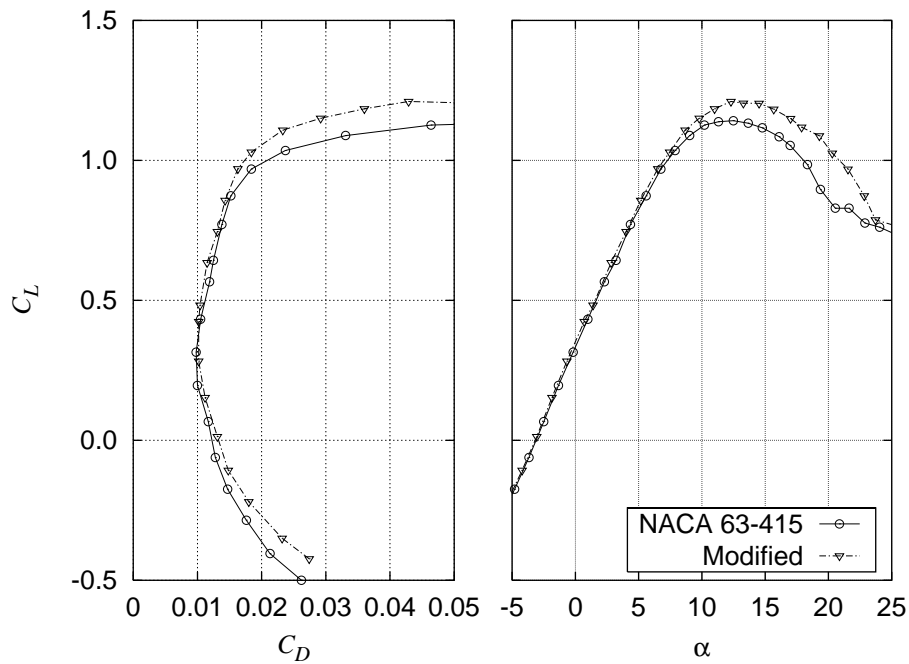
Figure 1-3 C_L-C_D for NACA 63-415 and NACA 63-415-Risø-D with LER at the pressure side.

1.1 Conclusions in summary

- For smooth surface conditions the modified airfoil had the characteristics as described in the design objectives compared to the NACA 63-415 airfoil:
  - higher lift-drag ratio from $\alpha = 6°$ (at $\alpha = 8°$ the lift-drag ratio increased from 67 to 72)
  - no double stall was observed in contrast to the NACA 63-415 airfoil,

- the maximum lift coefficient for the modified airfoil was increased from 1.33 to 1.37,
- the minimum drag coefficient was 0.008 for both airfoils.
- With leading edge roughness the following was observed:
  - with 90° zigzag tape of 0.35 mm thickness:
    - mounted at 5 % and 10 % chord length at the suction side and pressure side, respectively, only very little influence was observed compared to smooth conditions for both airfoils,
    - located on the pressure side leading edge the modified airfoil had improved the roughness insensitivity significantly (the maximum driving force coefficient showed an increase of 40 %),
    - located on the suction side leading edge the modified airfoil had improved the roughness insensitivity up to 15° angles of attack (the maximum driving force coefficient showed an increase of 5 %),
- In dynamic stall experiments the following was observed:
  - at 16°, 18° and 20° angles of attack the slope of the loops and the opening of the loops changed slightly for C_D and C_M,
  - the directions of the loops changed for C_D at 16° and 20°,
  - in general the dynamic stall characteristics for the two airfoils did not change.
- In static stall experiments the following was observed:
  - lower standard deviations for the modified airfoil for both C_L and C_D was observed indicating smoother and more stable stall conditions for the modified airfoil,
  - double stall was avoided for the modified airfoil.
- With stall strips mounted on the NACA 63-415 airfoil the following was observed:
  - the biggest reduction in maximum lift and the biggest increase in minimum drag were obtained if the stall strips were located around the very leading edge corresponding to stagnation points for –2°, 0° and 2° angles of attack,
  - locating the stall strips at the stagnation point for -2° angles of attack most significantly affected the aerodynamic coefficients,
  - the airfoil characteristics had a strong dependency of the exact location of the stall strips at the leading edge,
  - minor influence was seen if stall strips were mounted at the stagnation point for 6° angles of attack,
  - the effect of stall strips could be neglected when located at the stagnation point for 10° angles of attack and above if only positive angles of attack were considered.
- With vortex generators mounted at 20 % chord length at the suction side of the NACA 63-415 airfoil the following was observed:
  - significant increase of $C_{L,max}$ from 1.33 at 13° angles of attack without vortex generators to 1.74 at 18° angles of attack with vortex generators,
  - $C_{L,max}$ was followed by an abrupt loss of C_L, so that C_L for the airfoil with and without vortex generators was similar for angles of attack above 20°,
  - the presence of the vortex generators increased the drag for low angles of attack until 12°.

2 Introduction

This report concerns 2D wind tunnel measurements of the NACA 63-415 airfoil and a NACA 63-415 airfoil with modified leading edge called NACA 63-415-Risø-D. The NACA 63-415 airfoil described by Abbott and Doenhoff [1] is frequently used on wind turbine blades. For stall regulated wind turbines the stall characteristics are very important. To improve the stall characteristics the leading edge was modified resulting in the NACA 63-415-Risø-D airfoil described by Fuglsang and Bak [2]. The operational design Reynolds number for the modified airfoil is Re = 3.0 million. All tests were carried out at the highest possible Reynolds number of 1.6 million. The measurements were carried out in the VELUX wind tunnel, which has an inlet test section with a background turbulence level of 1% and a maximum flow velocity of 40 m/s. The angle of attack range was between -5° and 30°. Pressure distributions were measured on the airfoil section and in the wake. The testing facility is described in detail by Fuglsang *et al.* [3].

The test matrix included:
- Steady and quasi-steady inflow measurements where mean values were obtained for the airfoil aerodynamic coefficients. During quasi-steady measurements the angle of attack was changed continuously at an average rate around 0.1°/s to 0.5°/s. During steady inflow conditions the angle of attack was changed in steps of 2° and a 20 s duration time series was obtained for each angle of attack. Furthermore, measurements with the angle of attack fixed were performed for either 1 minute or 3 minutes typically at high angles of attack.
- Dynamic inflow measurements with the airfoil in pitching motion at amplitudes of ±2° around a certain mean pitch angle and reduced frequencies around 0.1. The hysteresis effects on the aerodynamic coefficients were derived.

The airfoils were tested under the following surface configurations:
- Smooth surface referred to as, 'smooth flow'.
- Leading edge roughness to simulate the change of the aerodynamic coefficients from dirt and dust accumulation referred to as, 'LER'.
- Stall strips at the leading edge, referred to as, 'SS'
- Vortex generators on the suction side referred to as, 'VG'

3 Experimental set-up

The experimental set-up is briefly described in this chapter. A more complete description can be found in Fuglsang *et al.* [3].

3.1 Testing facility

The VELUX wind tunnel is of the closed return type with an open test section with a cross section of 7.5×7.5 m and a length of 10.5 m, Figure 3-1. The cross section of the jet blowing into the test section is 3.4×3.4 m. The maximum flow velocity is 42 m/s.
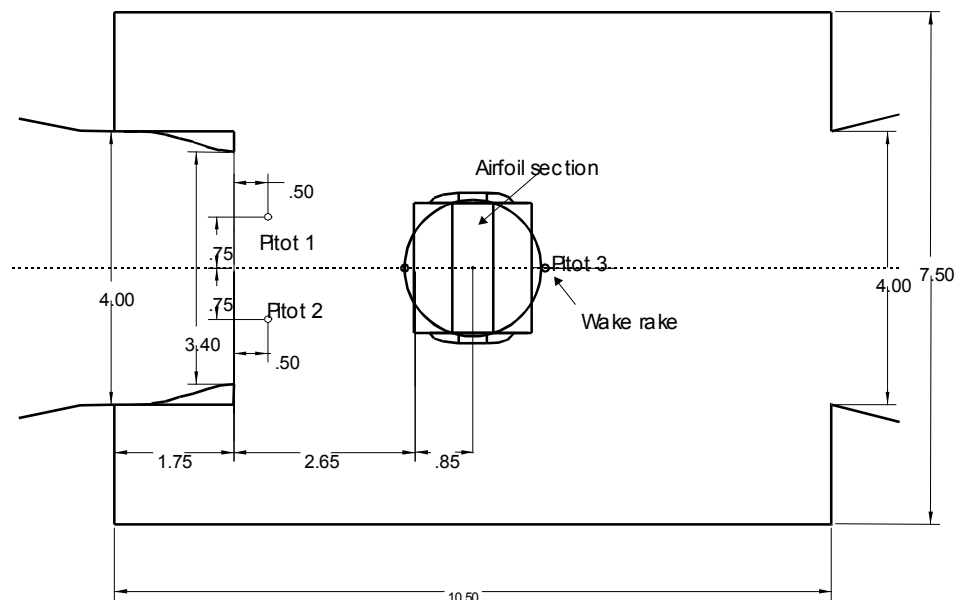

Figure 3-1 The wind tunnel test section with the test stand seen in a top view. with the flow coming from the left.

A test stand was built for 2D airfoil testing, Figure 3-2. The test stand was inserted in the tunnel test section. The airfoil section with a span of 1.9 m and a chord of 0.6 m was mounted 1.7 m from the tunnel floor and 3.2 m from the nozzle outlet. End plates were fixed to the stand at the ends of the airfoil section to limit 3d effects.

Three Pitot tubes measured static and total pressure at different locations in the test section, Figure 3-1. These Pitot tubes were used to measure the wind tunnel reference pressures and to estimate the turbulence level and the stability of the wind tunnel flow.

Quasi-steady measurements at continuously varying angles of attack as well as dynamic inflow measurements were possible. Dynamic inflow was obtained by pitching the airfoil section at different reduced frequencies up to $k = 0.15$ and amplitudes between $\pm1° < A < \pm5°$ with the pitch axis located at $x/c = 0.40$, see section 2.4.
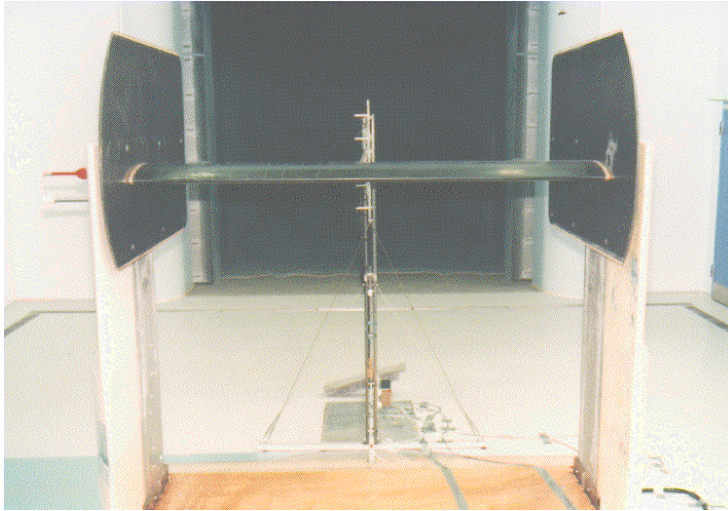
Figure 3-2 The test section with the test stand and the wake rake downstream of the airfoil section.

The wake rake consisted of 53 total pressure probes and five static tubes. The vertical span was 0.456 m, Figure 3-3. The distance between the airfoil trailing edge and the wake rake was 0.7 airfoil chords and the centre of the wake rake was placed at the height of the trailing edge at 0° incidence and behind the centre line of the airfoil section. The rake was not traversed in the horizontal or the vertical directions.
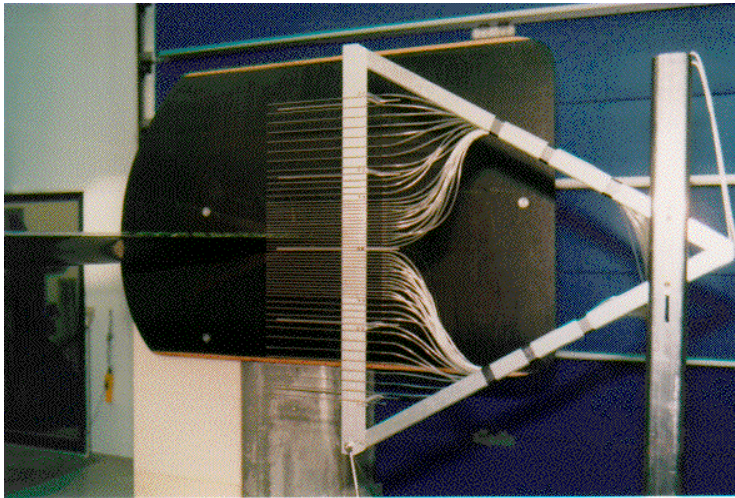
Figure 3-3 The wake rake seen from the side in front of an endplate.

The HyScan 2000 data acquisition system from Scanivalve Corp. was used. Two ZOC33 pressure-scanning modules recorded the pressure signals. For the airfoil surface pressures, 40 1psi and 24 2.5psi range sensors were used. For the wake rake and the Pitot tubes, 10´´ H_2O sensors were used. The ZOC module for the airfoil pressures was mounted on the test stand side just outside the airfoil section. Equal length tubes were lead from the airfoil section through a hollow axis to the pressure module. The pressure module used for the wake and the Pitot tube measurements was placed on the floor next to the wake rake. A ZOCEIM16 module was used for the acquisition of the electrical signals.

A total of 134 signals were measured by the data acquisition system during the measurement campaigns:

- 64 airfoil surface static pressures, $p_a(s)$
- 5 wake rake static pressures, $p_w(y)$
- 53 wake rake total pressures, $p_{ow}(y)$
- 3 Pitot tube static pressures, p_{1-3}
- 3 Pitot tube total pressures, p_{o1-3}
- Angle of attack, α
- Air temperature, T
- Atmospheric pressure, p_{atm}
- 2 strain gauges for recording shaft bending corresponding to the lift and drag forces experienced by the airfoil section.
- Electric motor frequency

3.2 Wind tunnel boundary corrections

Wind tunnel corrections should be applied for streamline curvature and down-wash. Horizontal buoyancy, solid and wake blockage could on the other hand be neglected because the test section configuration corresponds to an open jet, which is free to expand, Ray and Pope [4]. The application of wind tunnel boundary corrections for the VELUX wind tunnel was verified in Fuglsang *et al.* [3].

Streamline curvature is introduced to the flow, especially in the case of open test sections. Solid walls do not bound the flow, which is then free to diverge downstream of the airfoil section. The curvature of the flow induces drag and influences the effective angle of attack over the airfoil. In the case of the VELUX tunnel, the presence of the floor close to the jet bottom boundary will influence the streamline curvature and will introduce uncertainty on the wind tunnel corrections. This influence was assumed to be negligible and the applied corrections for streamline curvature do not account for it.

Down-wash is introduced to the flow when the jet dimensions exceed the airfoil section span. The airfoil section corresponds to a finite wing and trailing vortices appear at the ends of the span although reduced by the end plates. The trailing vorticity induces a down-wash velocity in the case of positive lift coefficient. Due to the down wash the angle of attack is reduced and additional drag is induced.

Both down-wash and streamline curvature result in a change in the angle of attack due to the induction of a velocity normal to the flow direction and the airfoil section. It is assumed in this case that down-wash is insignificant compared with streamline curvature because of the presence of end plates.

For the correction of streamline curvature, the method of Brooks and Marcolini [5] was used.

The corrected angle of attack, α, is found from:

$$\alpha = \alpha_t - \frac{\sqrt{3\sigma}}{\pi} C_L - \frac{2\sigma}{\pi} C_L - \frac{\sigma}{\pi} (4C_{Mt}) \ [rad]$$

(3-1)

Where

$$\sigma = \frac{\pi^2}{48} \cdot \left(\frac{c}{h} \right)^2$$

(3-2)

The drag coefficient, C_D, is calculated from:

(3-3)

$$C_D = C_{Dt} + \left[-\frac{\sqrt{3\sigma}}{\pi} C_L \right] C_L$$

The moment coefficient, C_M, is obtained:

$$C_M = C_{Mt} - \frac{\sigma}{2} C_L$$

(3-4)

For details see Fuglsang *et al.* [3].

3.3 Wind tunnel flow conditions

In Fuglsang *et al.* [3] the wind tunnel flow conditions are investigated and it is found that:

- The turbulence intensity at the test section inlet is 1%.
- Between the inlet and the airfoil section, there is a speed-up of, $\varepsilon_{j\text{-}a} = 6.9\%$, and a static pressure drop of $\Delta p_{j\text{-}a} = 15$ Pa/m.

The wind tunnel references for static, p_∞ and total pressures, $p_{o\infty}$ were derived from Pitot 1 measurements, Figure 3-1. The flow acceleration between Pitot 1 and the airfoil section, $\varepsilon_{1\text{-}\infty} = 5.9\%$ and the static pressure drop between Pitot 1 and the airfoil section, $\Delta p_{1\text{-}\infty} = 15$ Pa/m were determined in Fuglsang *et al.* [3] and they are taken into account at the calculation of p_∞ and $p_{o\infty}$.

3.4 Calculation methods

The airfoil pressure coefficient, $C_p(s)$, around the airfoil surface, s, is calculated from:

$$C_p(s) = \frac{p_a(s) - p_\infty}{q_\infty}$$

(3-5)

Where

$$q_\infty = p_{o\infty} - p_\infty$$

(3-6)

The normal force coefficient, C_N, and the tangential force coefficient, C_T, are found from integration of the $C_P(s)$ distribution along the *x*- and *y*-axis as seen

in Figure 3-4. The airfoil lift coefficient, C_L, and drag coefficient, C_D, are found by resolving C_N and C_T perpendicular to and parallel with the oncoming flow:

$$C_L = \cos(\alpha)C_N + \sin(\alpha)C_T$$

(3-7)

$$C_D = -\cos(\alpha)C_T + \sin(\alpha)C_N$$

The moment coefficient, C_M, is found from integration of $C_P(s)$ at $x/c = 0.25$.
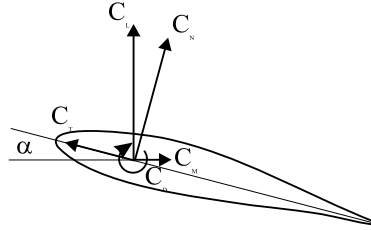

Figure 3-4 Sign convention for aerodynamic coefficients.

The total airfoil drag is the sum of skin friction and pressure drag. By assuming a control surface, which surrounds the airfoil section, the total drag can be calculated from the balance of the momentum flux entering and exiting the control surface. The momentum profile entering is assumed uniform and is calculated from the wind tunnel free stream reference pressures. The momentum profile exiting is calculated from the pressures measured by the wake rake.

Assuming that the flow is 2D, the total wake drag coefficient, C_{Dw}, is calculated from Rae and Pope [4]:

$$C_{Dw} = \frac{2}{c} \int_{y_{min}}^{y_{max}} \sqrt{\frac{p_o(y) - p(y)}{q_\infty}} \cdot \left(1 - \sqrt{\frac{p_o(y) - p(y)}{q_\infty}}\right) dy \qquad (3\text{-}8)$$

In the analysis of dynamic loads, while the airfoil is in pitching motion, the pitching motion is described by the equation:

$$\alpha = A\sin(\omega t) + \alpha_m$$

(3-9)

The pitching motion is related to the reduced frequency:

$$k = \frac{\omega c}{2V_\infty} \qquad (3\text{-}10)$$

4 Airfoil sections and aerodynamic devices

The tested airfoils were the NACA 63-415 airfoil, Abbott and Doenhoff [1], and the NACA 63-415-Risø-D airfoil, Fuglsang and Bak [2].

4.1 Airfoil sections

For both airfoil sections, the span was 1.9 m. The chord was 0.600 m for the NACA 63-415 airfoil and 0.606 m for the NACA 63-415-Risø-D airfoil. In Figure 4-1 the airfoils are shown, with the co-ordinates normalised with the NACA 63-415 airfoil chord length.
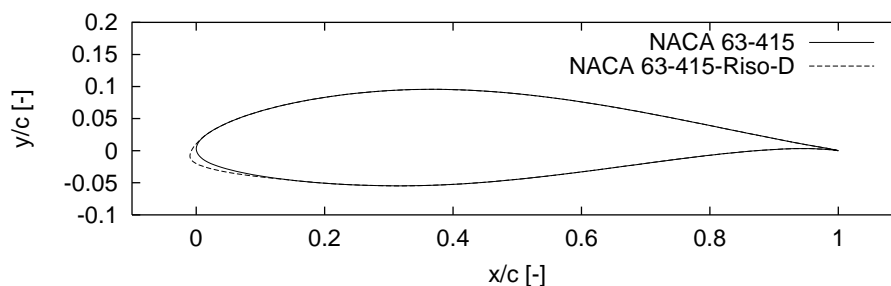

Figure 4-1 Theoretical co-ordinates for the NACA 63-415 and the NACA 63-415-Risø-D airfoil sections.

LM Glasfiber A/S, Denmark, manufactured both airfoils. Risø carried out the instrumentation of pressure tabs, end pieces and strain gauges. Each model was manufactured in two pieces as an upper and a lower shell to facilitate instrumentation. The models were made of fibre glass in moulds. The pressure taps were Ø0.5 mm holes drilled directly in the model surface with the exception of the leading and trailing edges where tubes were installed through the model surface, flush with the surface. Inside the model metal tubes were mounted parallel to the drilled holes and flexible plastic tubes were connected to the metal tubes. When the instrumentation was completed the two shells were assembled. The pressure tubes were taken outside of the model through a hollow axis at one side of the airfoil.

The airfoil sections were equipped with 62 pressure taps in the centre line region. The taps were placed along the chord at the centre line of the model in a staggered alignment to minimise disturbances from upstream taps. Additional taps were drilled close to the centre line as a back up to taps at important positions, e.g., the leading and trailing edges, and in order to allow measurements away from the centre line.

The position of the pressure taps on the model was decided by looking on the theoretical pressure distributions derived from numerical calculations. The distribution of the pressure taps reflected the expected pressure gradients and the tap spacing was dense at the leading edge. There was more taps on the upper surface compared to the lower surface. After the model was permanently

assembled the model dimensions and the tap positions were checked for compliance with the theoretical ones.

Only minor differences were found between the theoretical and the measured co-ordinates as shown in Figure 4-2 and Figure 4-3. For all airfoil models, it was concluded that this would not result in significant errors in the pressure distribution and in the derivation of aerodynamic loads.
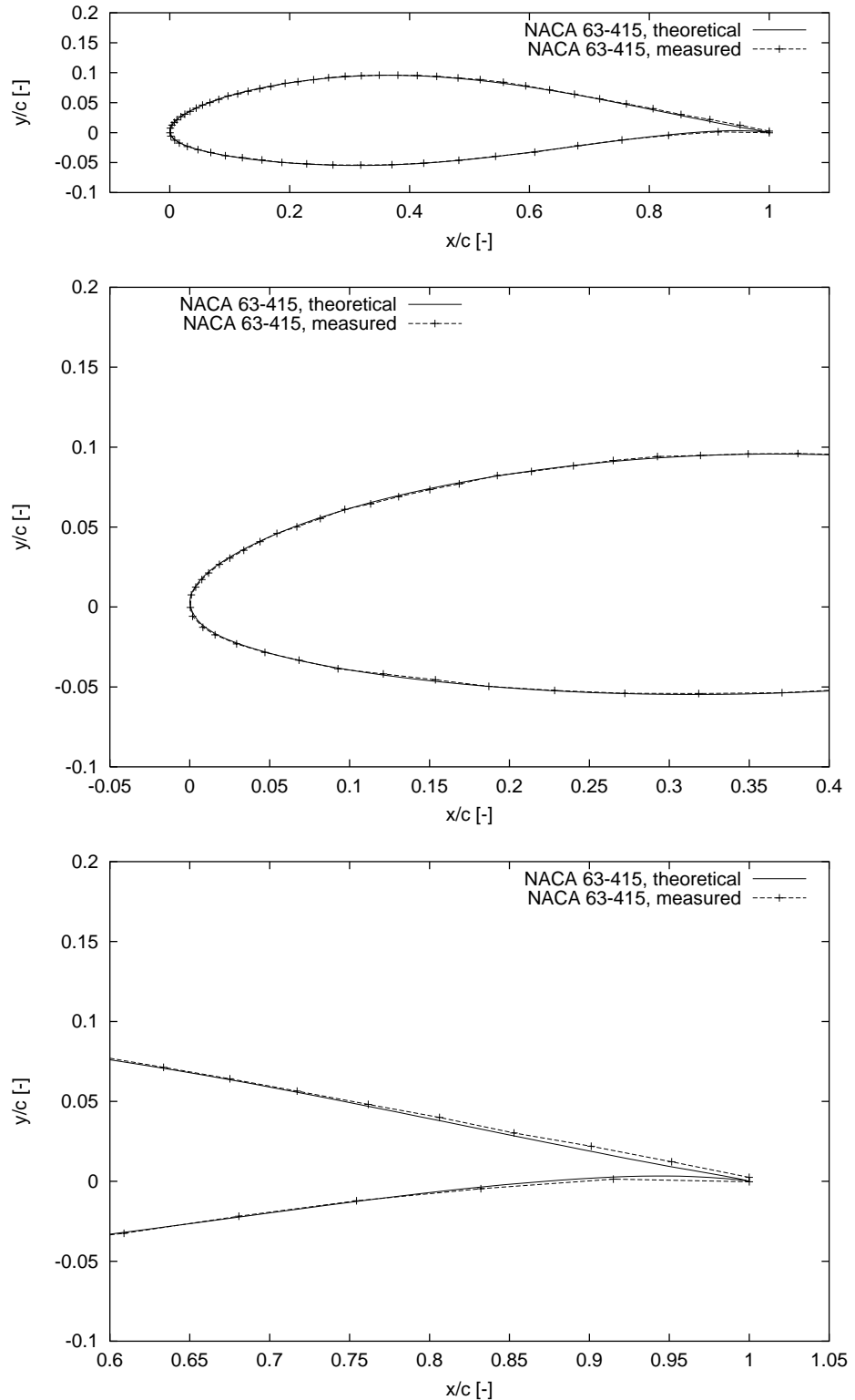

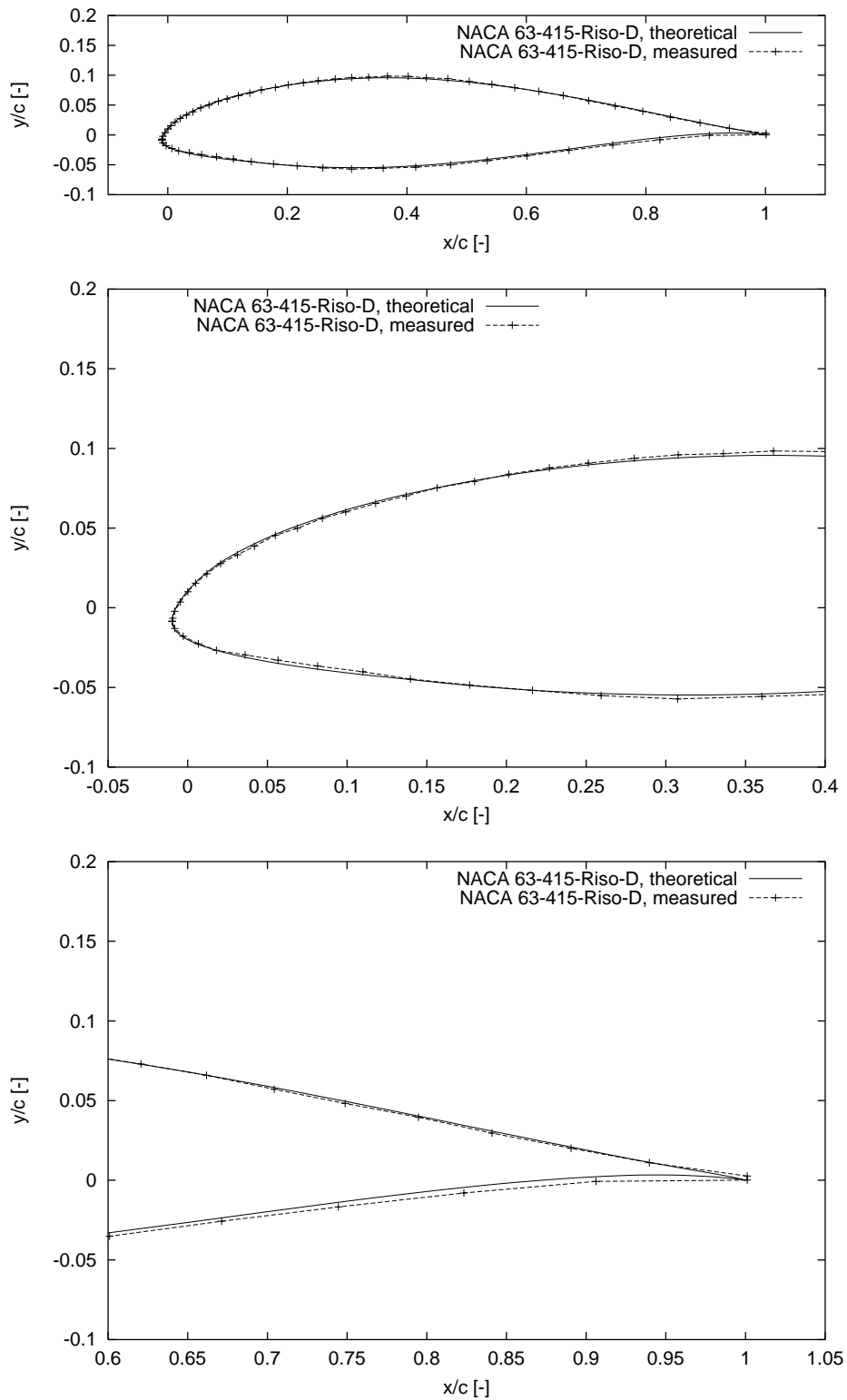*Figure 4-2 Theoretical and measured co-ordinates for the NACA 63-415 airfoil section.*

Figure 4-3 Theoretical and measured co-ordinates for the NACA 63-415-Risø-D airfoil section

4.2 Leading edge roughness

Trip tape was mounted on the airfoil model surface to simulate the effects from leading edge roughness (LER). LER appears when dirt, bugs or soil accumulate on the wind turbine blades in dirty environments.

Three different kinds of LER were used:
- 90° zigzag tape of height 0.35 mm
- 60° zigzag tape of height 0.85 mm
- Car customising tape of height 0.12 mm

4.2.1   90° zigzag tape

The used trip tape was originally intended for use on gliders and was manufactured as fibre enforced plastic tape that was glued to the airfoil model surface.

Figure 4-4 shows the 90° zigzag trip tape with a 90° angle, a width of 3 mm and a thickness of 0.35 mm.
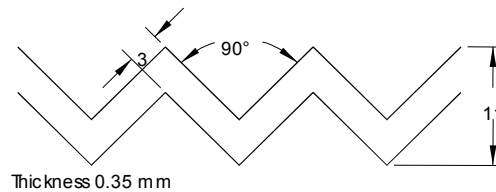

Thickness 0.35 mm

Figure 4-4 Trip tape with 90° zigzag of 3 mm width and 0.35 mm thickness.

The trip tape was mounted at different positions:
- At x/c=0.05 on the suction side and x/c=0.10 on the pressure side
- From x/c=0, i.e. the leading edge, towards the pressure side
- From x/c=0, i.e. the leading edge, towards the suction side

4.2.2   60° zigzag tape

As for the 90° zigzag tape the trip tape was originally intended for use on gliders and was as well manufactured as fibre enforced plastic tape that was glued to the airfoil model surface.

Figure 4-5 shows the 60° zigzag trip tape with a 60° angle, a width of 3 mm and a thickness of 0.85 mm.
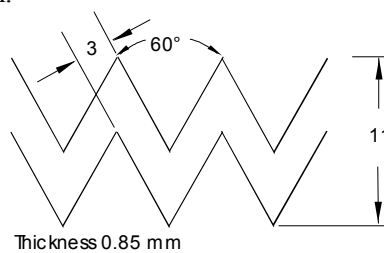

Thickness 0.85 mm

Figure 4-5 Trip tape with 60° zigzag of 3 mm width and 0.85 mm thickness.

The trip tape was mounted from x/c=0, i.e. the leading edge, towards the pressure side.

4.2.3   Car customising tape

This trip tape was originally intended for use on cars for decoration and was manufactured as plastic tape that was glued to the airfoil model surface.

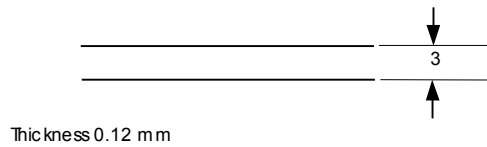Figure 4-6 shows the trip tape with a width of 3 mm and a thickness of 0.12 mm.

Thickness 0.12 mm

Figure 4-6 Trip tape of 3 mm width and 0.12 mm thickness.

The trip tape was mounted from x/c=0, i.e. the leading edge, towards the pressure side.

4.3 Stall strips

Stall strips (SS) were mounted to the airfoil model surface at the leading edge to modify the stall characteristics. SS are used to control both power and loads for wind turbines. SS of length 0.5 m and up to several meters in radial direction are occasionally mounted at the outer part of a wind turbine blade.

Two different kinds of SS were used:
- '7 mm' SS
- '5 mm' SS

4.3.1 '7 mm' stall strip

'7 mm' SS are used on full scale wind turbines. The SS are slightly curved on one side to fit the curvature of the leading edge, Figure 4-7. They are positioned on the blade where the chord length is around 0.8 m.
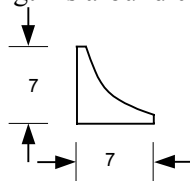

Figure 4-7 Profile view of a '7 mm' stall strip of 7 mm side length used for application on the leading edge.

The '7 mm' SS were mounted at two stagnation point positions on both airfoils, Table 4-1 and Figure 4-9 and Figure 4-10. The stagnation points were computed using the CFD code *EllipSys2D* where smooth airfoils were assumed. Thus, '7 mm' SS were used because of the curvature of the leading edge.

Table 4-1 Position of '7 mm' SS on the two airfoils

Stagnation point at AOA [°]	NACA 63-415 Chordwise position [%]	NACA 63-415-Risø-D Chordwise position [%]
-2	0.23	-
0	0.00	0.00
2	0.23	0.03

4.3.2 '5 mm' stall strip

'5 mm' SS are triangular devices, Figure 4-8, slightly smaller than '7 mm' SS. It was made to scale from the 0.8 m chord length on full scale wind turbines to the 0.6 m chord length on the model airfoil, corresponding to SS of 5 mm.
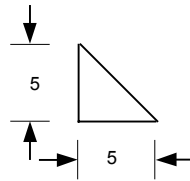
Figure 4-8 profile view of '5 mm' stall strip of 5 mm side length.

The '5 mm' SS were mounted at three stagnation point positions on both airfoils, Table 4-2 and Figure 4-9 and Figure 4-10. The stagnation points were computed using the CFD code *EllipSys2D* where smooth airfoils were assumed.

Table 4-2 Position of '5 mm' SS on the two airfoils.

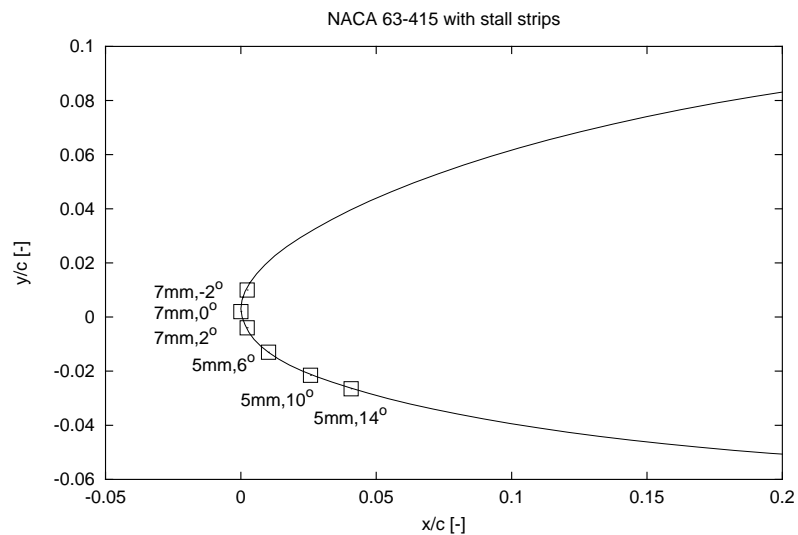| Stagnation point at AOA [°]	NACA 63-415 Chordwise position [%]	NACA 63-415-Risø-D Chordwise position [%]
6	1.02	0.79
10	2.57	2.25
14	4.07	4.48

Figure 4-9 Position of '7 mm' and '5 mm' SS on the NACA 63-415 airfoil.
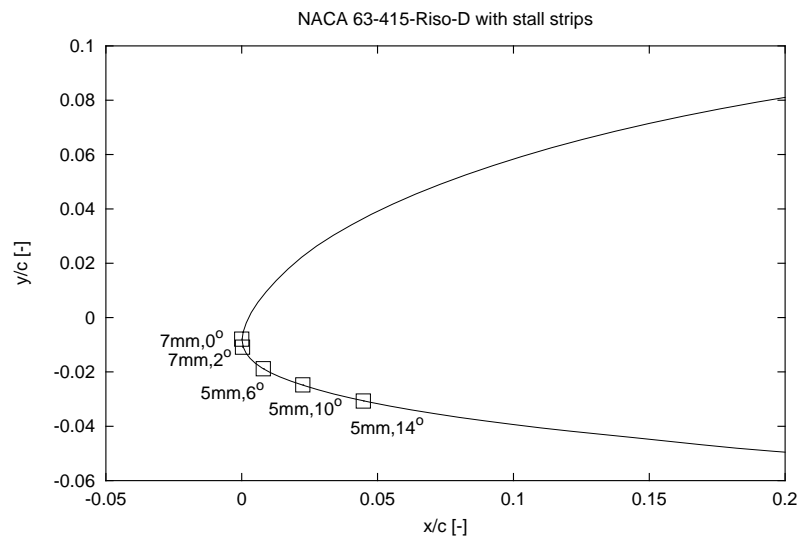

Figure 4-10 Position of '7 mm' and '5 mm' SS on the NACA 63-415-Risø-D airfoil.

Risø-R-1193(EN)

4.4 Vortex generators

Vortex generators (VG's) are often used at the inner part of wind turbine blades located on the blade suction side between 10 % and 30 % of the chord counted from the leading edge. They increase the maximum lift coefficient by delaying separation on the airfoil suction side to higher incidences. At the same time, they increase the drag coefficient.

The design of the VG's followed the guide lines from Hoerner and Borst [6] and was similar to those used for numerous airfoil tests by Timmer [7], at Delft University, The Netherlands.

Figure 4-11 shows the shapes and dimensions of the used VG's. They have a height of 6 mm a length of 18 mm. The angles relative to the chordwise direction are ±19.5°. The leading edge spacing between two VG's is 10 mm and the distance between two consecutive pairs is 25 mm. They are of the Delta wing type with a shape of orthogonal triangles and they are placed with their right-angle perpendicular to the airfoil surface and their height increases towards the trailing edge. The presence of the VG's results in the formation of counter-rotating vortices, which transfer high momentum fluid down to the airfoil surface and thus delay separation. To achieve this VG's are arranged in pairs at equal and opposite angles relative to the chord of the blade.

The VG's were constructed from 0.2 mm thick stainless steel. Each VG was cut out and bent perpendicular to the surface. The VG's were glued on the airfoil model surface separately. The thickness of the gluing surface will slightly disturb the measurements since the flow has to enforce the edge of the gluing surface. In particular the drag coefficient at low angles of attack will be increased.
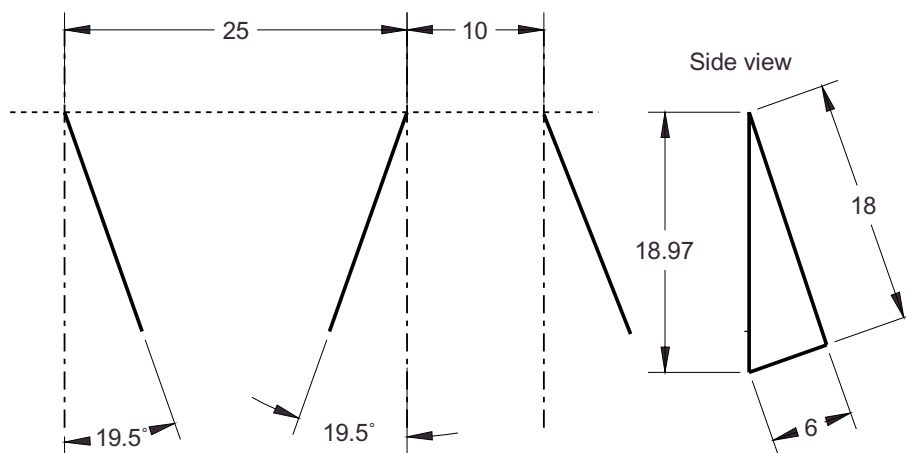

Figure 4-11 Vortex generators of height 6 mm, length 18 mm.

In the performed measurements the VG's were mounted either at 20 % of the chord length at the suction side.

5 Results

All shown results were corrected for wind tunnel effects and the aerodynamic forces were referenced to the wind tunnel free stream flow by use of Pitot 1 taking into account corrections for speed-up and pressure loss, Fuglsang *et al.* [3].

The measurements for each airfoil are reported correspondingly in Chapter 5 and 6 with a comparison in Chapter 7. The measurements are discussed in Chapter 8.

The different types of conducted measurements are described in Appendix A.

5.1 Testing conditions

The testing conditions are shown in Table 5-1.

Table 5-1 Testing conditions

Airfoil chords	NACA 63-415	$c = 0.606$ m
	NACA 63-415-Risø-D	$c = 0.600$ m
Flow velocity	$v = 40$ m/s	
Reynolds number	$Re = 1.6 \times 10^6$	
Dynamic inflow		
Angular velocity	$\omega = 12.9$ *rad/s*	
Reduced frequency	$k = 0.092$	
Amplitude	$1.4^o < A < 2.0^o$	

5.2 Numerical calculations

The smooth measurements were compared with numerical calculations. The Ellipsys2D Navier-Stokes code, Sørensen [8], with the k-ω SST turbulence model, Menter [9], was used for turbulent flow calculations. Free transition was modelled using the Michel transition criteria, Michel [10].

The Ellipsys2D Navier-Stokes code was used with both turbulent flow on the entire airfoil and free transition. The difference between the two kinds of computations is related to the way that transition from laminar to turbulent flow takes place.

5.3 Presentation of results

Chapter 6 presents the results from the NACA 63-415 airfoil, Chapter 7 the results from the NACA 63-415-Risø-D airfoil, and finally Chapter 8 presents comparisons between the results from the two airfoils. Results are presented as pressure distributions, C_P and as lift, C_L, drag, C_D, and moment coefficients, C_M, respectively. For the comparisons in Chapter 8 also the tangential force

coefficient, C_T, defined as $C_T=C_L sin(\alpha)-C_D cos(\alpha)$, is shown. This coefficient represents the force, which pulls the airfoil forward in chordwise direction. In figures and tables the acronyms shown in Table 5-3 and Table 5-4 are used.

Chapter 6 and 7 contains measurements for each airfoil as shown in Table 5-2.

Table 5-2 Measurements for each airfoil.

Smooth flow	Measurements with no devices and a clean airfoil surface.
LER Zigzag-tape 90°	Measurements with 90° zigzag-tape at different positions at the leading edge.
LER on pressure side	Measurements with three different kinds of trip tape mounted one at a time from the leading edge towards the pressure side.
Stall strips	Measurements with stall strips at different positions at the leading edge.
Vortex generators	Measurements with vortex generators at 20 % chord length at the suction side. Measurements were carried out only for the NACA 63-415 airfoil.
Dynamic stall	Measurements with an oscillating airfoil with no devices and with stall strips at the CFD computed stagnation point at α=10°.
Stall characteristics	Measurements with fixed α in stall to investigate the stability of the flow and possibly reveal any tendencies to double stall as described by Bak *et al.* [11]. The measurements are time series lasting from one to three minutes. The stall behaviour is presented as standard deviations for α, C_L and C_D. Furthermore, the probability density function of α, C_L and C_D are shown to reveal the distribution of the measured quantities. If a well defined maximum in the number of samples is not present then time series for this measurement will be shown.

Table 5-3 Description of acronyms to describe the devices and their positions on the airfoil.

SS	Stall Strips
LER	Leading edge roughness
ZZ 60°	60° Zigzag tape
ZZ 90°	90° Zigzag tape
TT	Trip tape
s.s.	From the very leading edge towards the suction side
p.s.	From the very leading edge towards the pressure side
0.05/0.10	LER placed on x/c=5% on suction side and 10% on pressure side

Table 5-4 Description of acronyms to describe the positions of the stall strips on the airfoil.

P0,-2	Position of stagnation point at $\alpha = -2^\circ$
P0,0	Position of stagnation point at $\alpha = 0^\circ$
P0,2	Position of stagnation point at $\alpha = 2^\circ$
P0,6	Position of stagnation point at $\alpha = 6^\circ$
P0,10	Position of stagnation point at $\alpha = 10^\circ$
P0.14	Position of stagnation point at $\alpha = 14^\circ$

6 Results for NACA 63-415

6.1 NACA 63-415, smooth flow (run024)
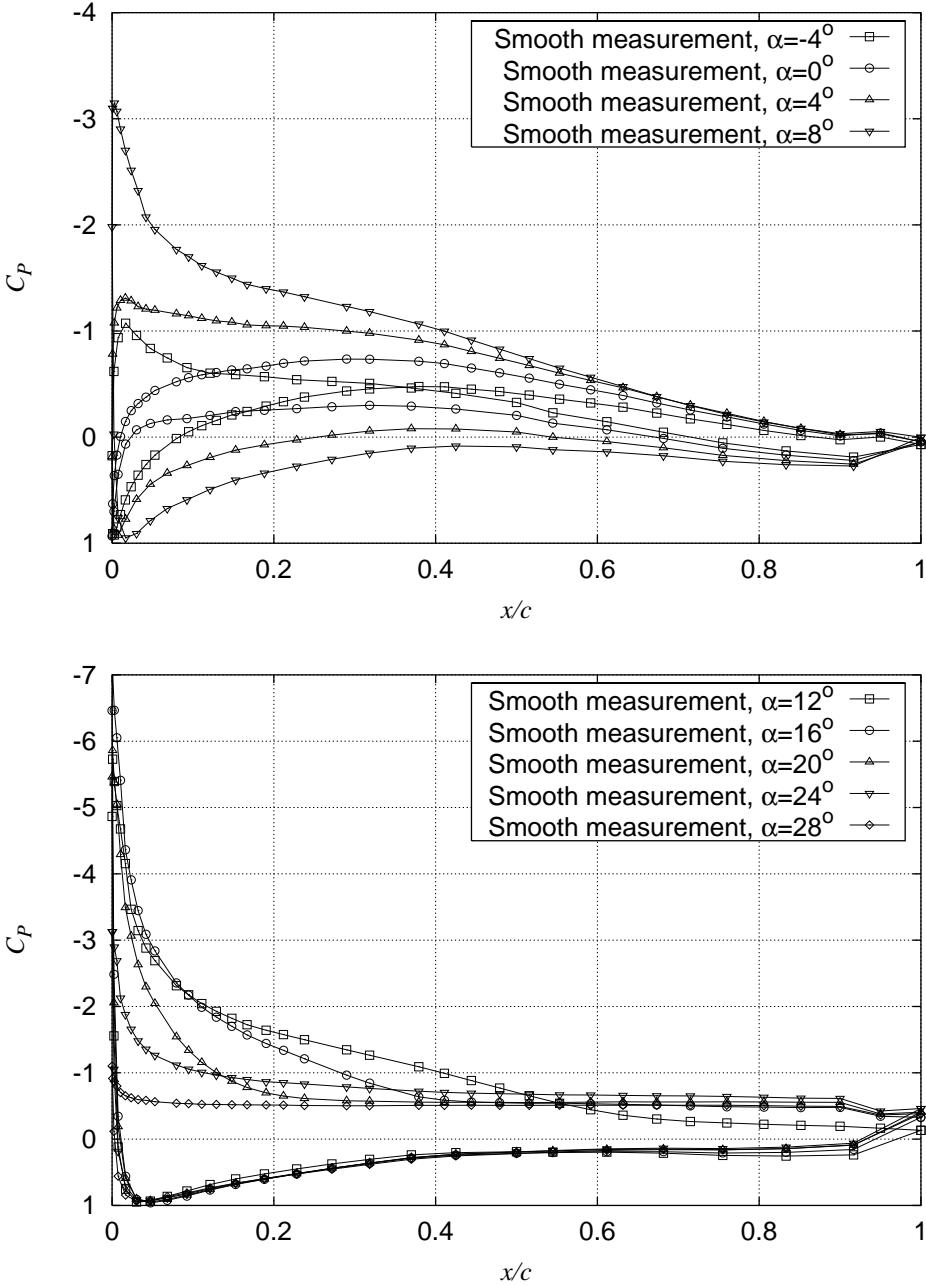
Figure 6-1 C_P at different angles of attack for NACA 63-415 smooth measurements (run024).
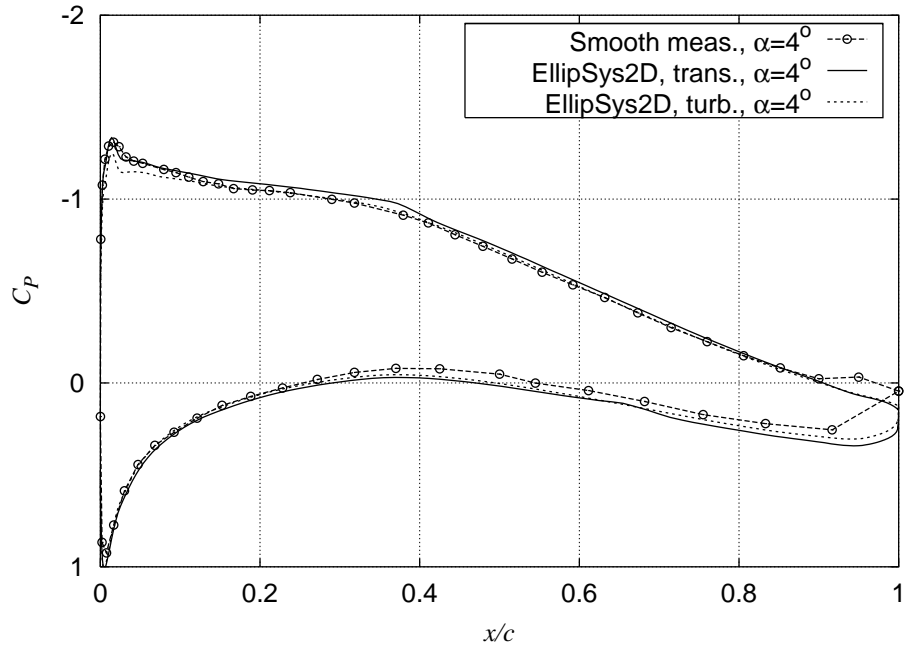
Figure 6-2 C_P at $\alpha = 4°$ for NACA 63-415 smooth measurements compared with EllipSys2D calculations with transition model and turbulent flow, respectively (run024).
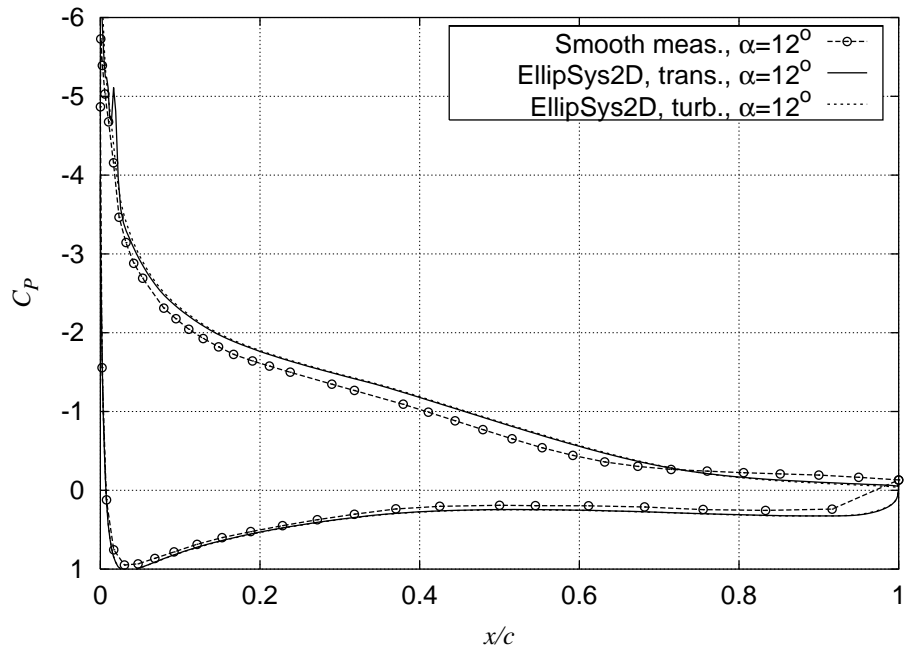
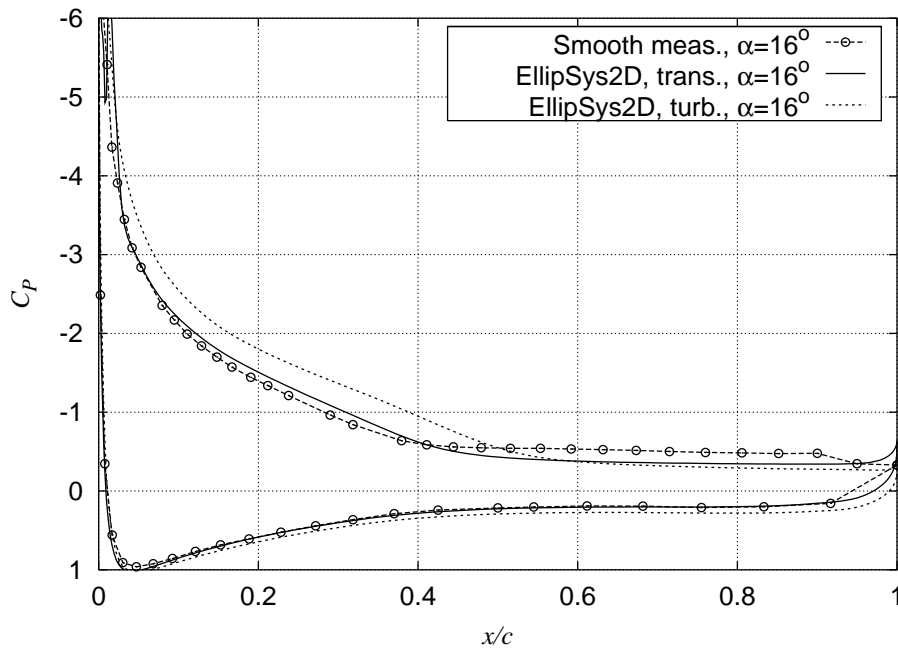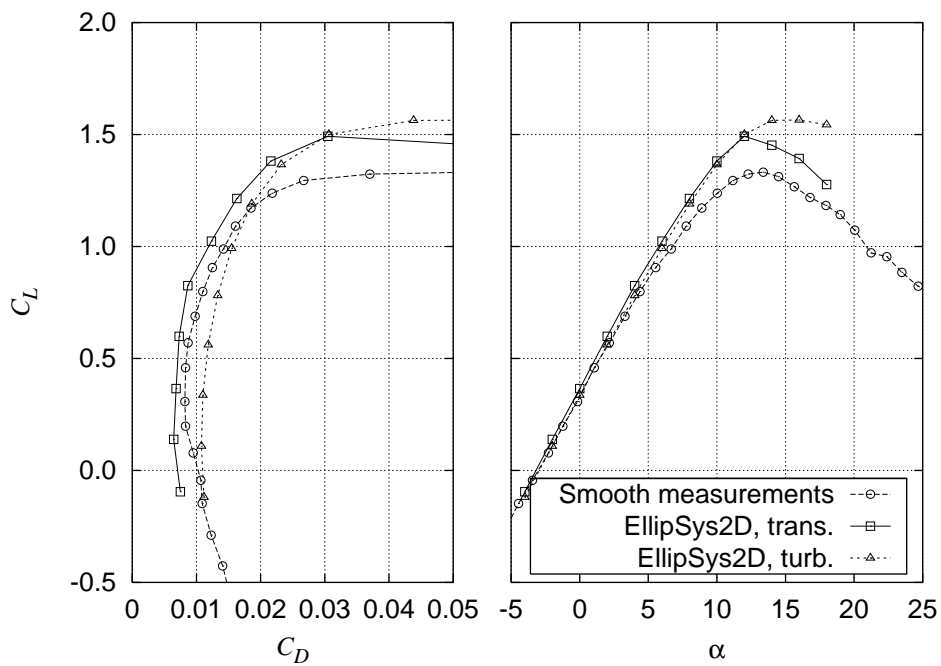*Figure 6-3 C_P at $\alpha = 12°$ for NACA 63-415 smooth measurements compared with EllipSys2D calculations with transition model and turbulent flow, respectively (run024).*

Figure 6-4 C_P at $\alpha = 16°$ for NACA 63-415 smooth measurements compared with EllipSys2D calculations with transition model and turbulent flow, respectively (run024).

Figure 6-5 C_L-C_D for NACA 63-415 smooth measurements compared with EllipSys2D calculations with transition model and turbulent flow, respectively (run024).
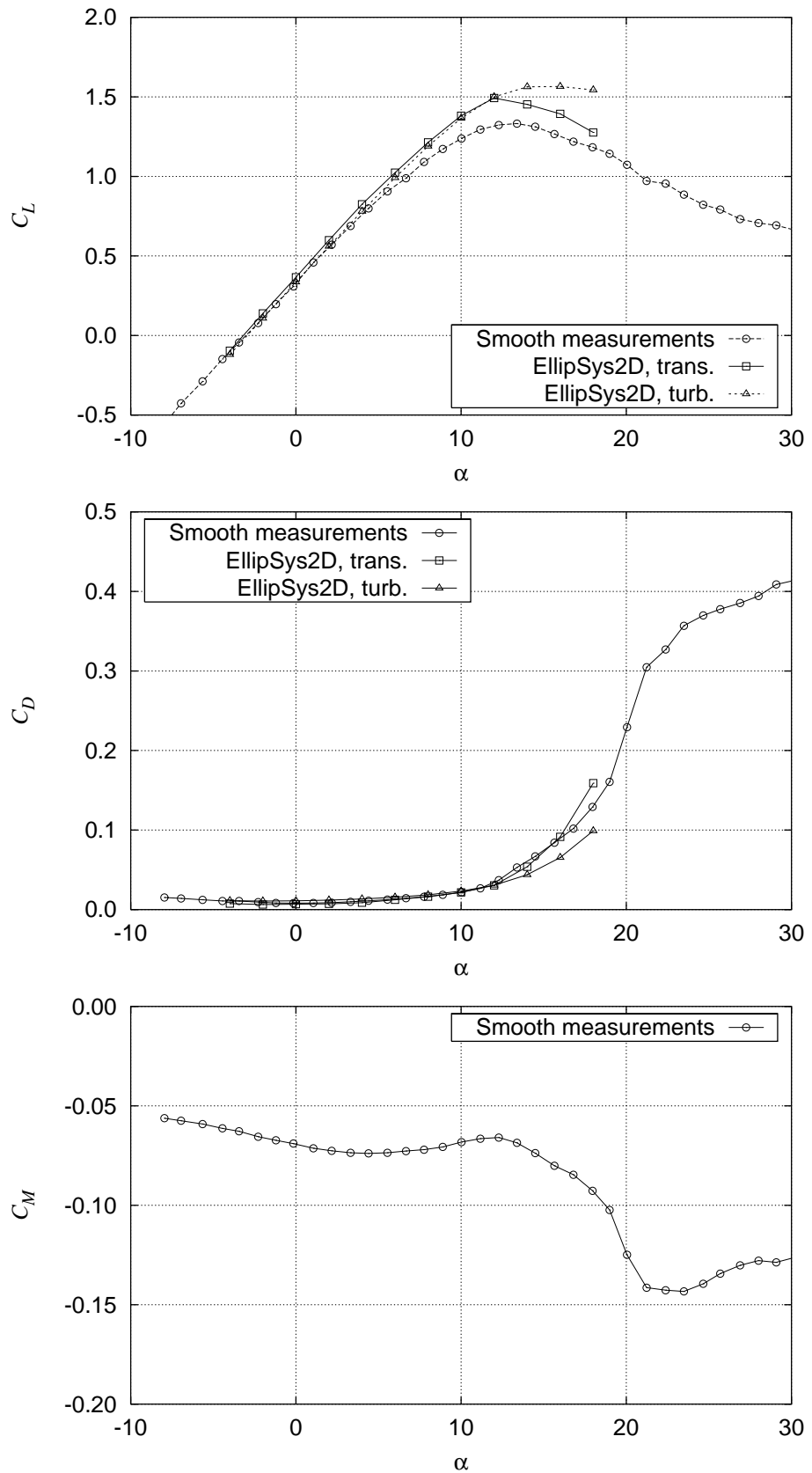
Figure 6-6 C_L, C_D and C_M for NACA 63-415 smooth measurements compared with EllipSys2D calculations with transition model and turbulent flow, respectively (run024).

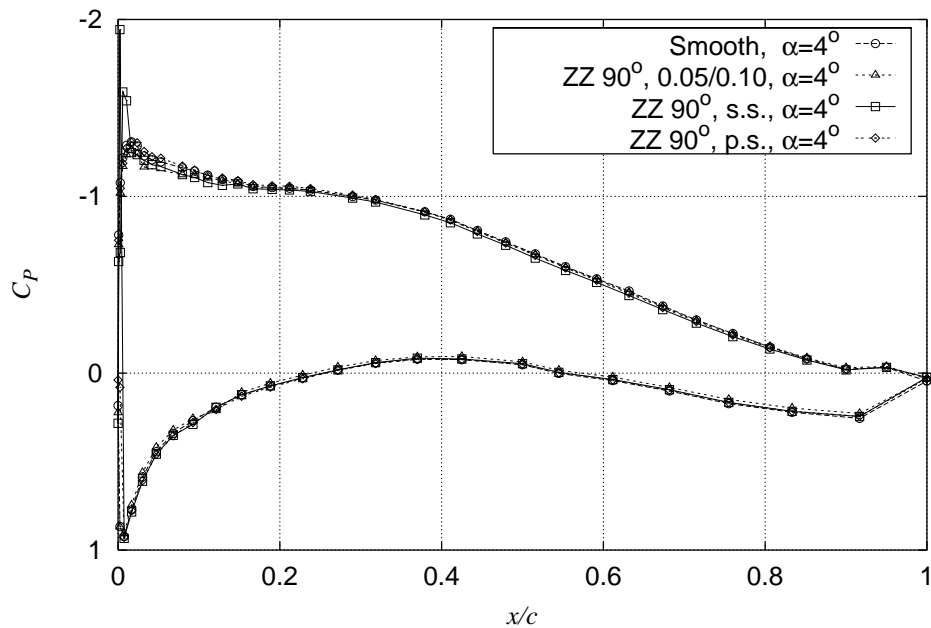## 6.2 NACA 63-415, LER zigzag tape 90° (run025, 027, 028)

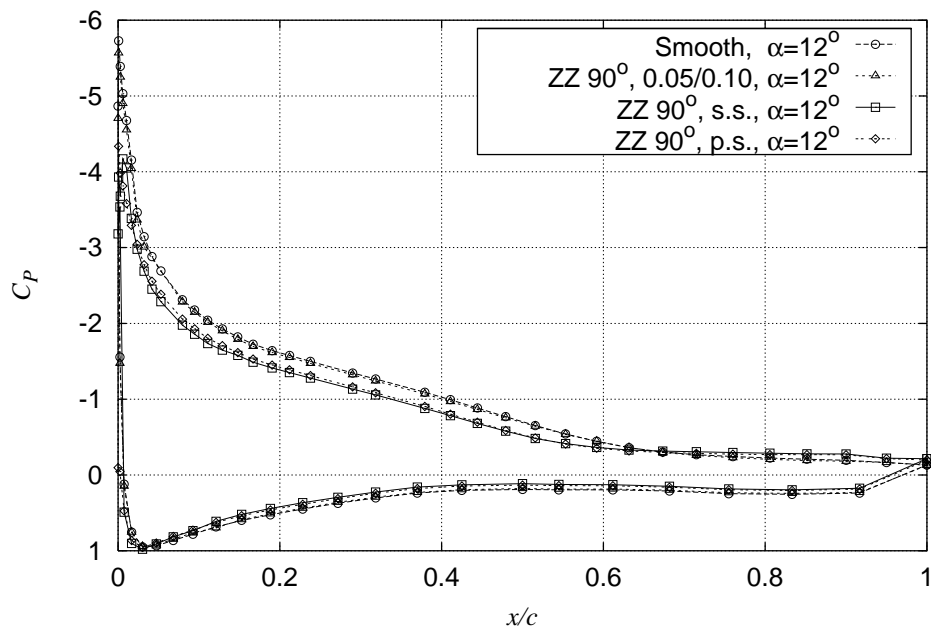*Figure 6-7 C_P at α = 4° for NACA 63-415, ZZ90° LER measurements compared with smooth flow.*

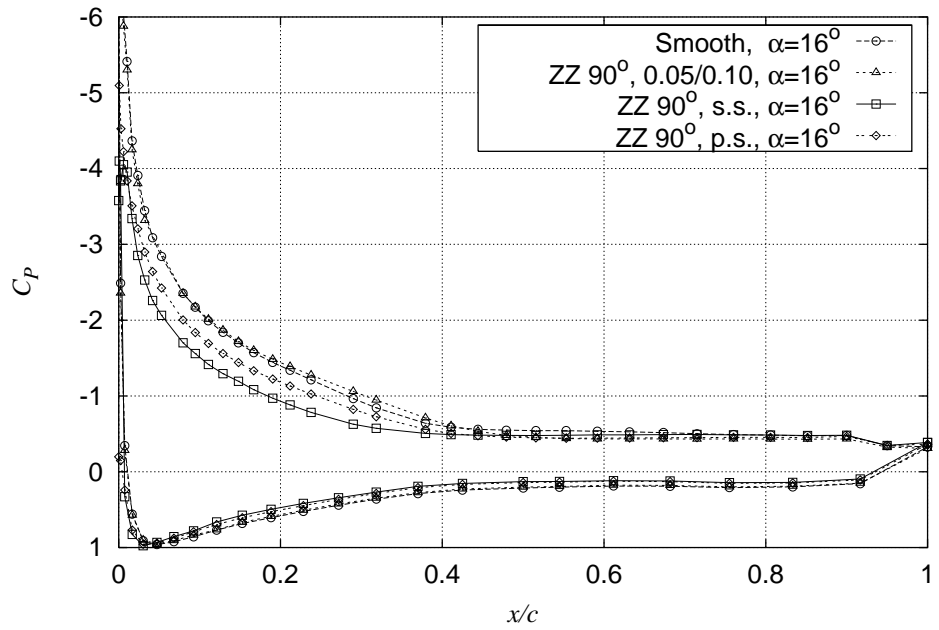*Figure 6-8 C_P at α = 12° for NACA 63-415, ZZ90° LER measurements compared with smooth flow.*

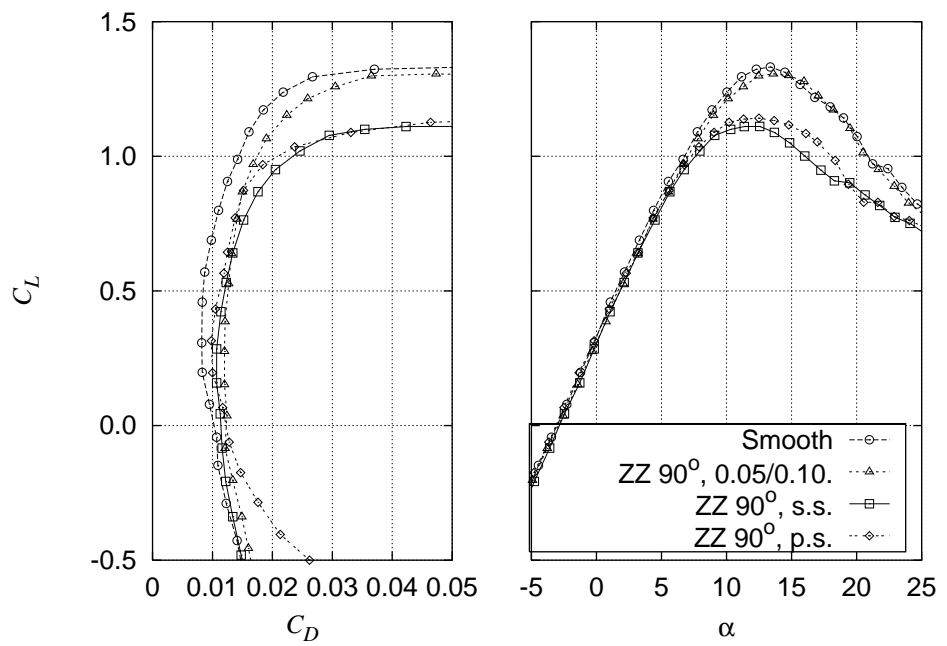*Figure 6-9 C_P at α = 16° for NACA 63-415, ZZ90° LER measurements compared with smooth flow.*

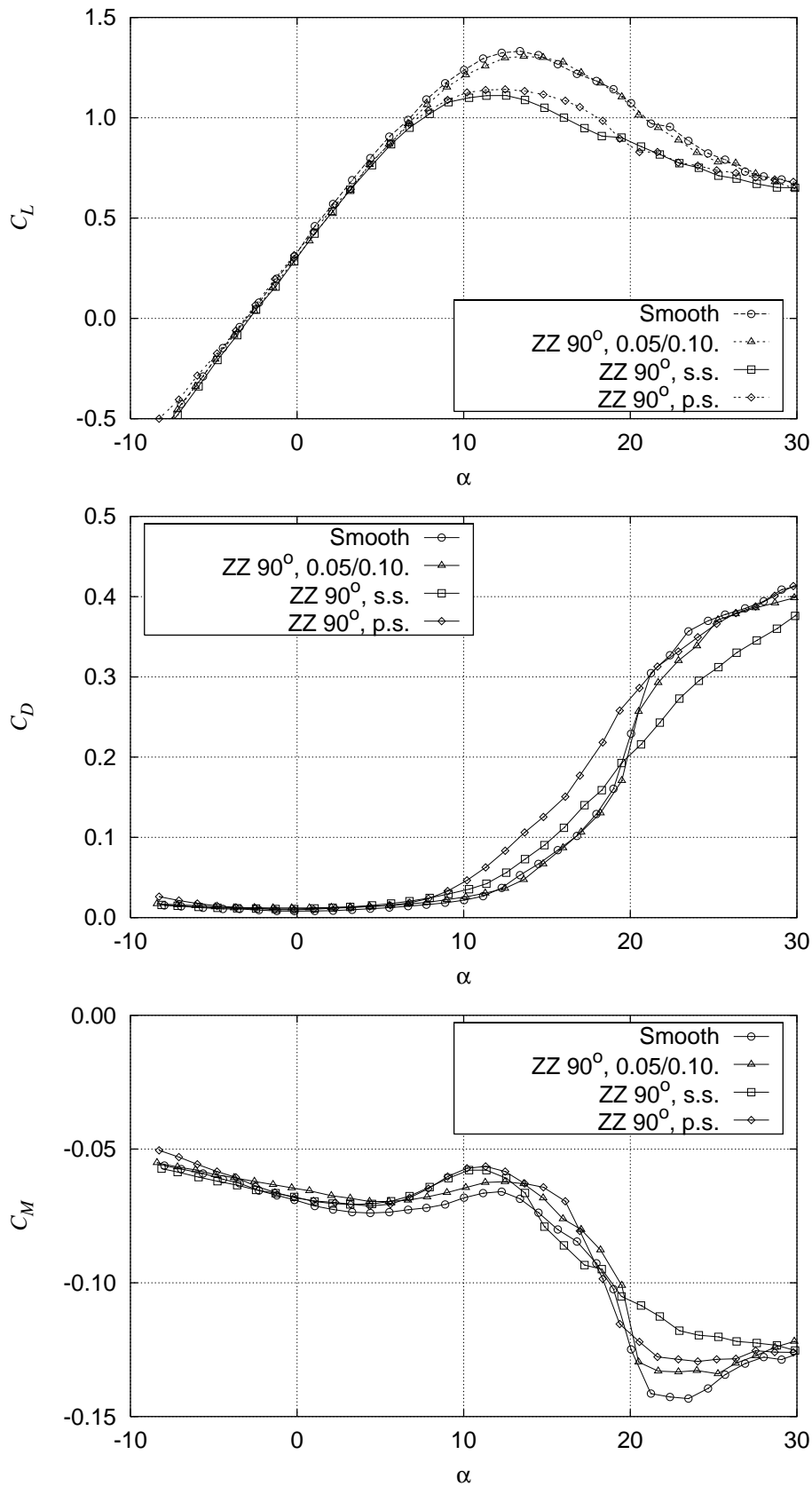*Figure 6-10 C_L-C_D for NACA 63-415, ZZ90° LER measurements compared with smooth flow.*

Figure 6-11 C_L, C_D and C_M for NACA 63-415, ZZ90° LER measurements compared with smooth flow.

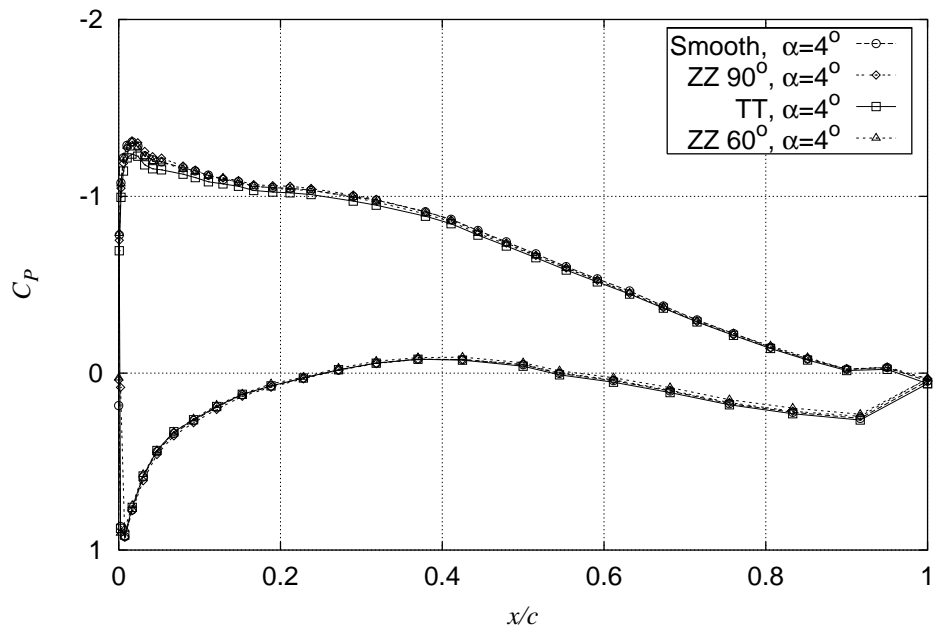## 6.3 NACA 63-415, LER on pressure side (run028, 092, 094)

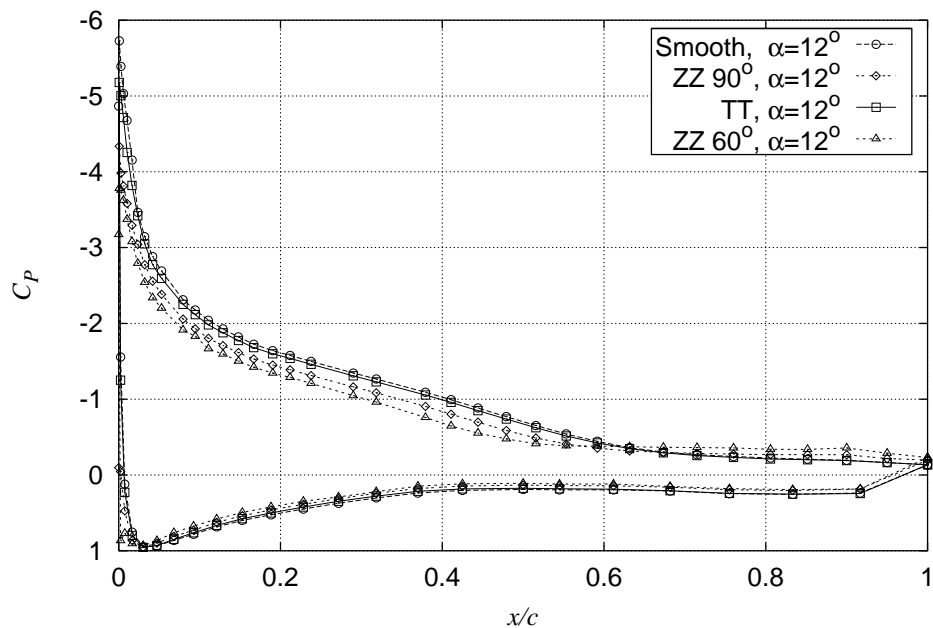*Figure 6-12 C_P at α = 4° for NACA 63-415, LER on pressure side measurements compared with smooth flow.*

Figure 6-13 C_P at α = 12° for NACA 63-415, LER on pressure side measurements compared with smooth flow.
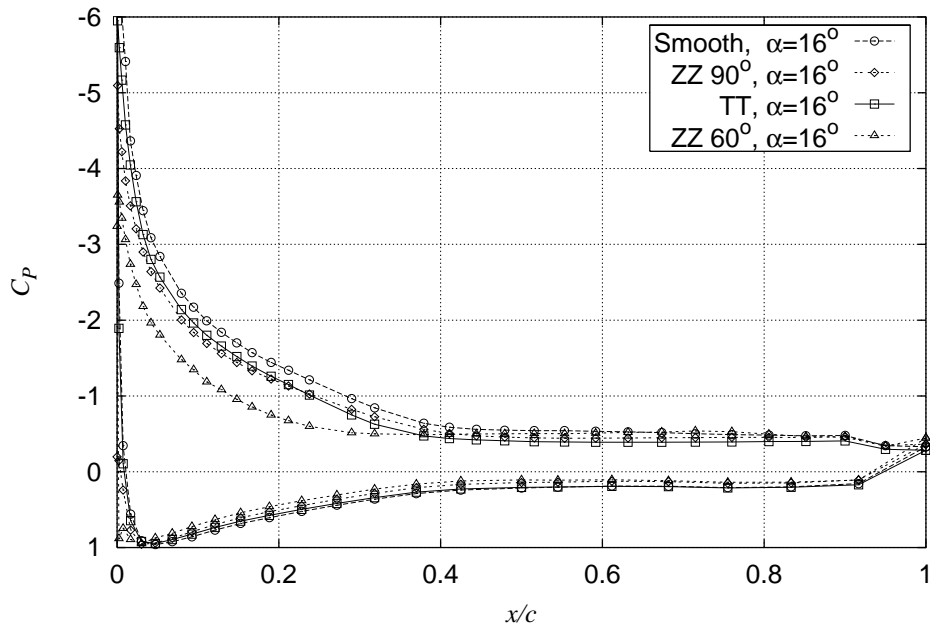
Risø-R-1193(EN)

Figure 6-14 C_P at α = 16° for NACA 63-415, LER on pressure side measurements compared with smooth flow.
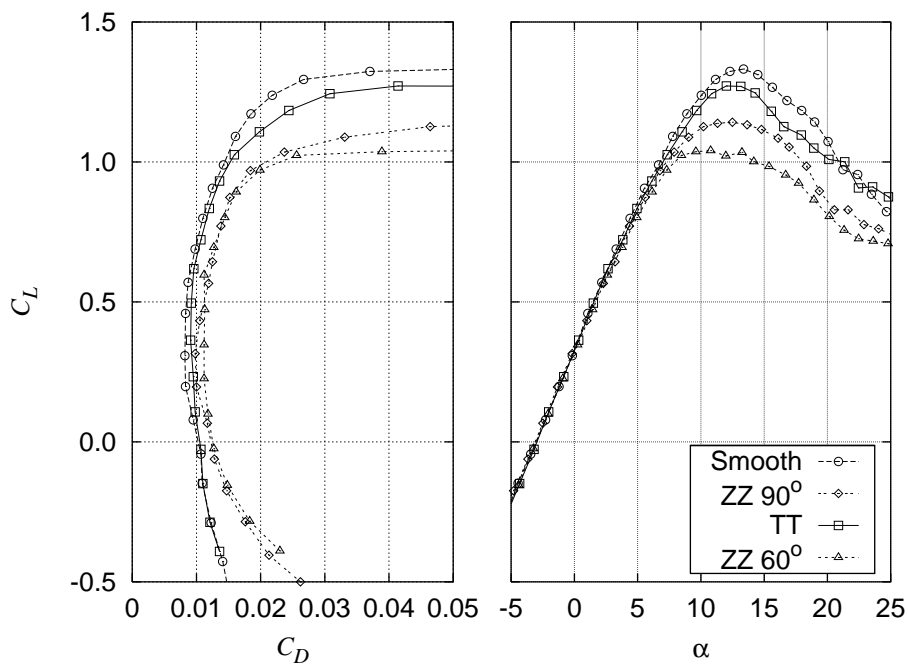

Figure 6-15 C_L-C_D for NACA 63-415, LER on pressure side measurements compared with smooth flow.

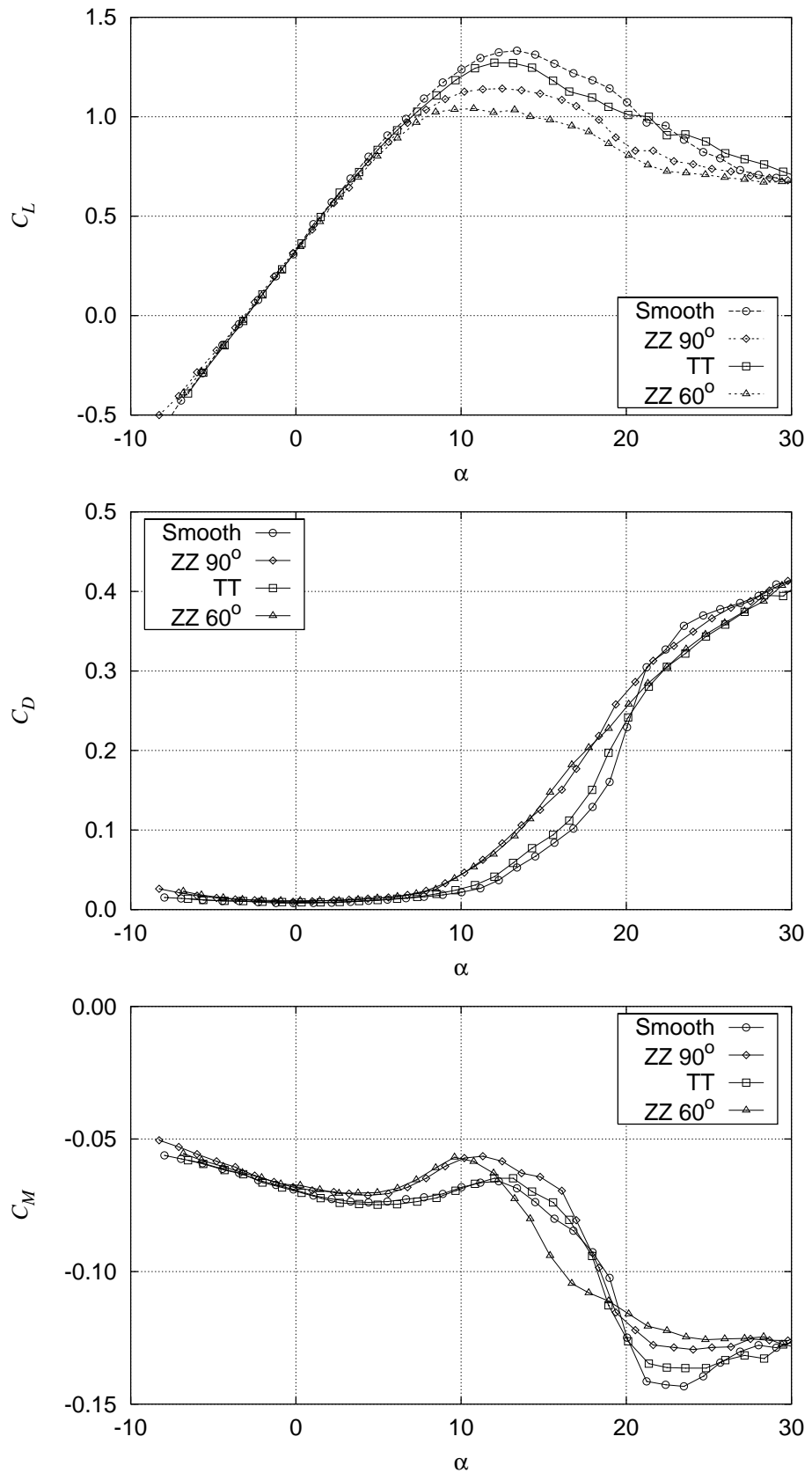*Figure 6-16 C_L, C_D and C_M for NACA 63-415, LER on pressure side measurements compared with smooth flow.*

6.4 NACA 63-415, VG on suction side, x/c = 0.20 (run072)

Figure 6-17 C_P at $\alpha = 4°$ for NACA 63-415, VG on suction side, x/c = 0.20, measurements compared with smooth flow
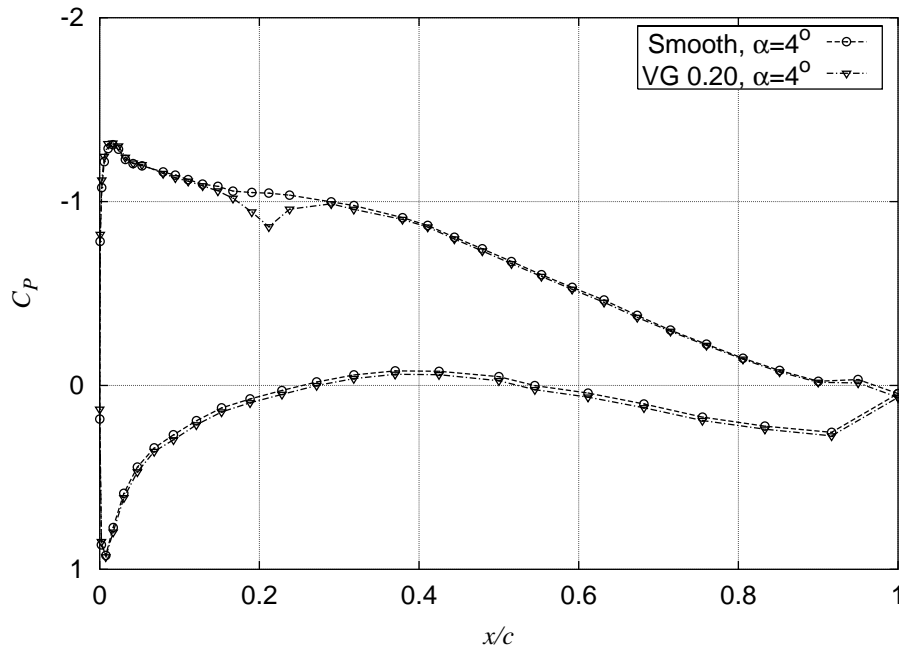

Figure 6-18 C_P at $\alpha = 12°$ for NACA 63-415, VG on suction side, x/c = 0.20, measurements compared with smooth flow

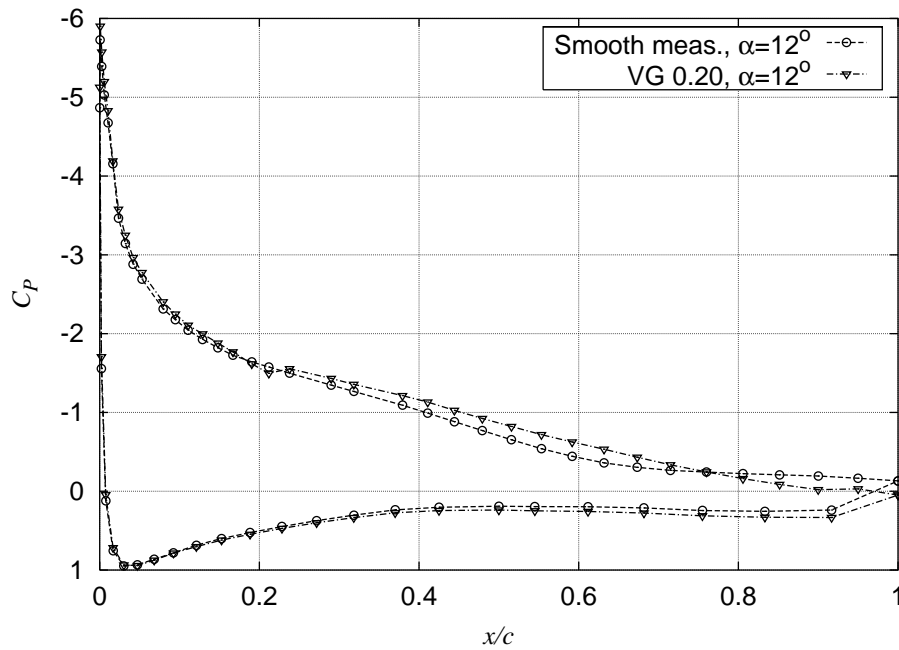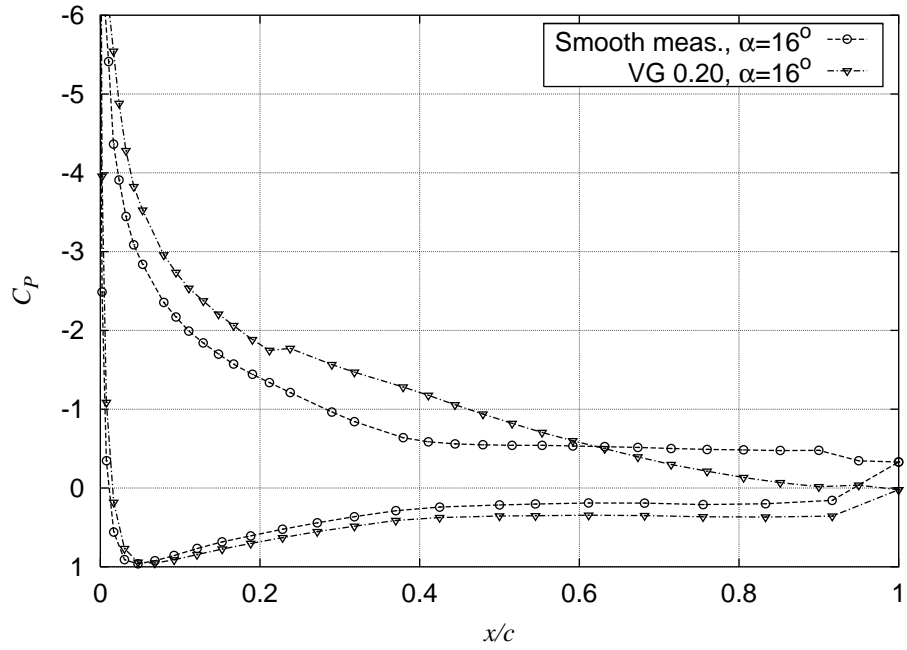*Figure 6-19 C_P at $\alpha = 16°$ for NACA 63-415, VG on suction side, x/c = 0.20, measurements compared with smooth flow*
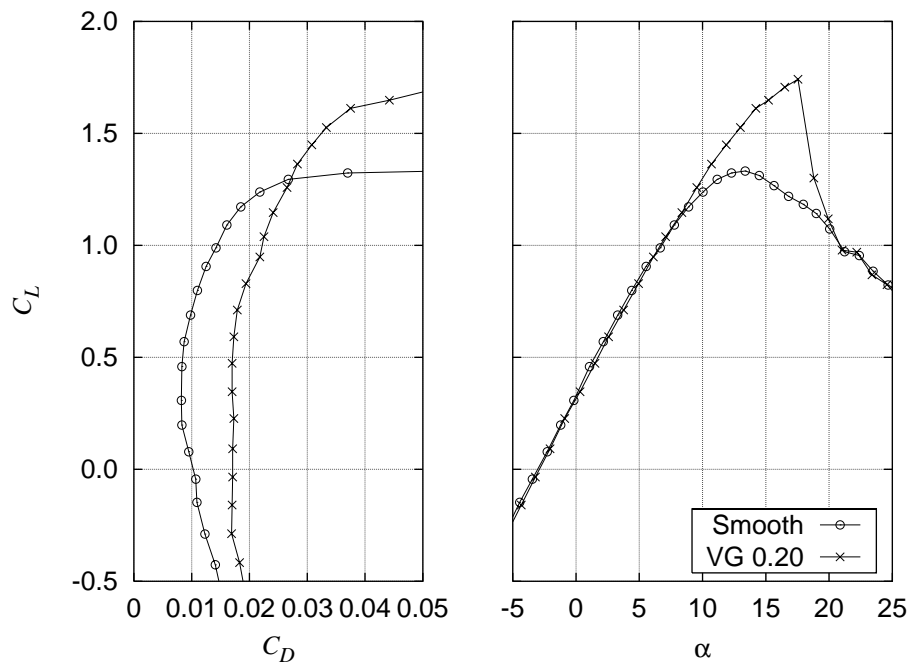
Figure 6-20 C_L-C_D for NACA 63-415, VG on suction side, x/c = 0.20, measurements compared with smooth flow
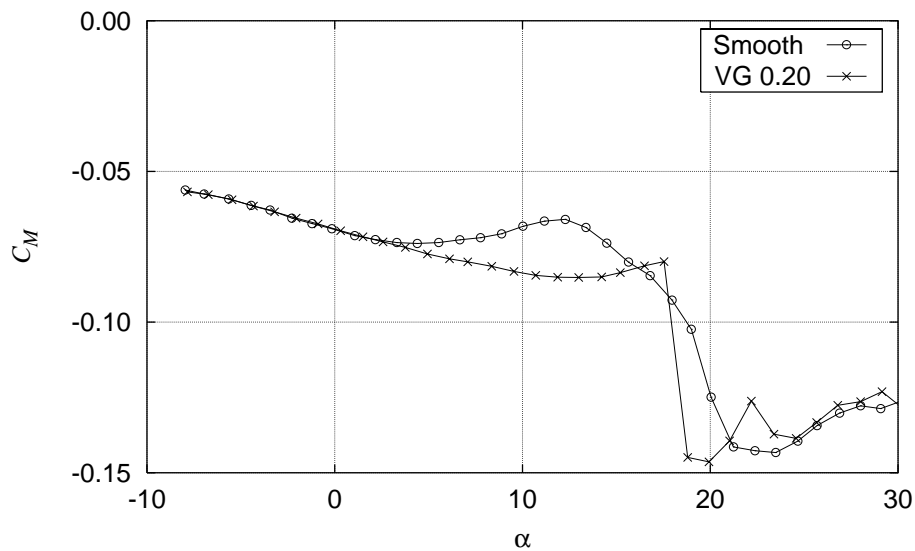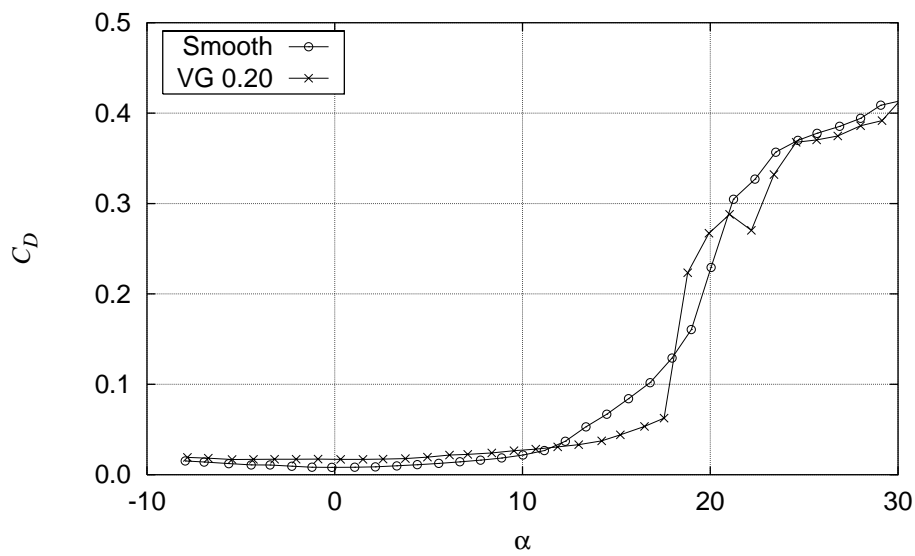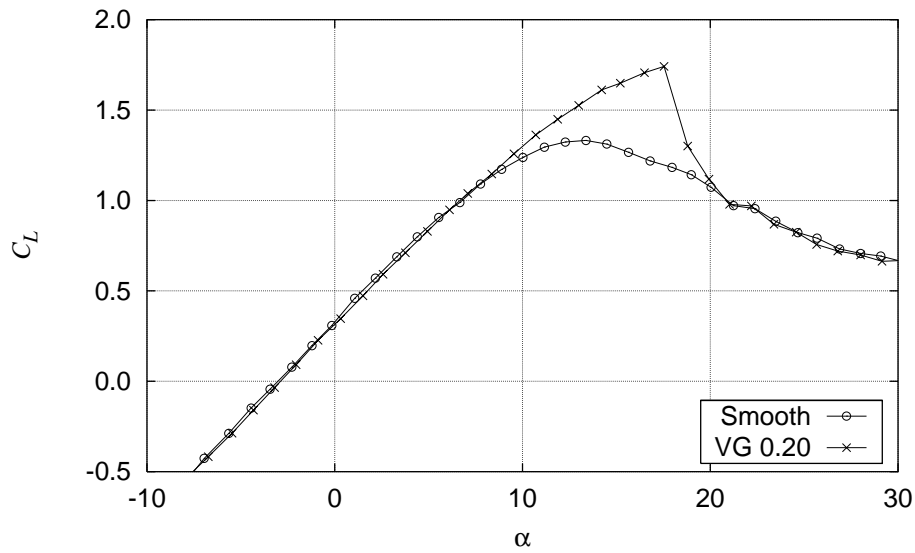
Figure 6-21 C_L, C_D and C_M for NACA 63-415, VG on suction side, x/c = 0.20, measurements compared with smooth flow

6.5 NACA 63-415, 7 mm stall strips (run093, 085, 086)
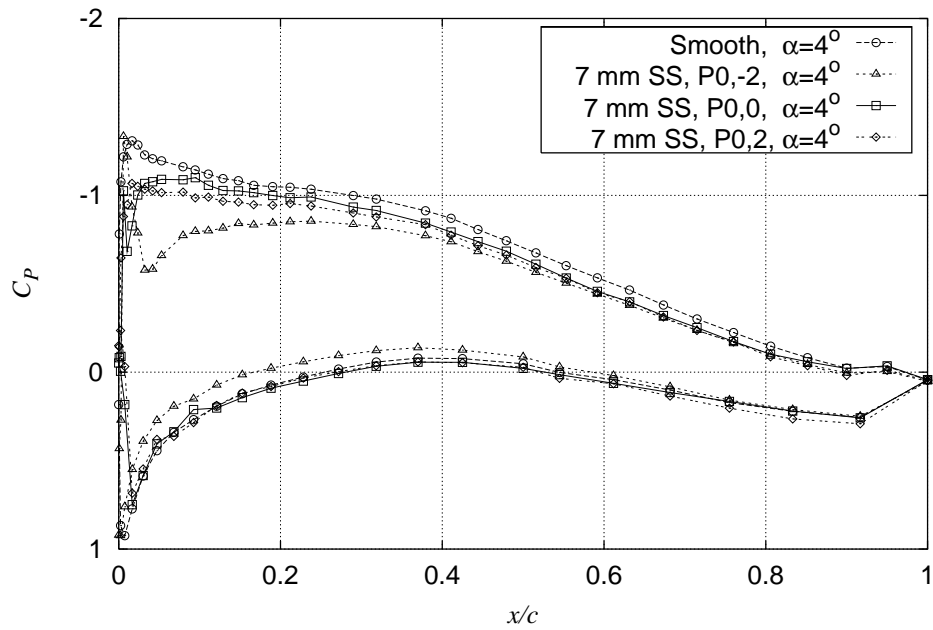
Figure 6-22 C_P at $\alpha = 4°$ for NACA 63-415, 7mm Stall strips measurements compared with smooth flow.
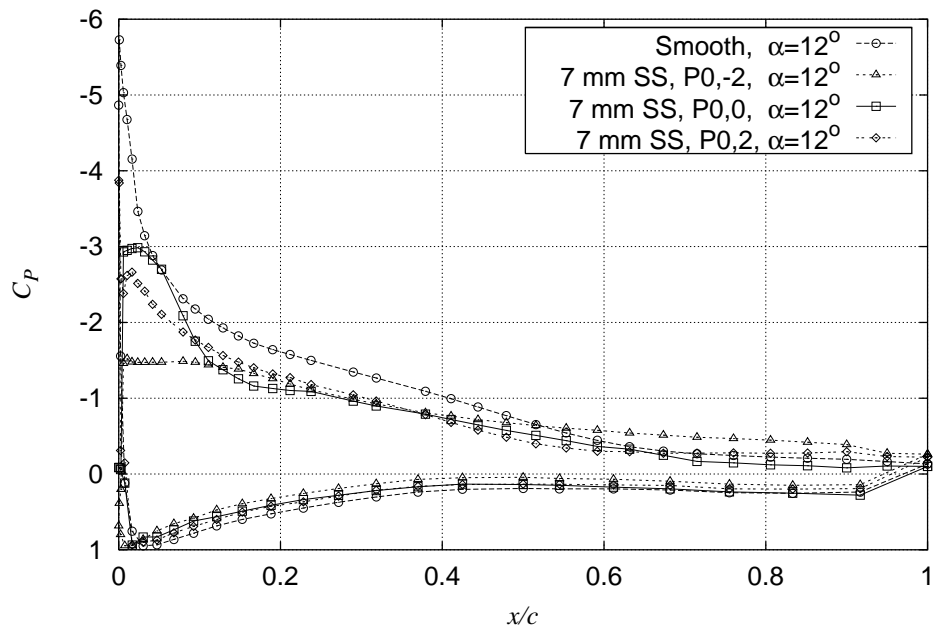
Figure 6-23 C_P at $\alpha = 12°$ for NACA 63-415, 7mm Stall strips measurements compared with smooth flow.
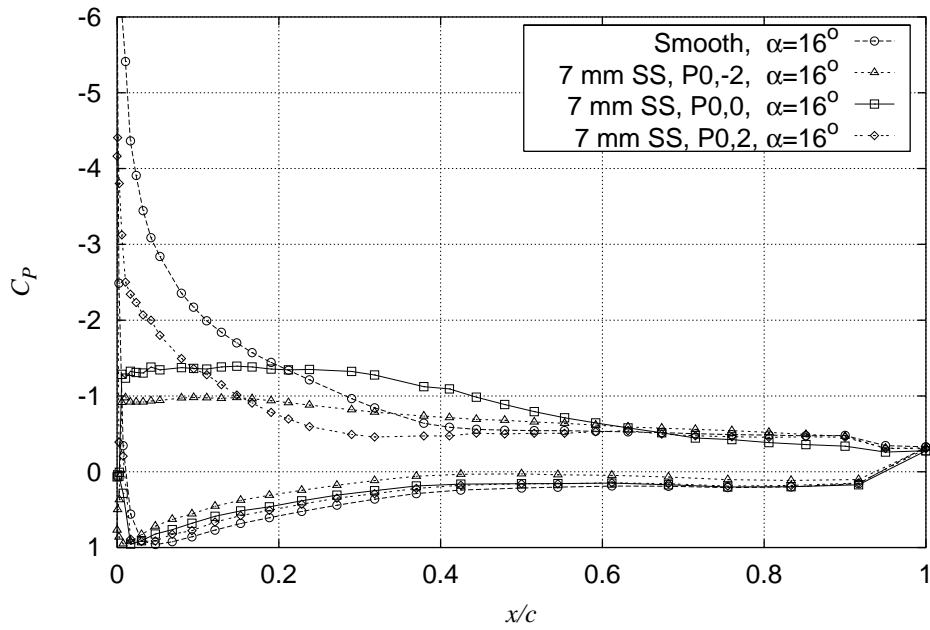
Figure 6-24 C_P at $\alpha = 16°$ for NACA 63-415, 7mm Stall strips measurements compared with smooth flow.
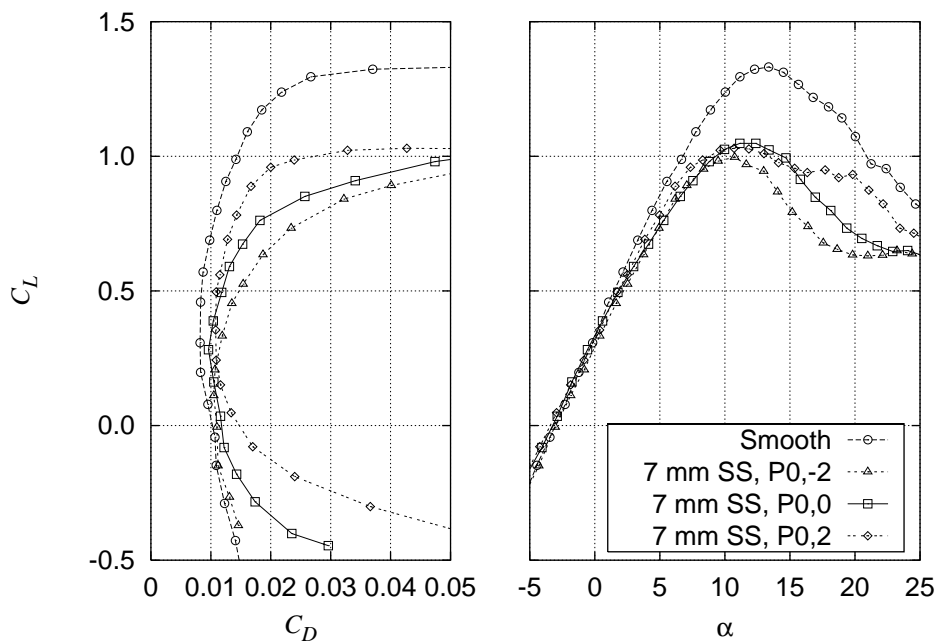
Figure 6-25 C_L-C_D for NACA 63-415, 7mm Stall strips measurements compared with smooth flow.
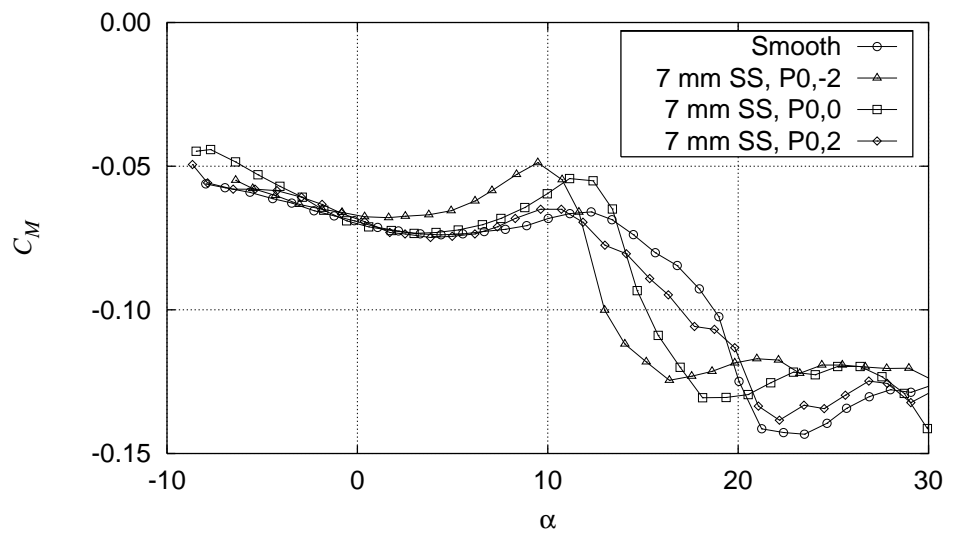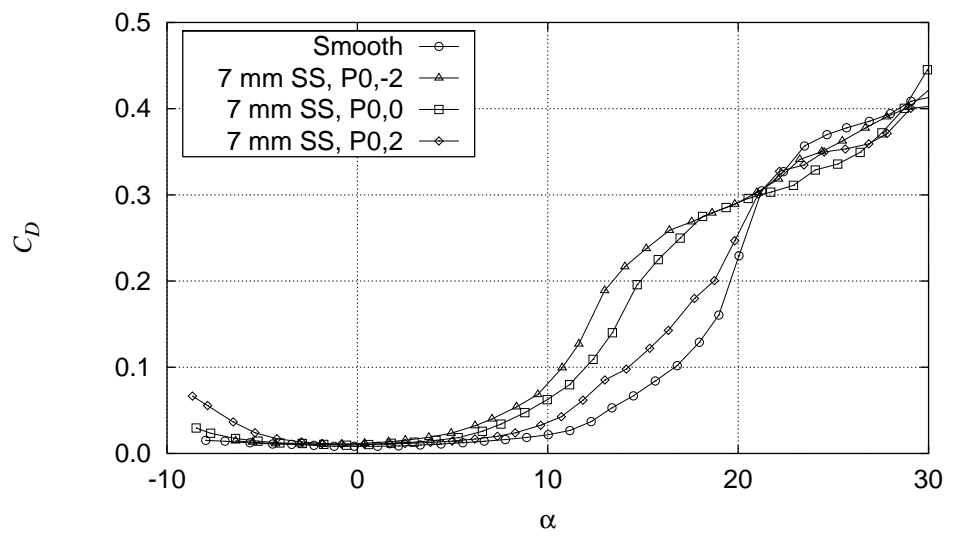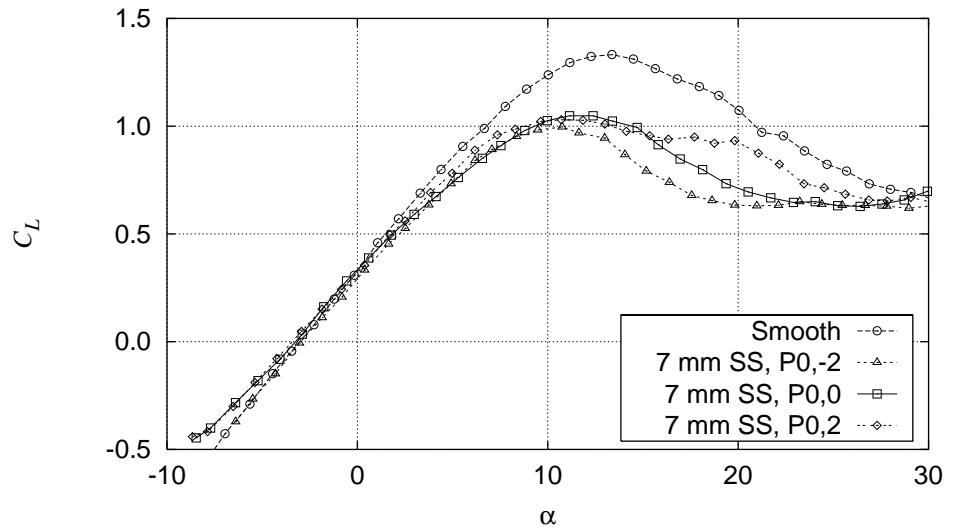
Figure 6-26 C_L, C_D and C_M for NACA 63-415, 7mm Stall strips measurement compared with smooth flow.

6.6 NACA 63-415, 5 mm stall strips (run087, 089, 088)
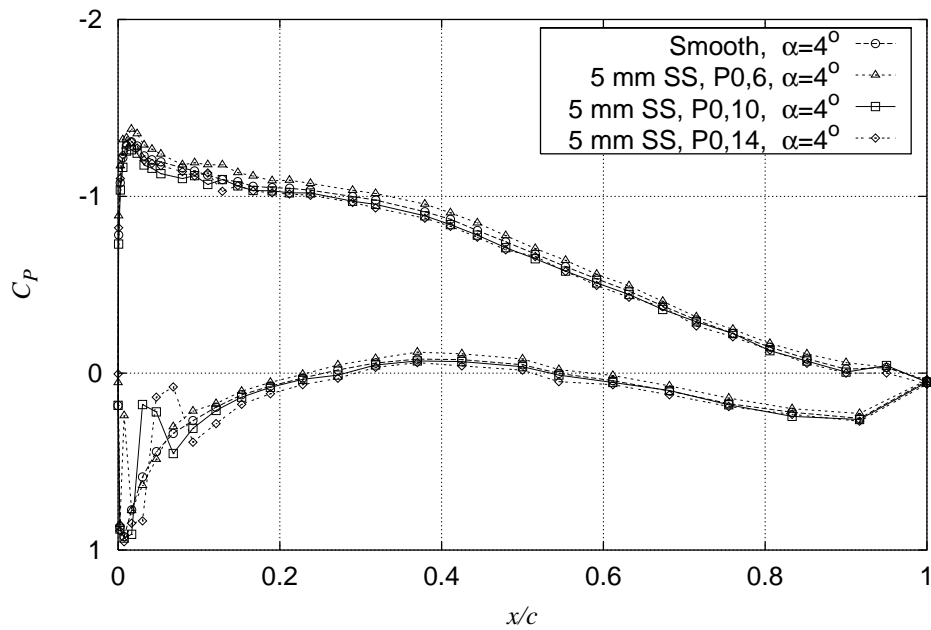
Figure 6-27 C_P at α = 4° for NACA 63-415, 5mm Stall strips measurements compared with smooth flow.
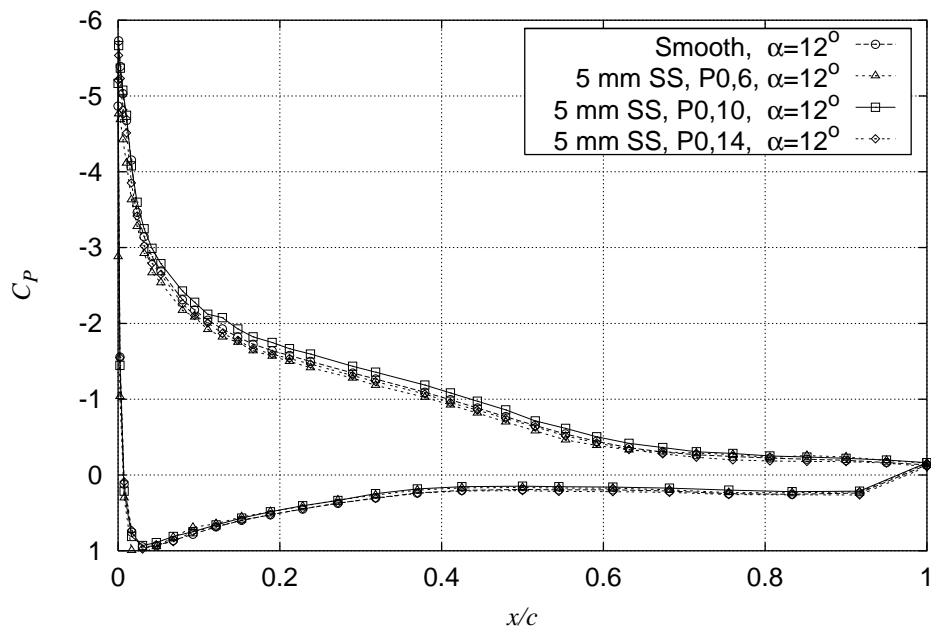
Figure 6-28 C_P at α = 12° for NACA 63-415, 5mm Stall strips measurements compared with smooth flow.

Figure 6-29 C_P at $\alpha = 16°$ for NACA 63-415, 5mm Stall strips measurements compared with smooth flow.

Figure 6-30 C_L-C_D for NACA 63-415, 5mm Stall strips measurements compared with smooth flow.
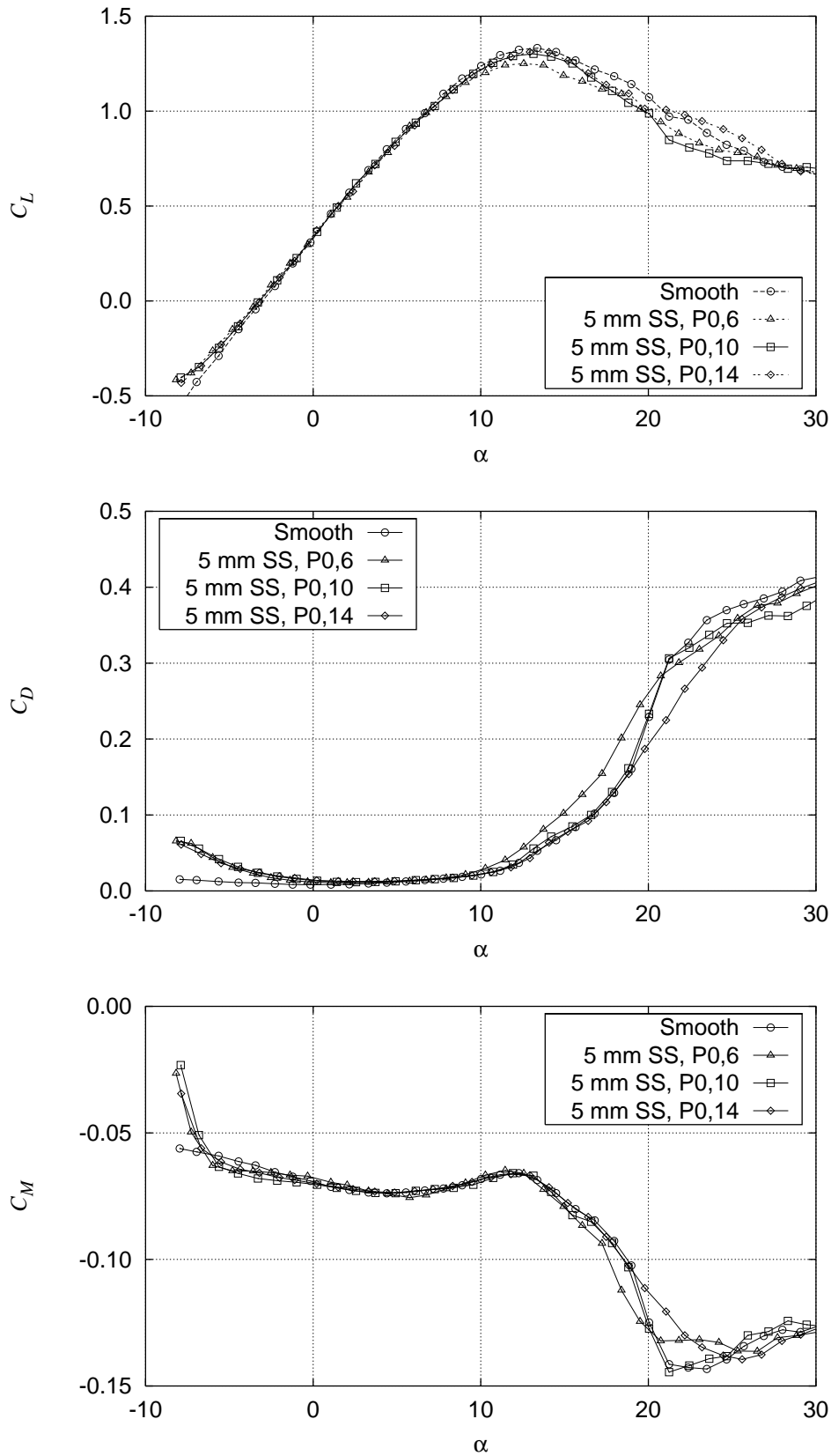
Figure 6-31 C_L, C_D and C_M for NACA 63-415, 5mm Stall strips measurements compared with smooth flow.

6.7 NACA 63-415, dynamic stall (run064)
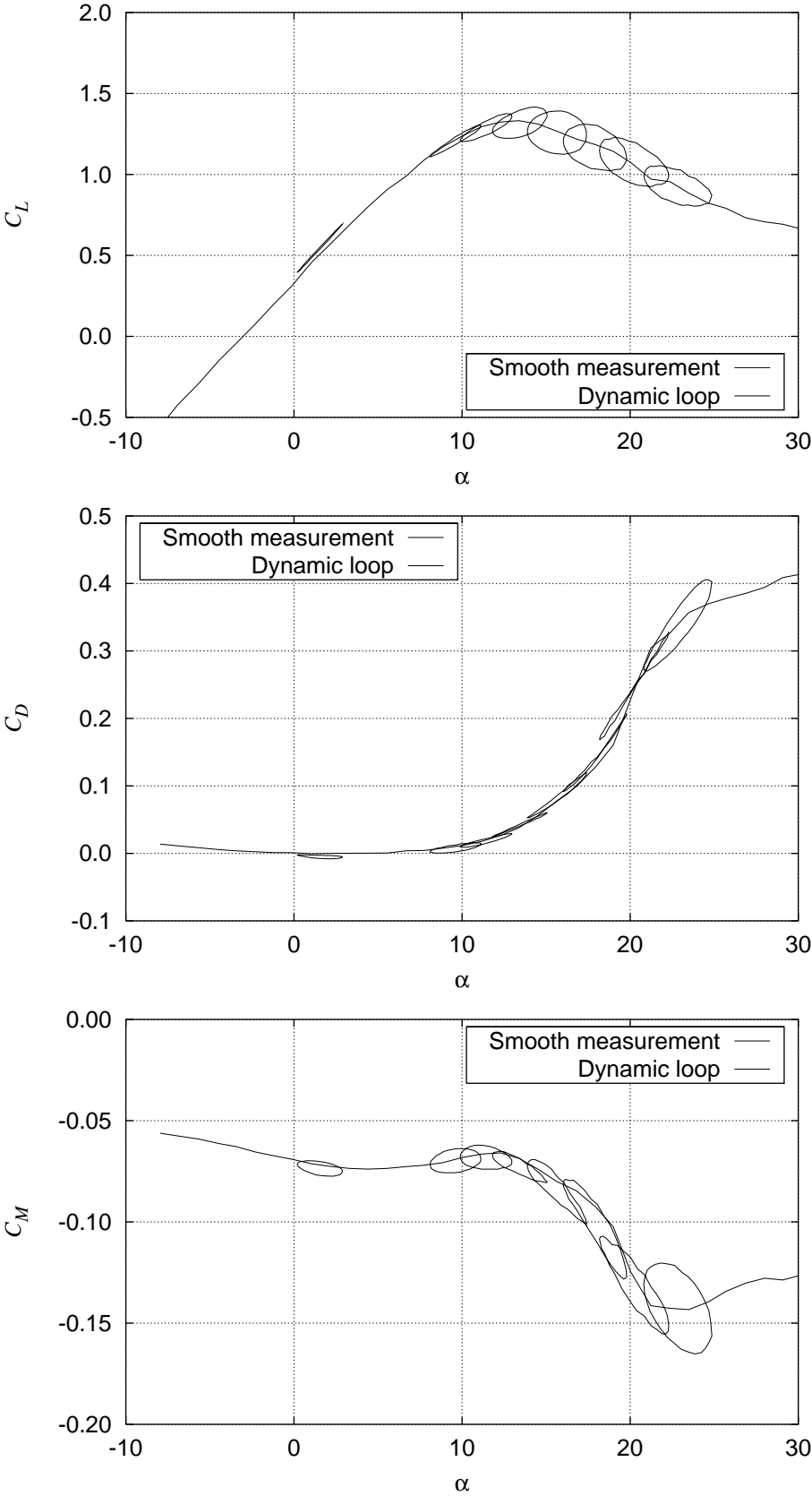
Figure 6-32 C_L, C_D and C_M hysteresis loops for NACA 63-415 smooth measurements at k = 0.092, A between 1.3° and 2.1° (run064).
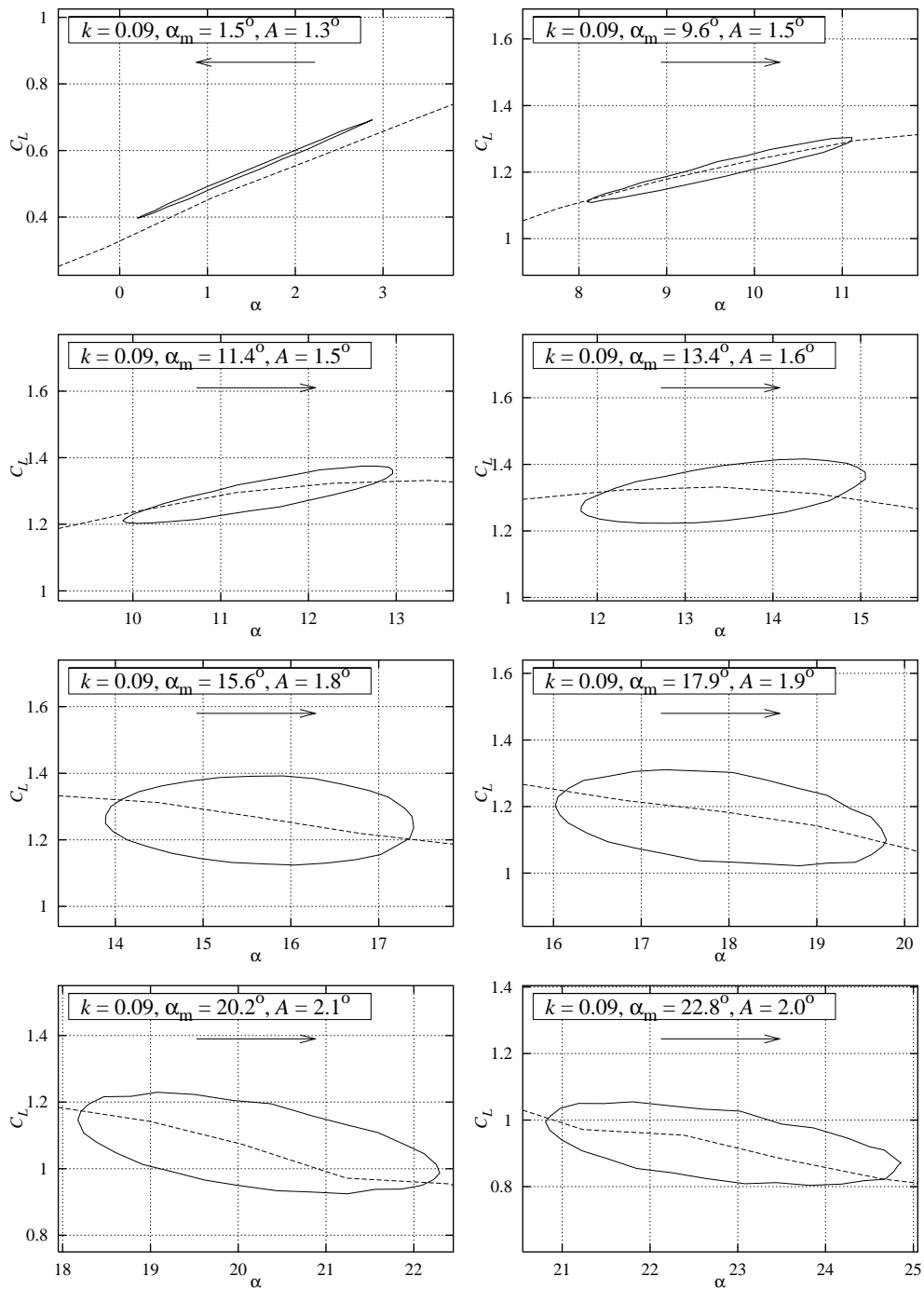
Figure 6-33 C_L hysteresis loops for NACA 63-415 smooth measurements at k = 0.09, A between 1.3° and 2.1° (run064).
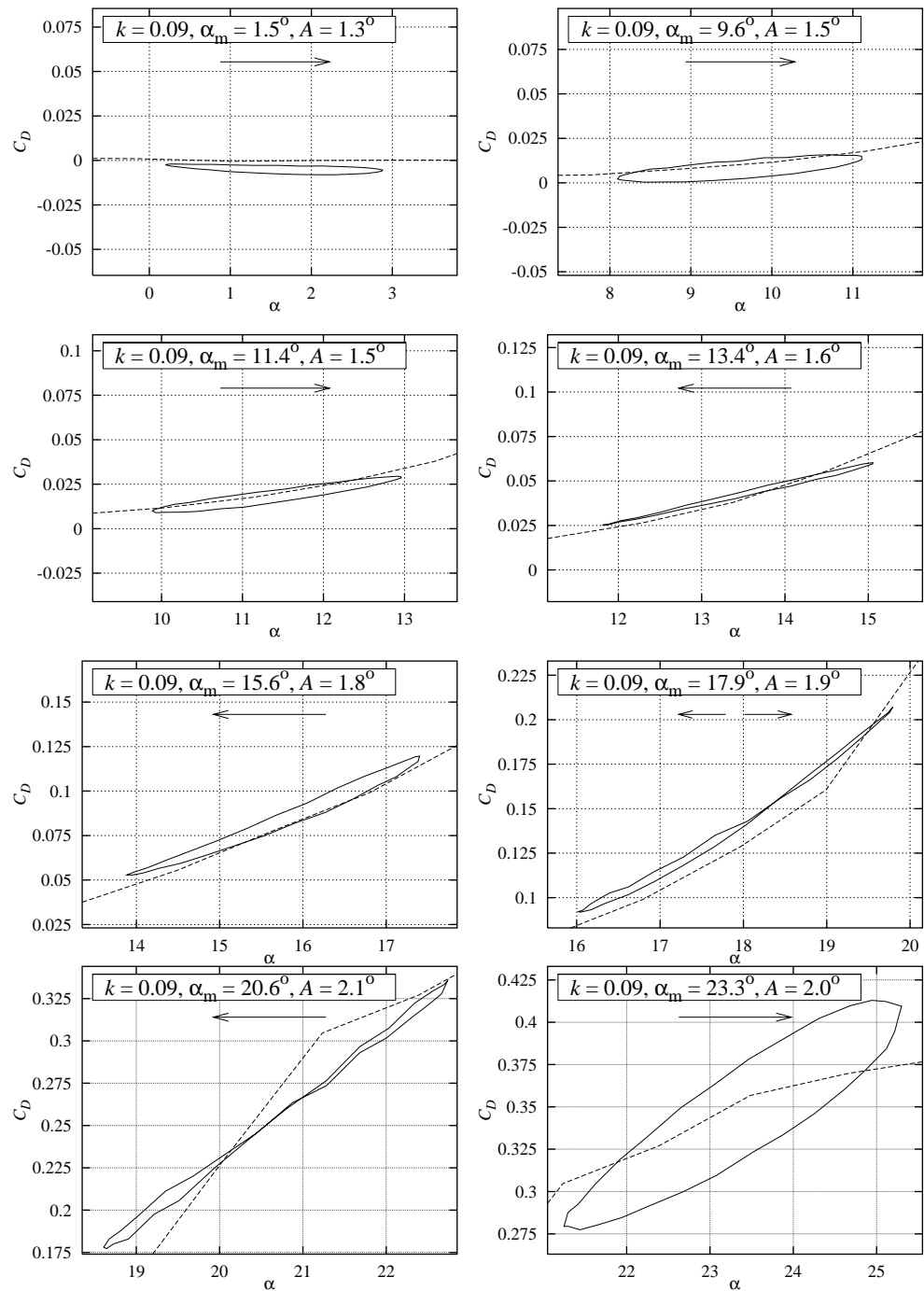
Figure 6-34 C_D hysteresis loops for NACA 63-415 smooth measurements at k = 0.09, A between 1.3° and 2.1° (run064).
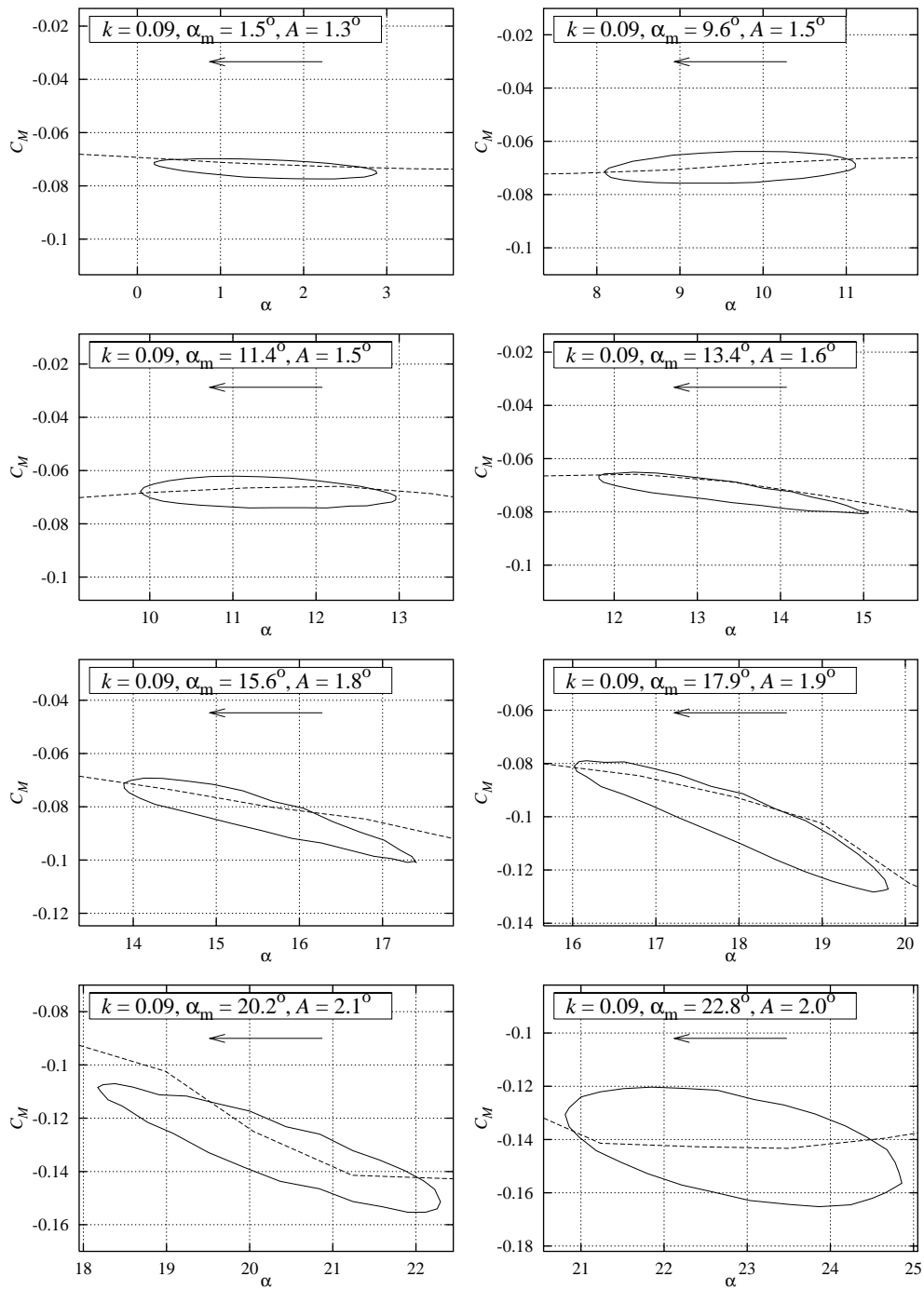
Figure 6-35 C_M hysteresis loops for NACA 63-415 smooth measurements at k = 0.09, A between 1.3° and 2.1° (run064).

6.8 NACA 63-415, stall characteristics (run065, 096)
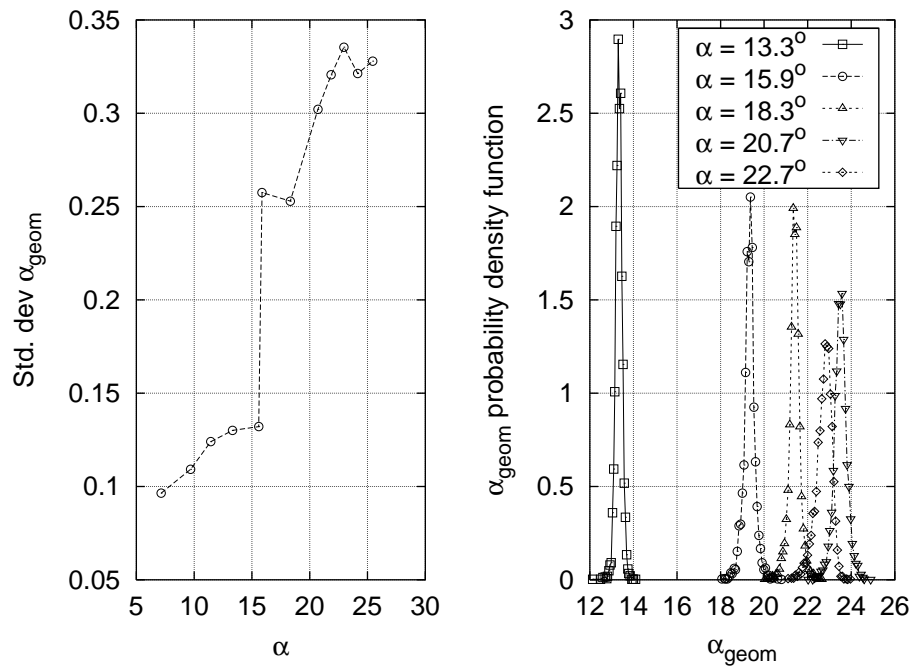
Figure 6-36 NACA 63-415 smooth. Left: Standard deviation of geometrical α as function of mean α. Right: Probability density function of geometrical α at different corrected mean α.
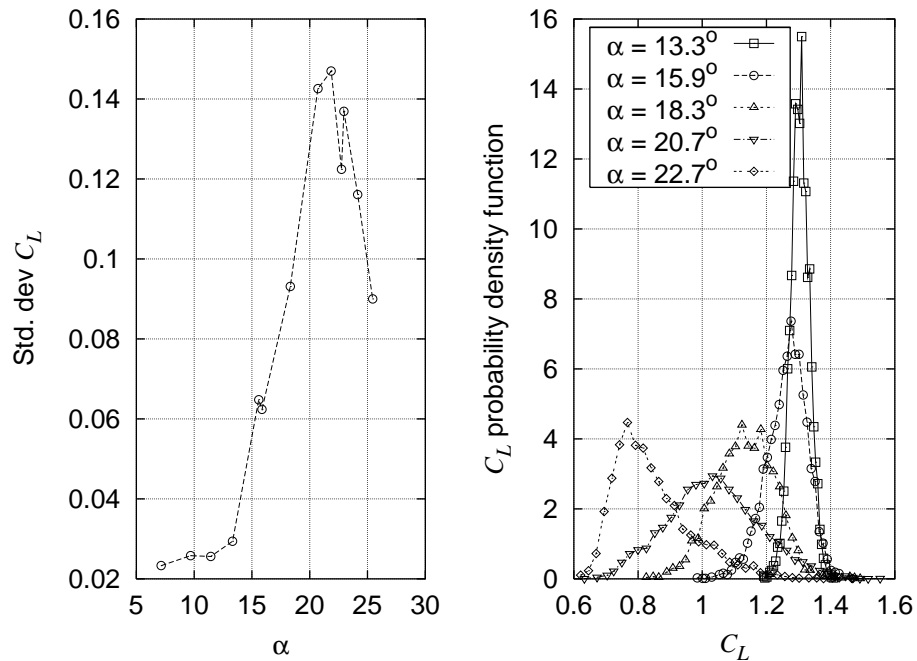
Figure 6-37 NACA 63-415 smooth. Left: Standard deviation of C_L as function of mean α. Right: Probability density function of C_L at mean α.
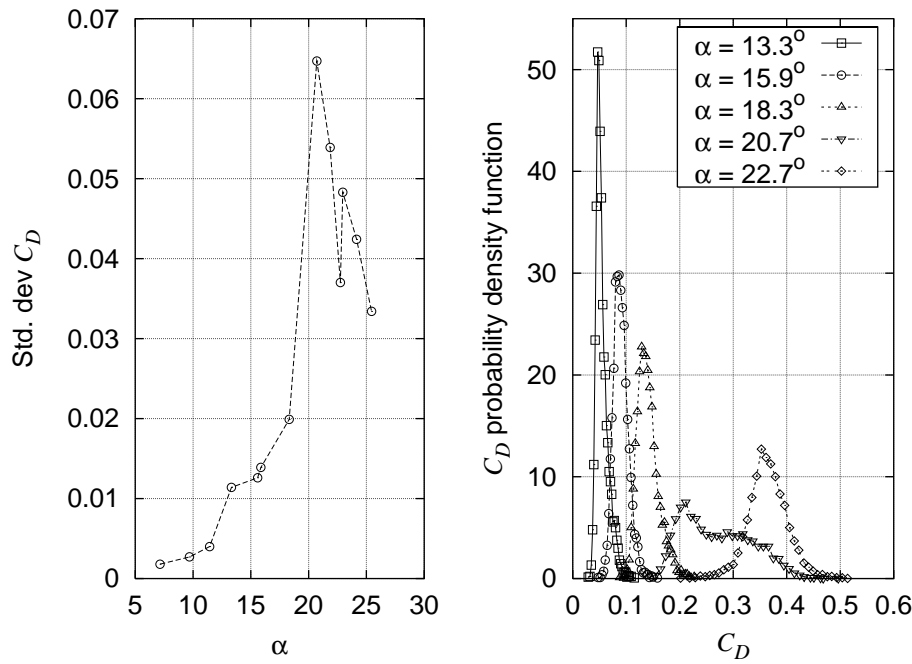
Figure 6-38 NACA 63-415 smooth. Left: Standard deviation of C_D as function of mean α. Right: Probability density function of C_D at different mean α.
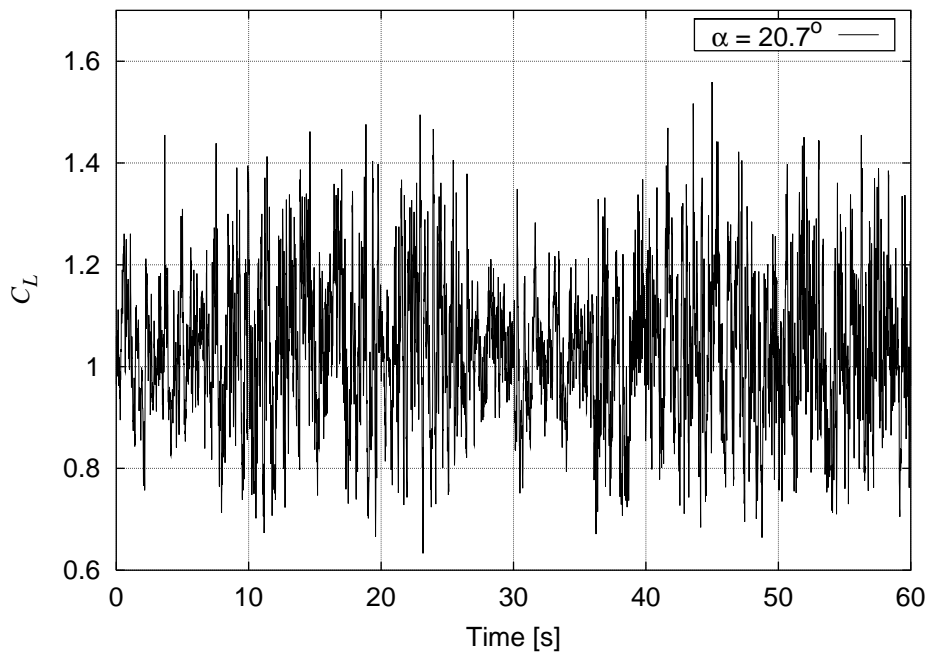
Figure 6-39 NACA 63-415 smooth: Time series of C_L for mean $\alpha = 20.7°$.
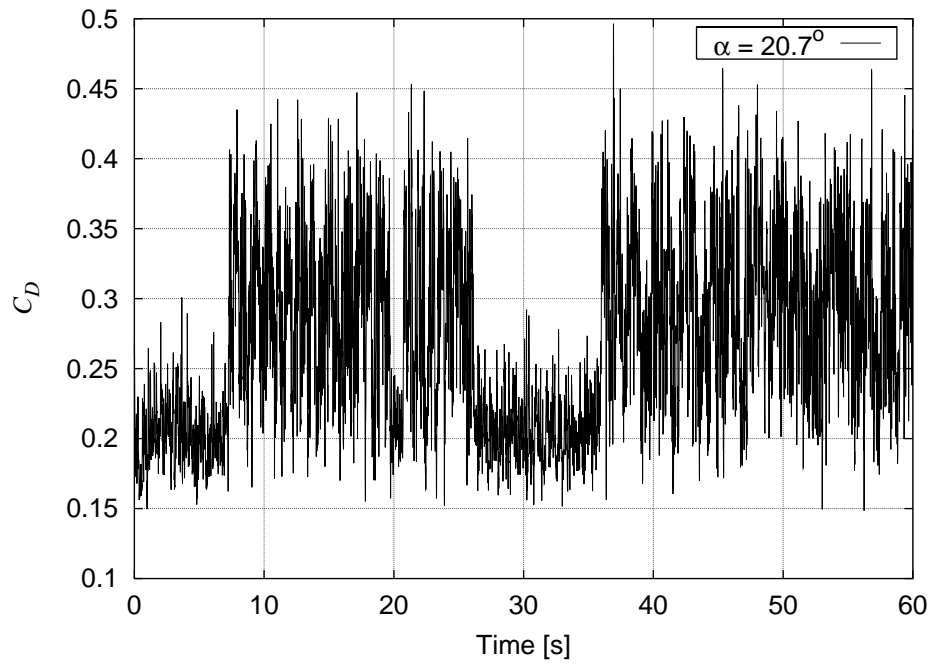
Figure 6-40 NACA 63-415 smooth: Time series of C_D for mean $\alpha = 20.7\,°$.

7 Results for NACA 63-415-Risø-D

7.1 NACA 63-415-Risø-D, smooth flow (run002)
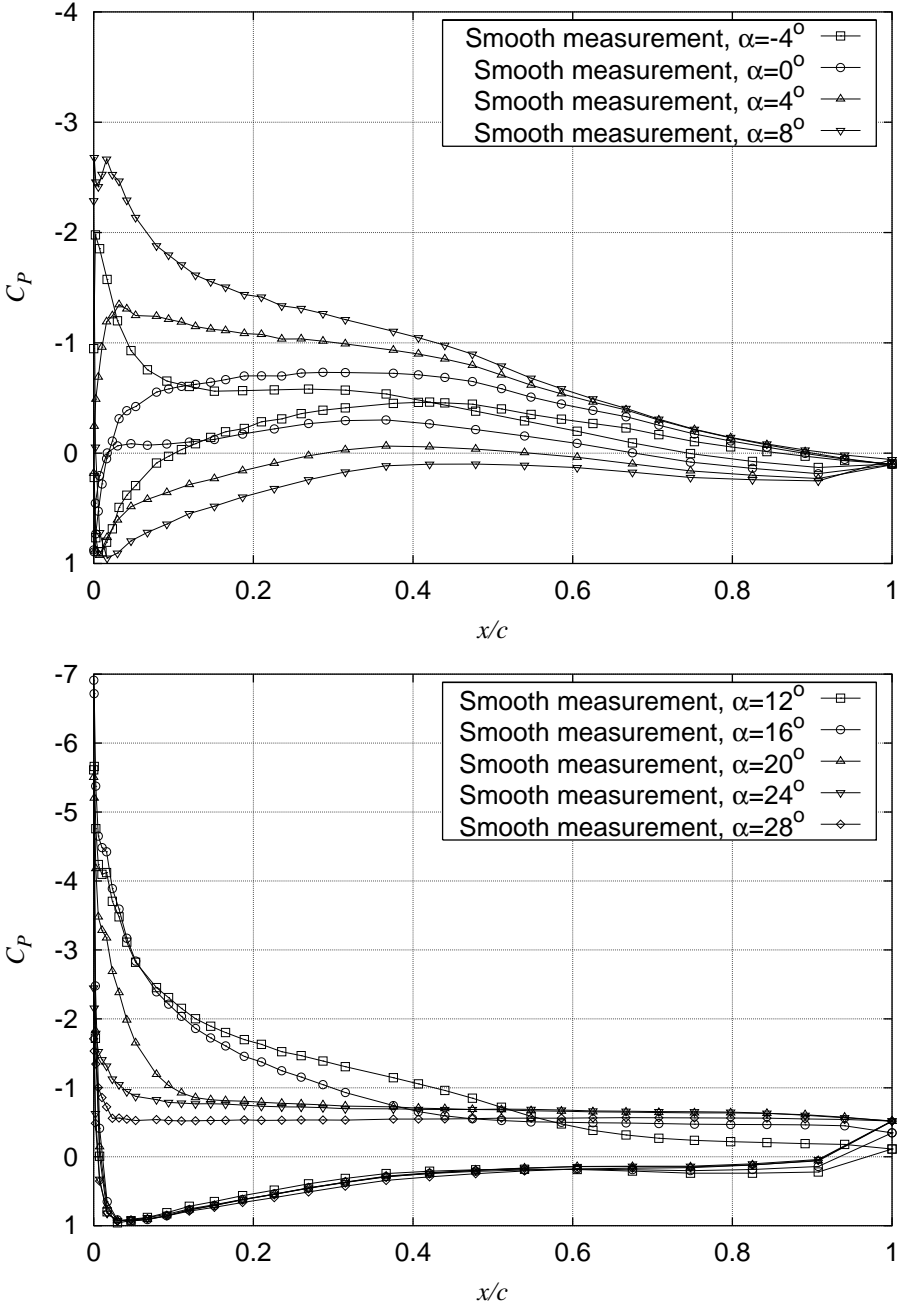
Figure 7-1 C$_P$ at different angles of attack for NACA 63-415-Risø-D smooth measurements.
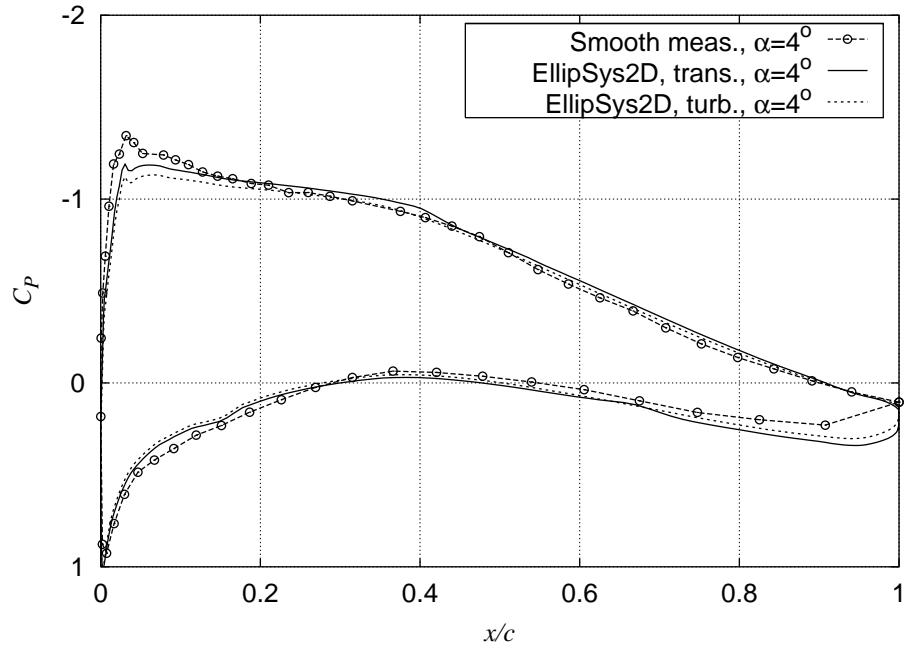
Figure 7-2 C_P at $\alpha = 4°$ for NACA 63-415-Risø-D smooth measurements compared with EllipSys2D calculations with transition model and turbulent flow, respectively.
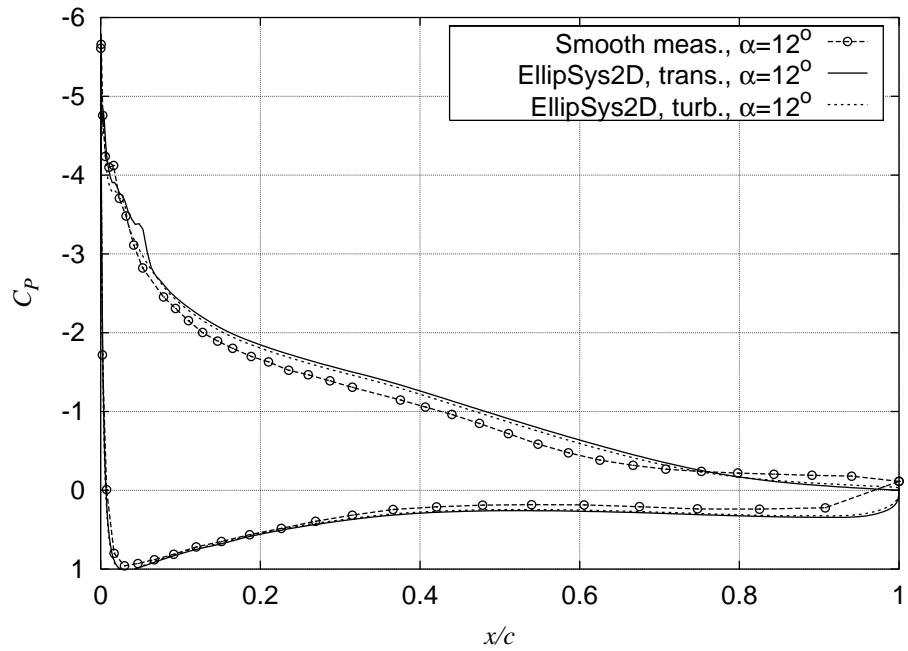
Figure 7-3 C_P at $\alpha = 12°$ for NACA 63-415-Risø-D smooth measurements compared with EllipSys2D calculations with transition model and turbulent flow, respectively.
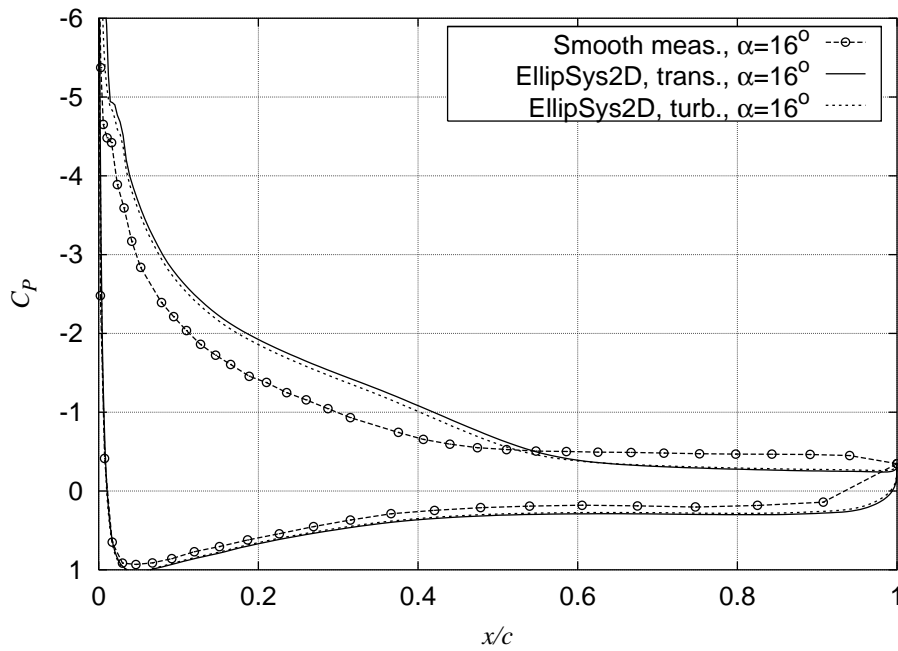
Figure 7-4 C_P at $\alpha = 16°$ for NACA 63-415-Risø-D smooth measurements compared with EllipSys2D calculations with transition model and turbulent flow, respectively.
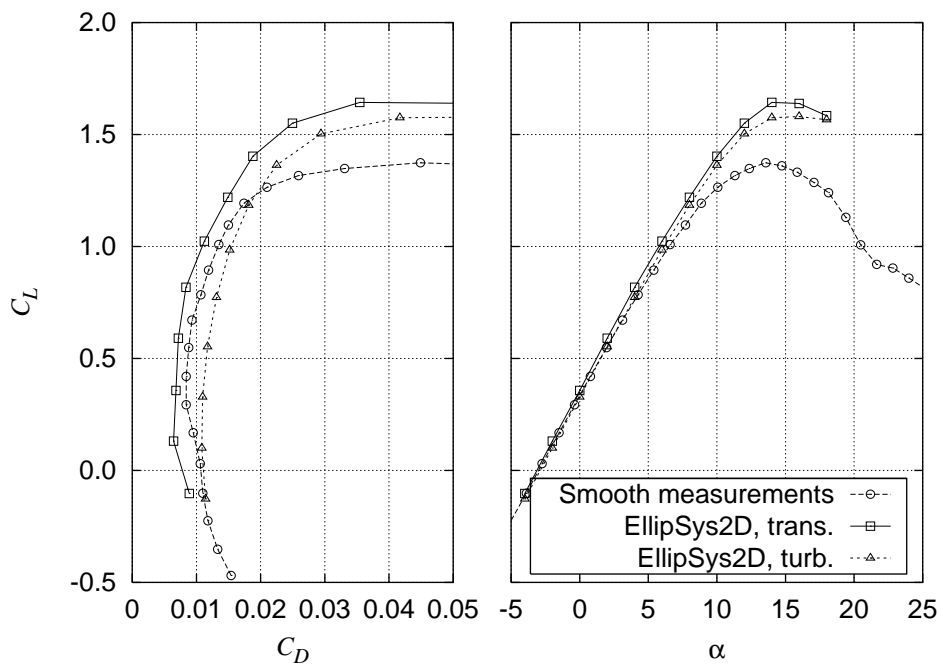
Figure 7-5 C_L-C_D for NACA 63-415-Risø-D smooth measurements compared with EllipSys2D calculations with transition model and turbulent flow, respectively.
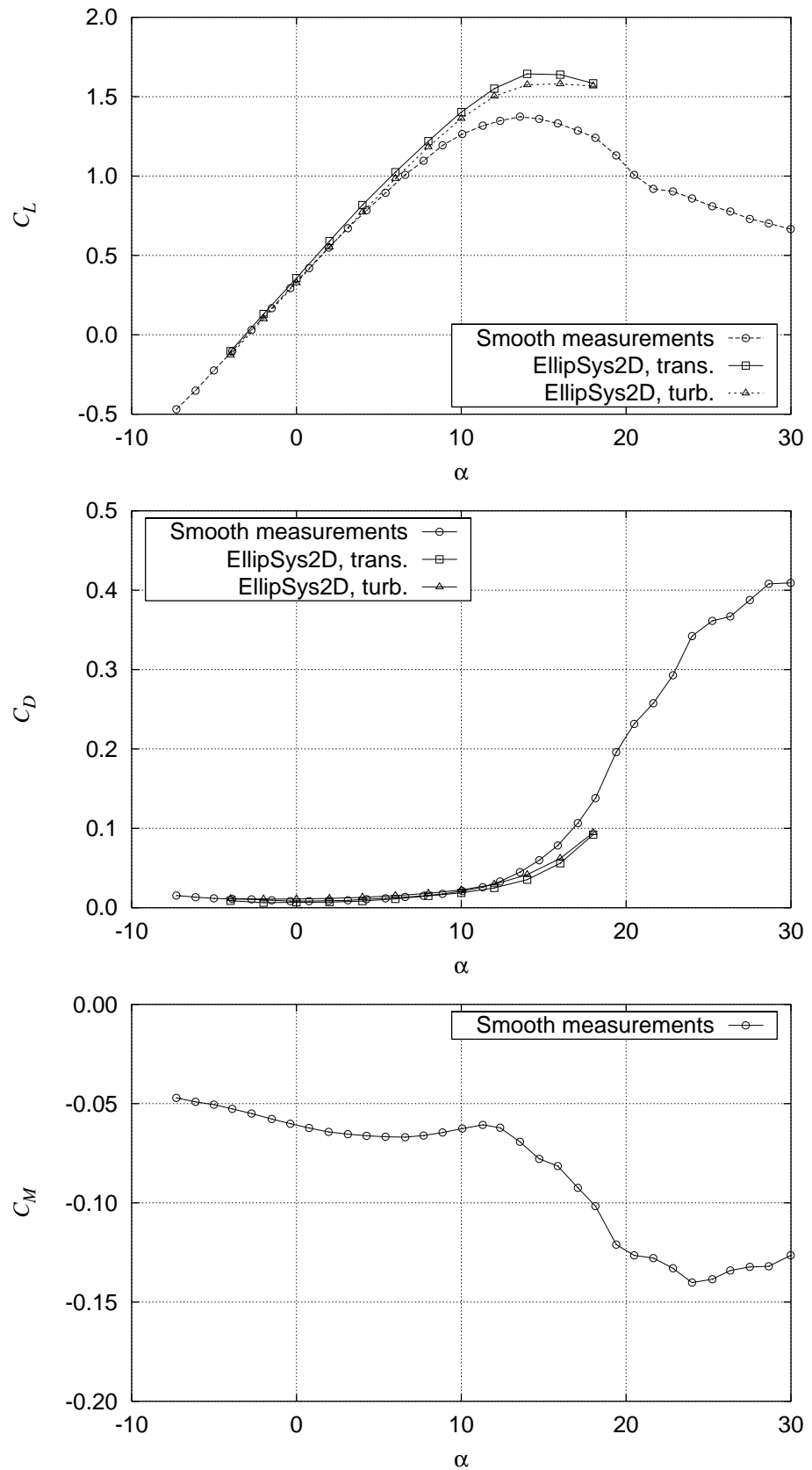
Figure 7-6 C_L, C_D and C_M for NACA 63-415-Risø-D smooth measurements compared with EllipSys2D calculations with transition model and turbulent flow, respectively.

7.2 NACA 63-415-Risø-D, LER zigzag tape 90° (run008, 009, 010)
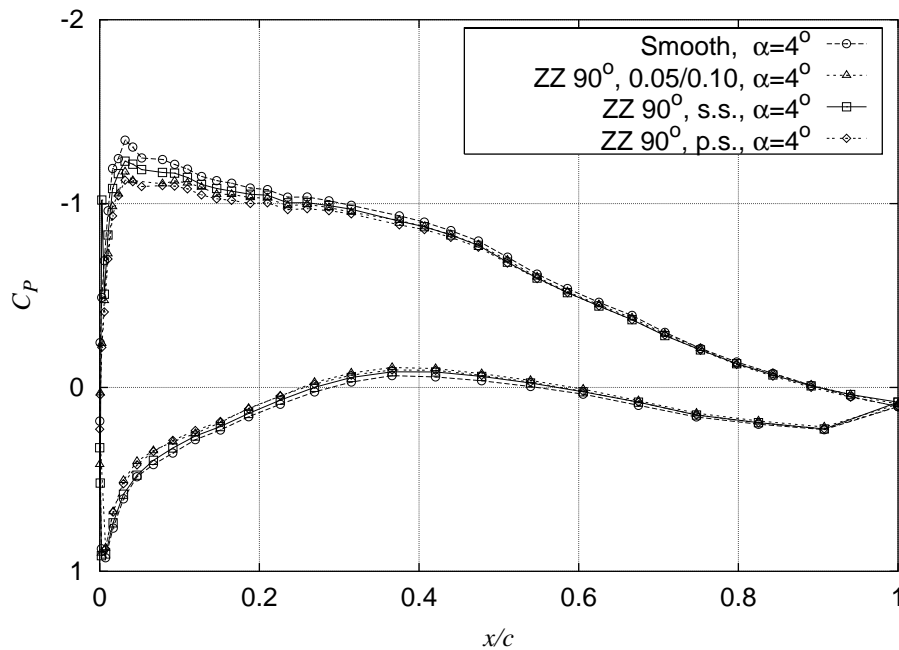
Figure 7-7 C_P at α = 4° for NACA 63-415-Risø-D, ZZ90° LER measurements compared with smooth flow.
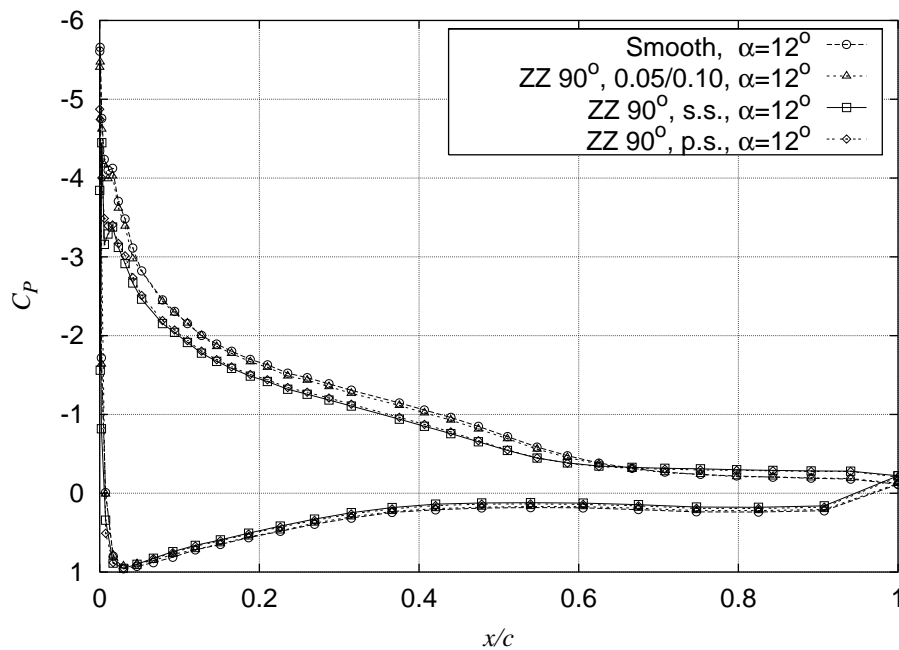
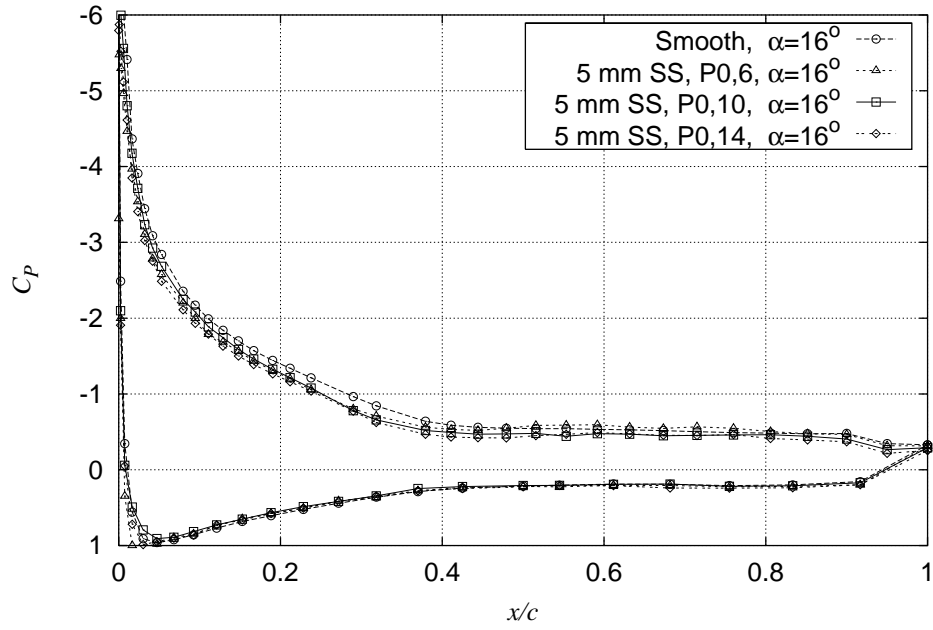*Figure 7-8 C_P at α = 12° for NACA 63-415-Risø-D, ZZ90° LER measurements compared with smooth flow.*

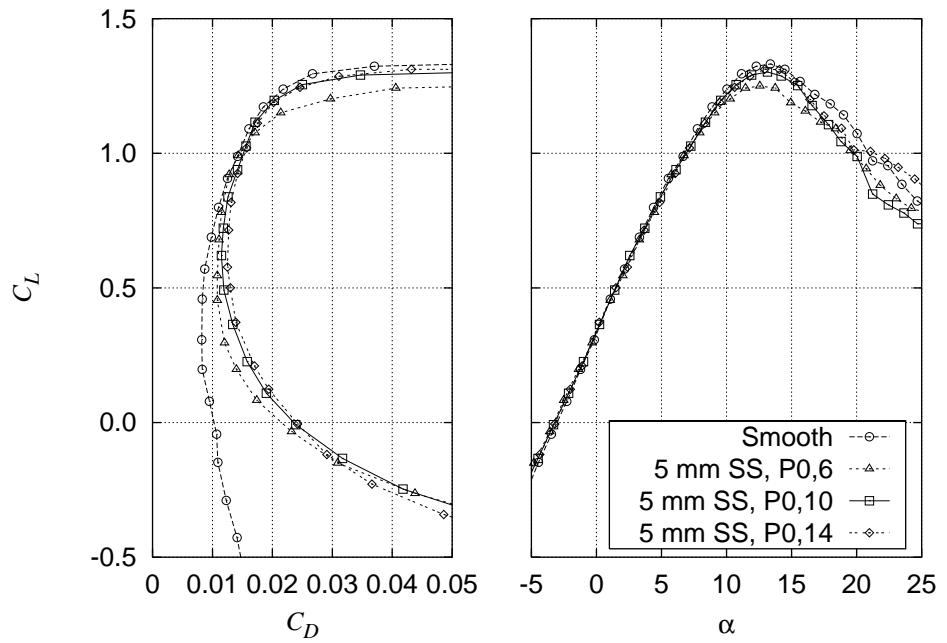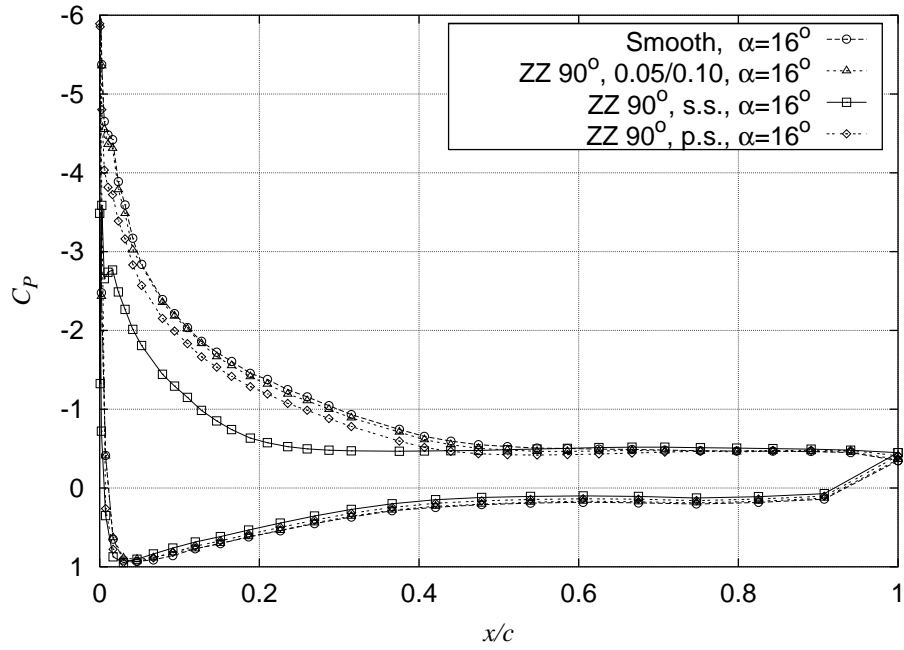*Figure 7-9 C_P at $\alpha = 16°$ for NACA 63-415-Risø-D, ZZ90° LER measurements compared with smooth flow.*
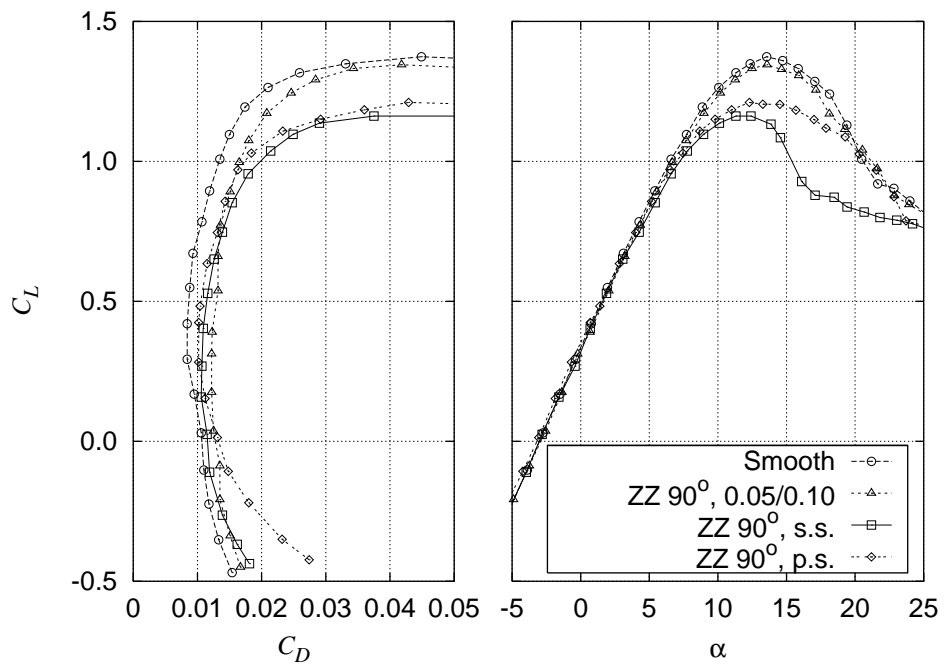
Figure 7-10 C_L-C_D for NACA 63-415-Risø-D, ZZ90° LER measurements compared with smooth flow.
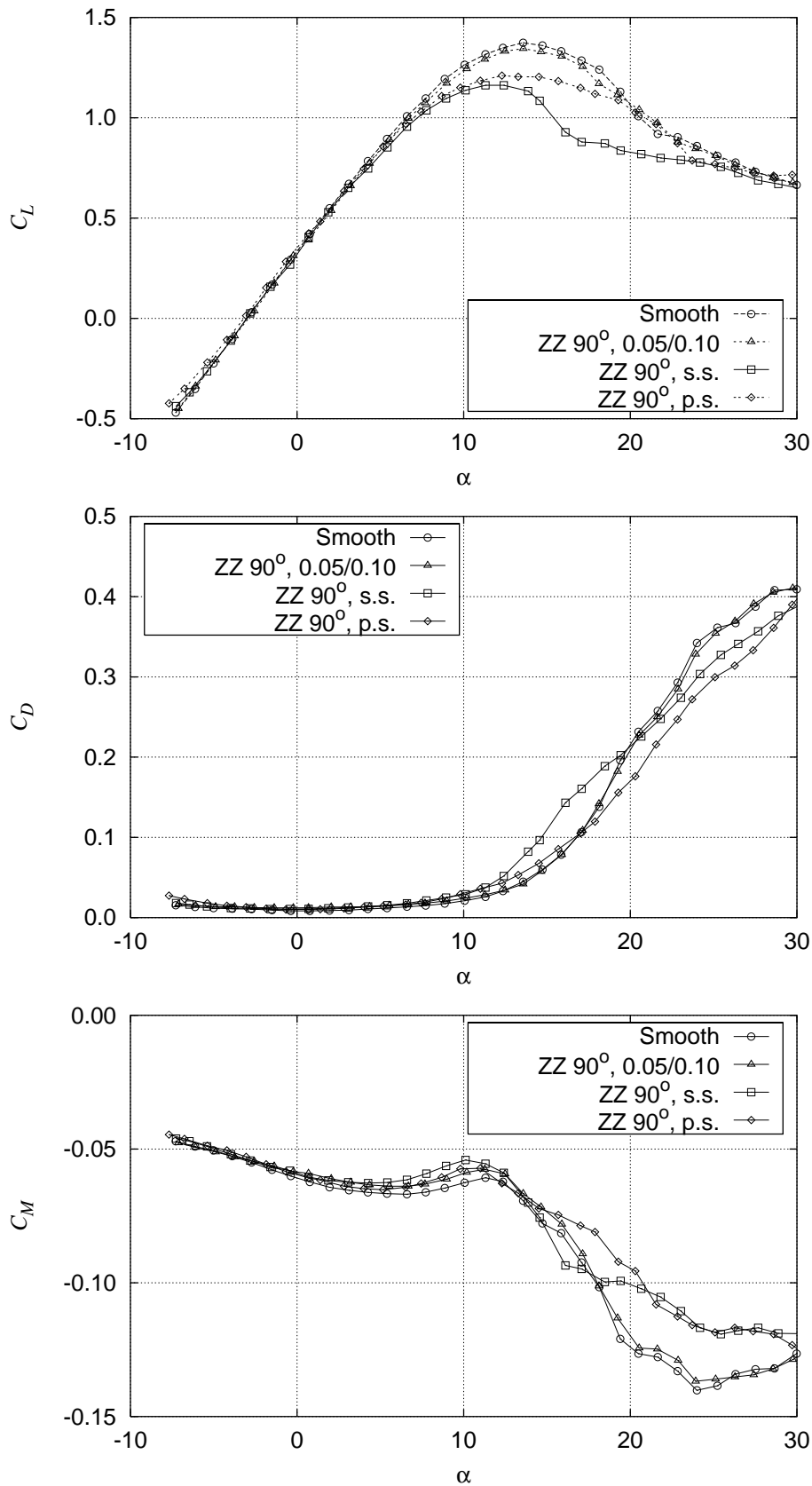
Figure 7-11 C_L, C_D and C_M for NACA 63-415-Risø-D, ZZ90° LER measurements compared with smooth flow.

7.3 NACA 63-415-Risø-D, LER on pressure side (run010, 017, 019)
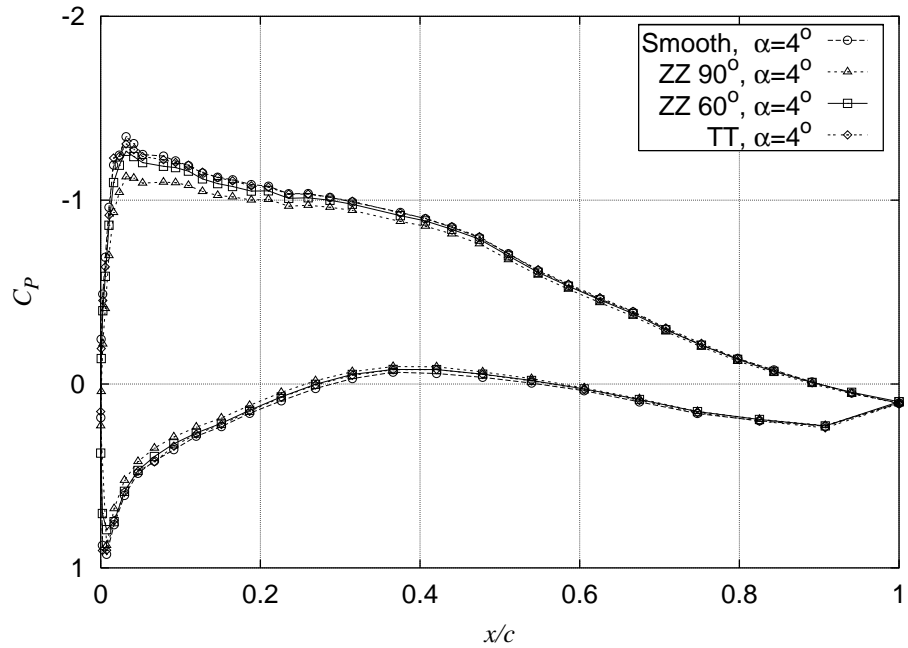
Figure 7-12 C_P at $\alpha = 4°$ for NACA 63-415-Risø-D, LER on pressure side measurements compared with smooth flow.
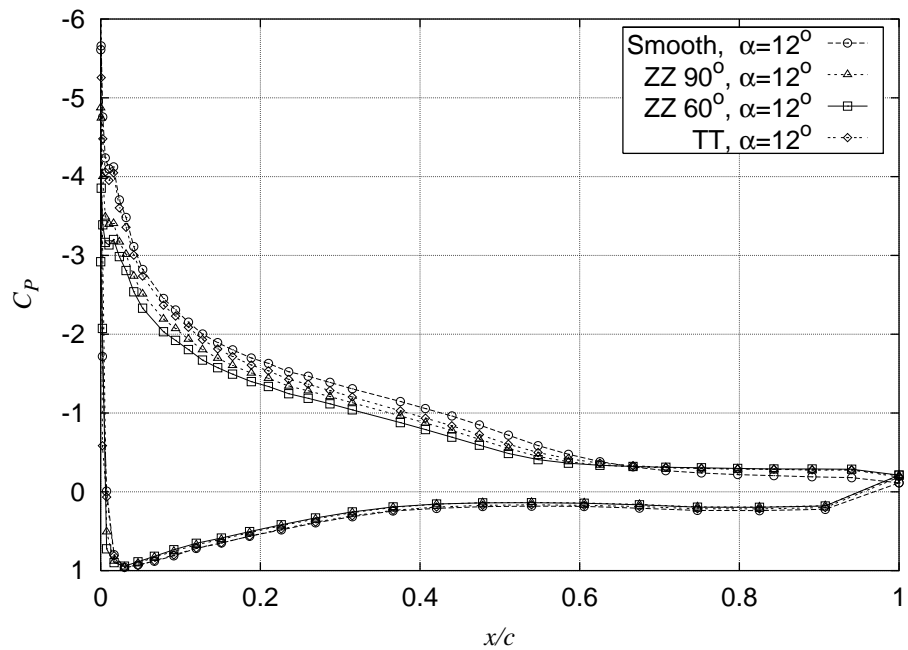
Figure 7-13 C_P at $\alpha = 12°$ for NACA 63-415-Risø-D, LER on pressure side measurements compared with smooth flow.
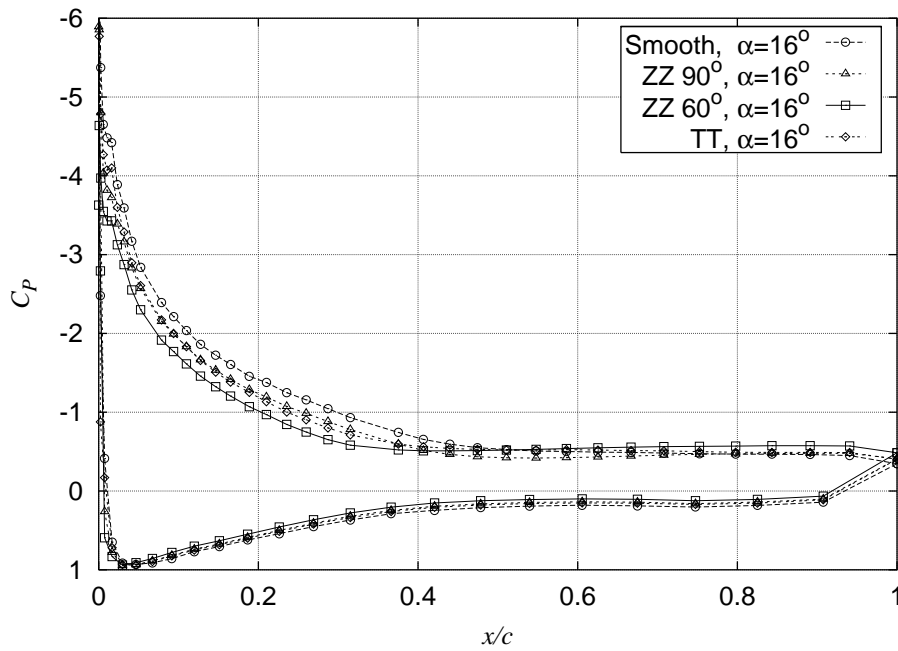
Figure 7-14 C_P at $\alpha = 16°$ for NACA 63-415-Risø-D, LER on pressure side measurements compared with smooth flow.
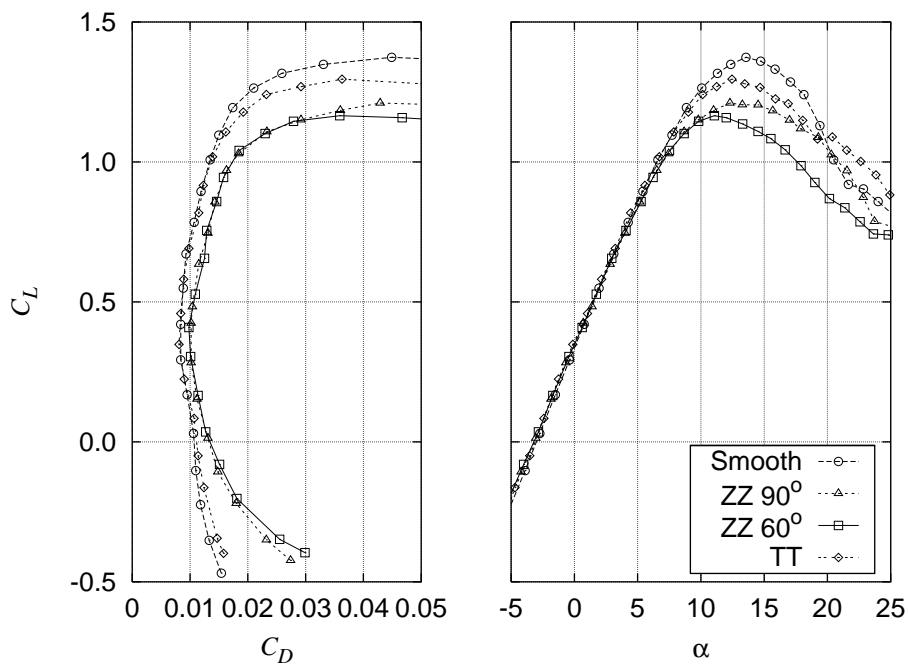
Figure 7-15 C_L-C_D for NACA 63-415-Risø-D, LER on pressure side measurements compared with smooth flow.
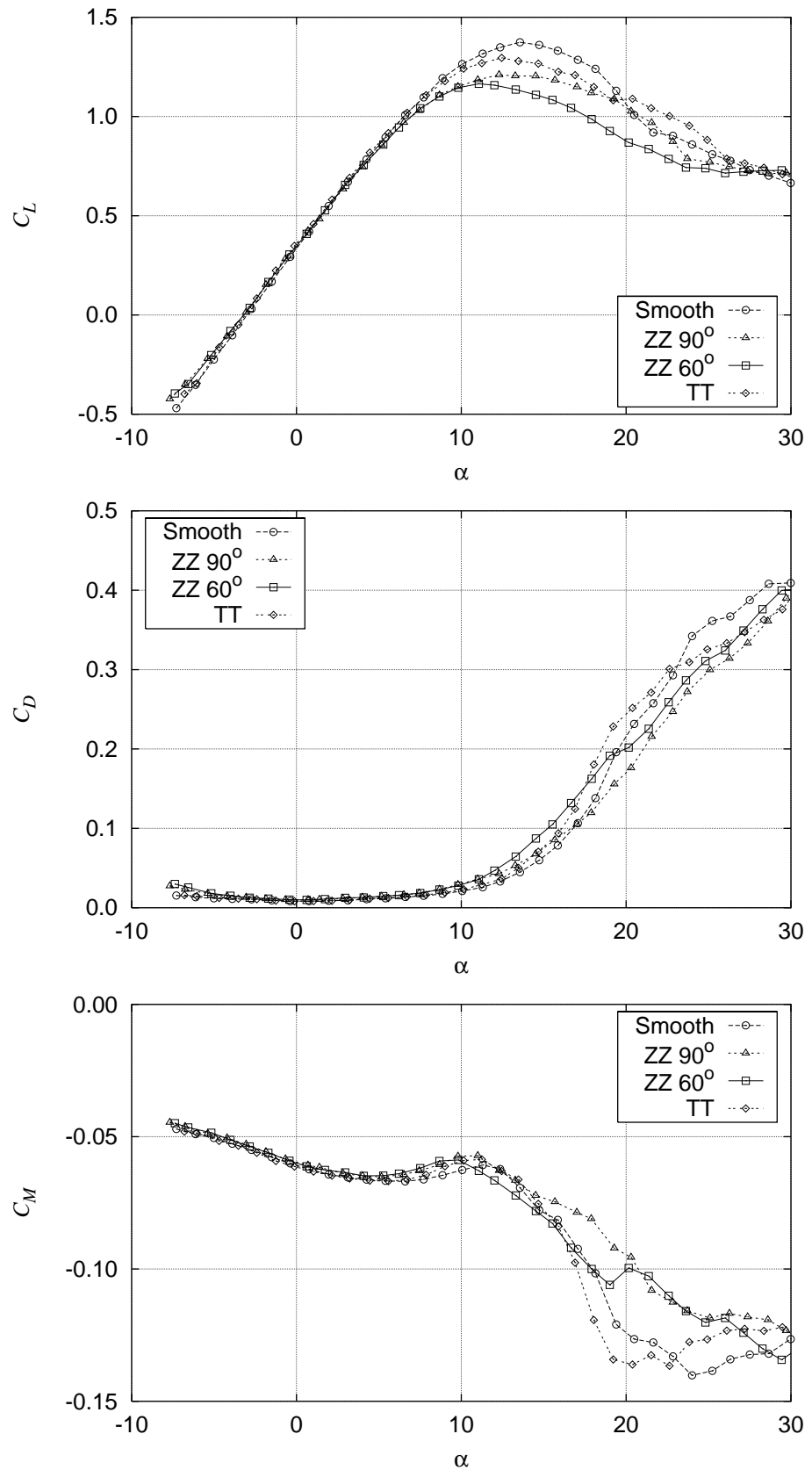
Figure 7-16 C_L, C_D and C_M for NACA 63-415-Risø-D, LER on pressure side measurements compared with smooth flow.

7.4 NACA 63-415-Risø-D, 7 mm stall strips (run012, 016)
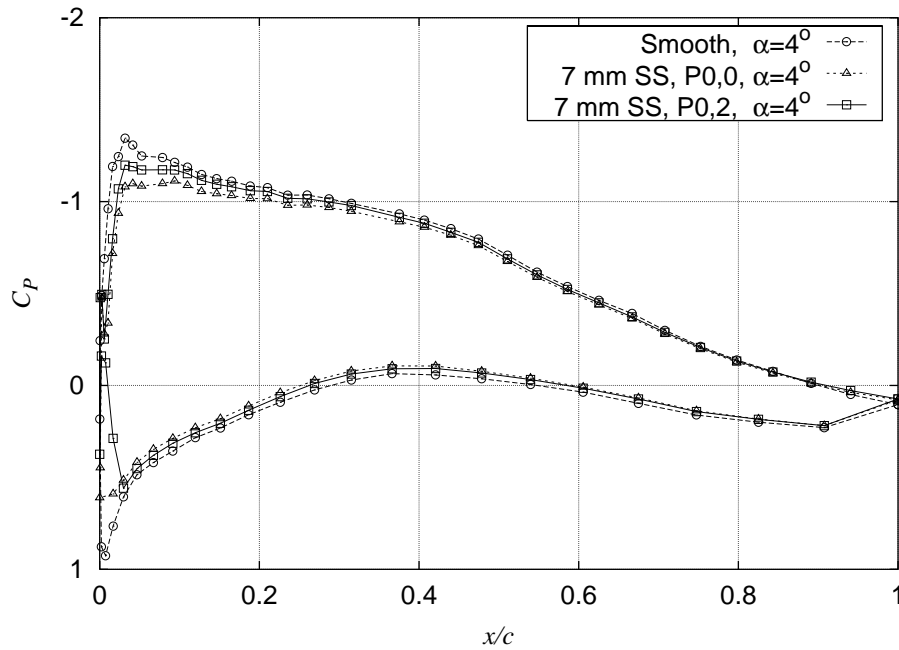
Figure 7-17 C_P at $\alpha = 4°$ for NACA 63-415-Risø-D, 7mm Stall strips measurements compared with smooth flow.
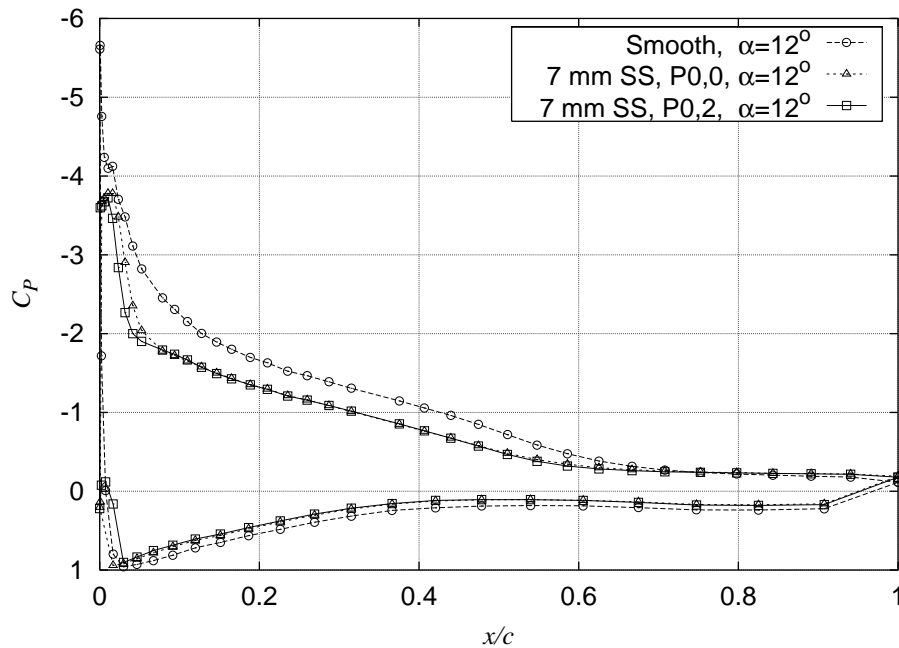
Figure 7-18 C_P at $\alpha = 12°$ for NACA 63-415-Risø-D, 7mm Stall strips measurements compared with smooth flow.
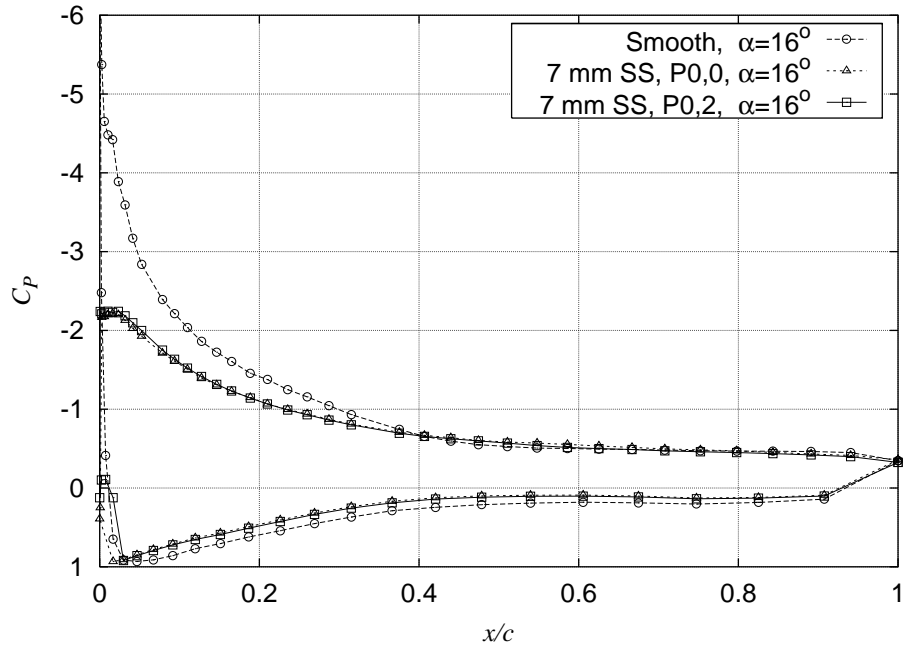
Figure 7-19 C_P at α = 16° for NACA 63-415-Risø-D, 7mm Stall strips measurements compared with smooth flow.
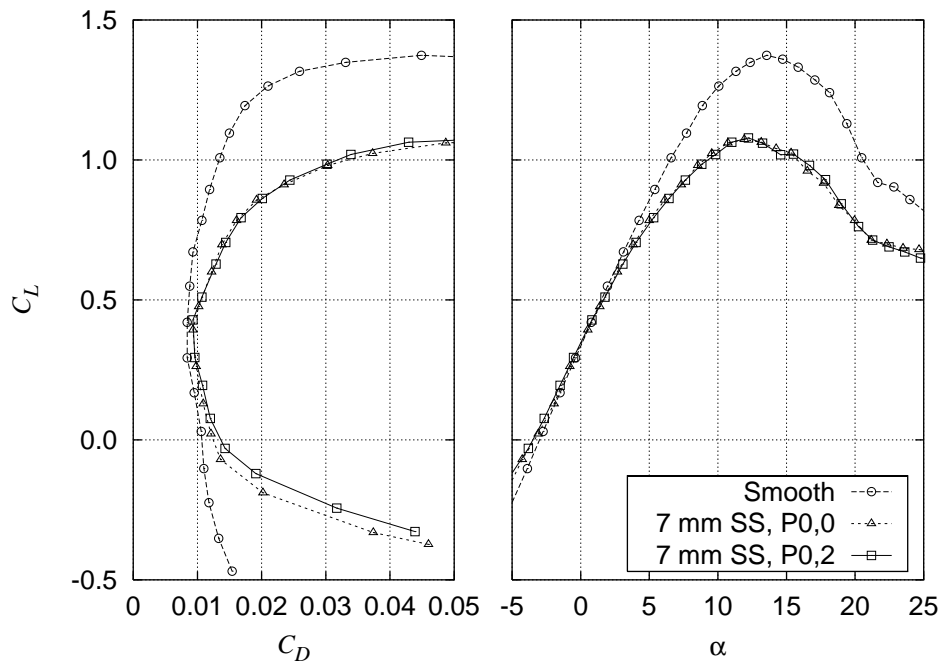
Figure 7-20 C_L-C_D for NACA 63-415-Risø-D, 7mm Stall strips measurements compared with smooth flow.
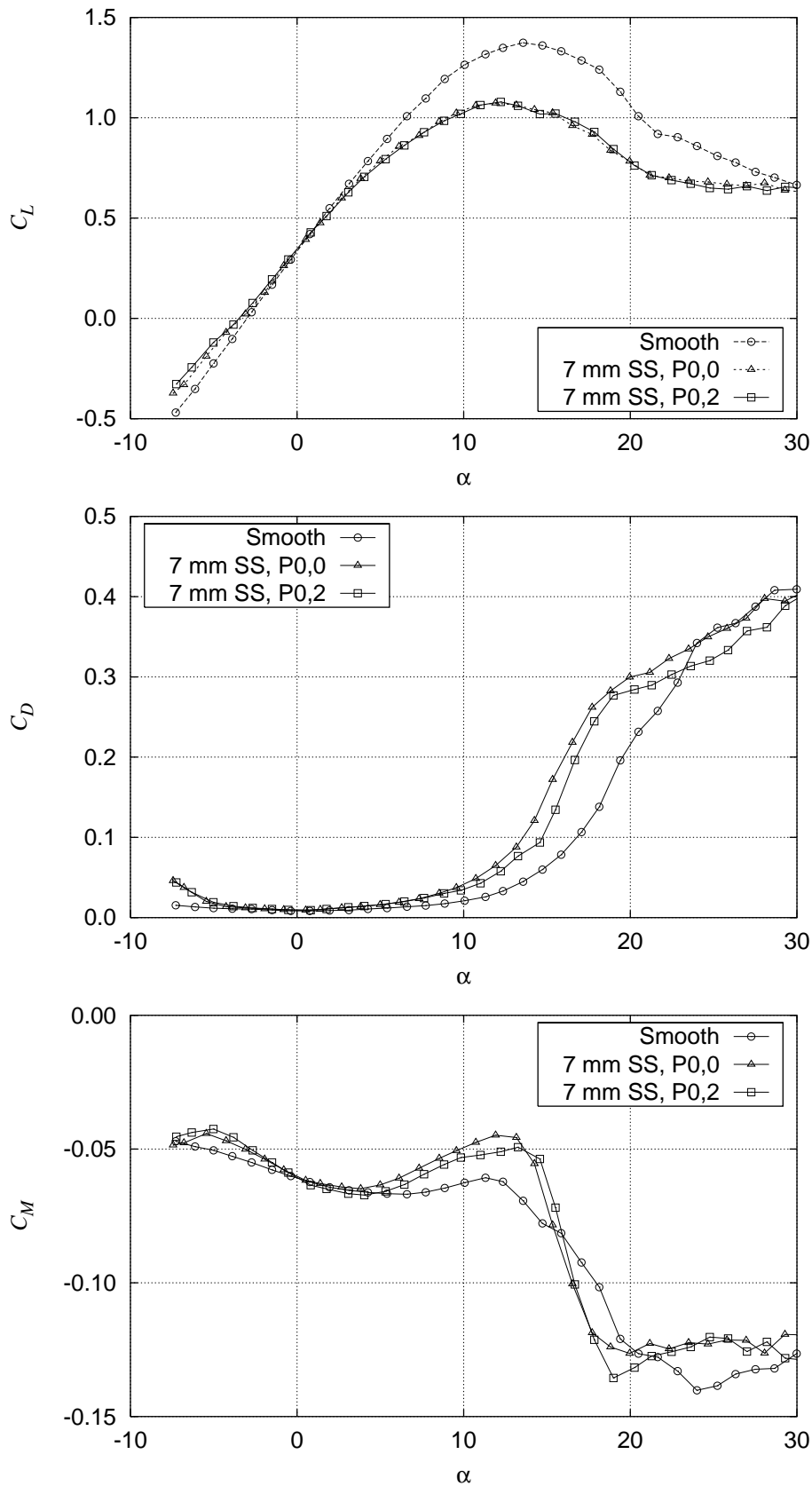
Figure 7-21 C_L, C_D and C_M for NACA 63-415-Risø-D, 7mm Stall strips measurement compared with smooth flow.

7.5 NACA 63-415-Risø-D, 5 mm stall strips (run013, 014, 018)
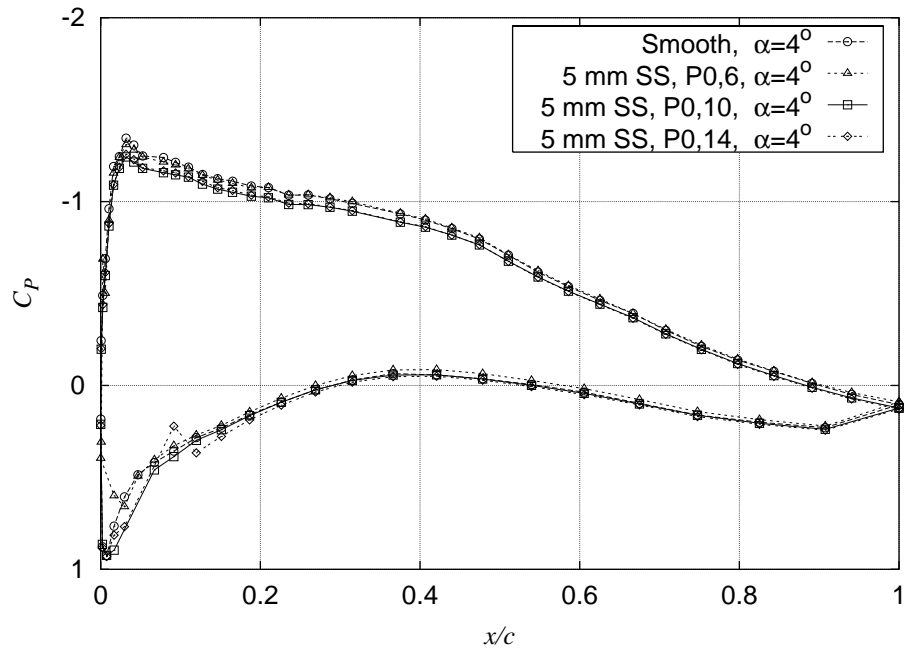
Figure 7-22 C_P at α = 4° for NACA 63-415-Risø-D, 5mm Stall strips measurements compared with smooth flow.
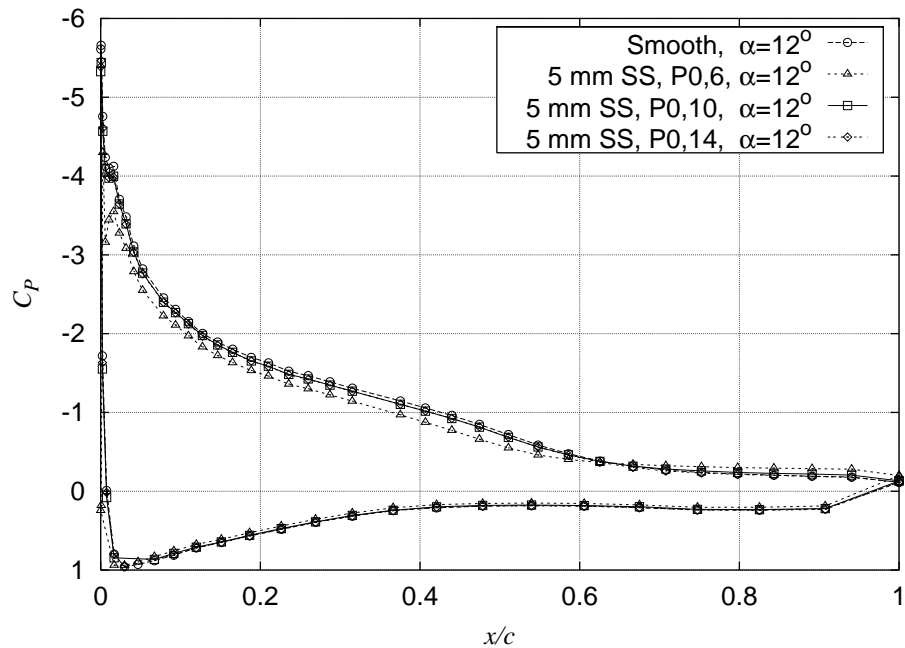
Figure 7-23 C_P at α = 12° for NACA 63-415-Risø-D, 5mm Stall strips measurements compared with smooth flow.
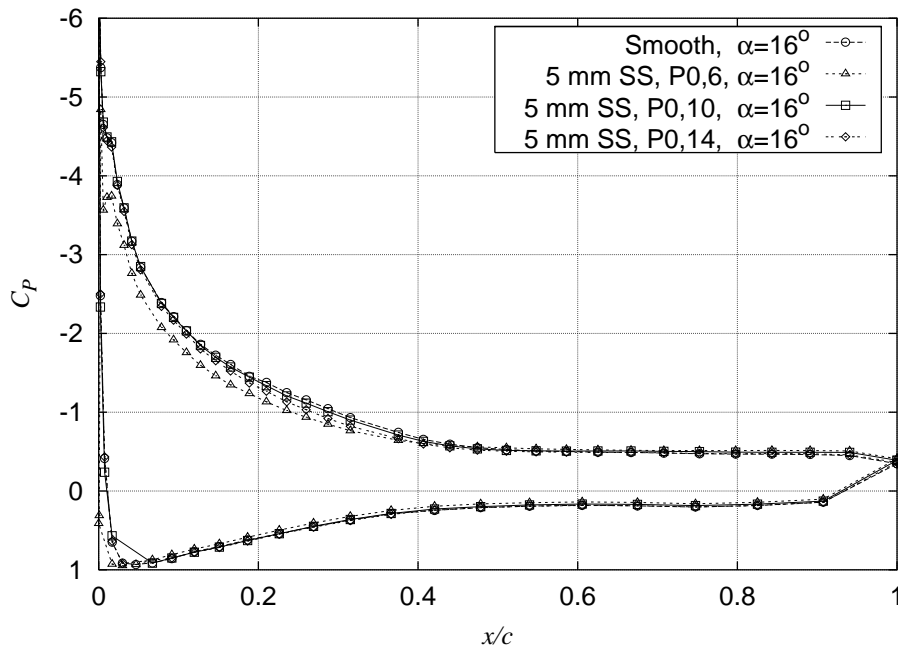
Figure 7-24 C_P at $\alpha = 16°$ for NACA 63-415-Risø-D, 5mm Stall strips measurements compared with smooth flow.
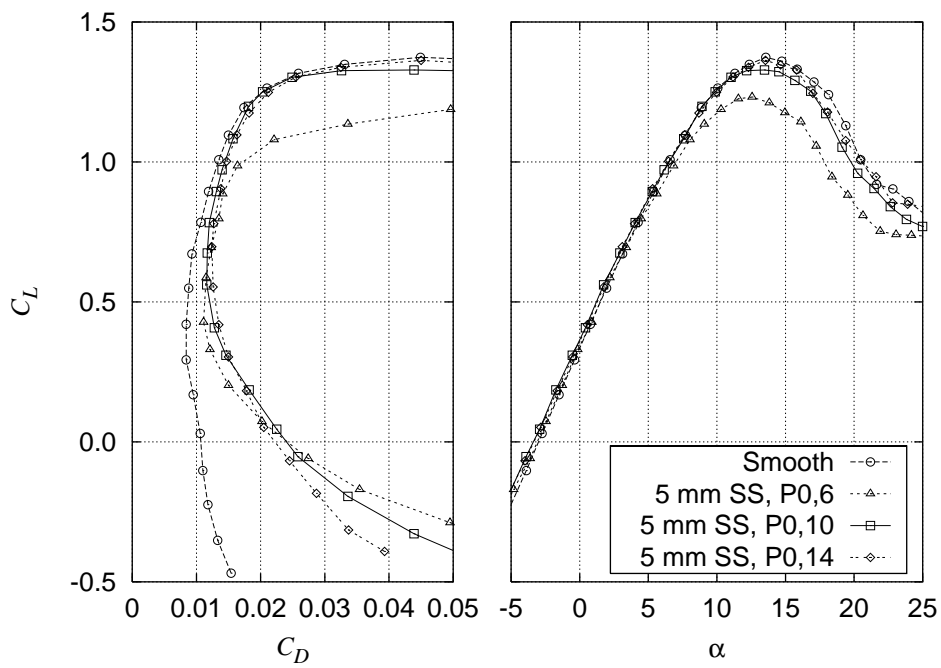
Figure 7-25 C_L-C_D for NACA 63-415-Risø-D, 5mm Stall strips measurements compared with smooth flow.
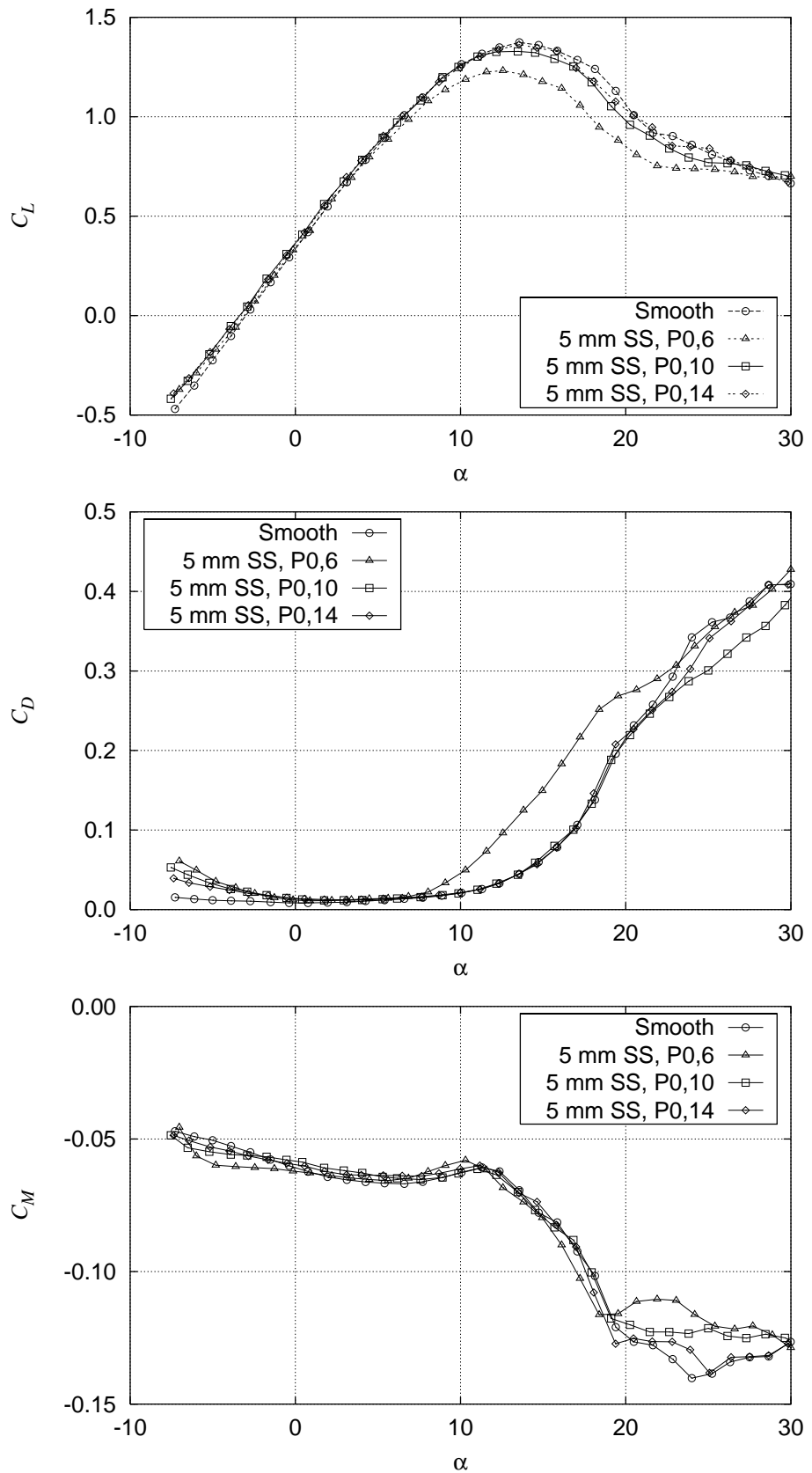
Figure 7-26 C_L, C_D and C_M for NACA 63-415-Risø-D, 5mm Stall strips measurement compared with smooth flow.

7.6 NACA 63-415-Risø-D, dynamic stall (run006)
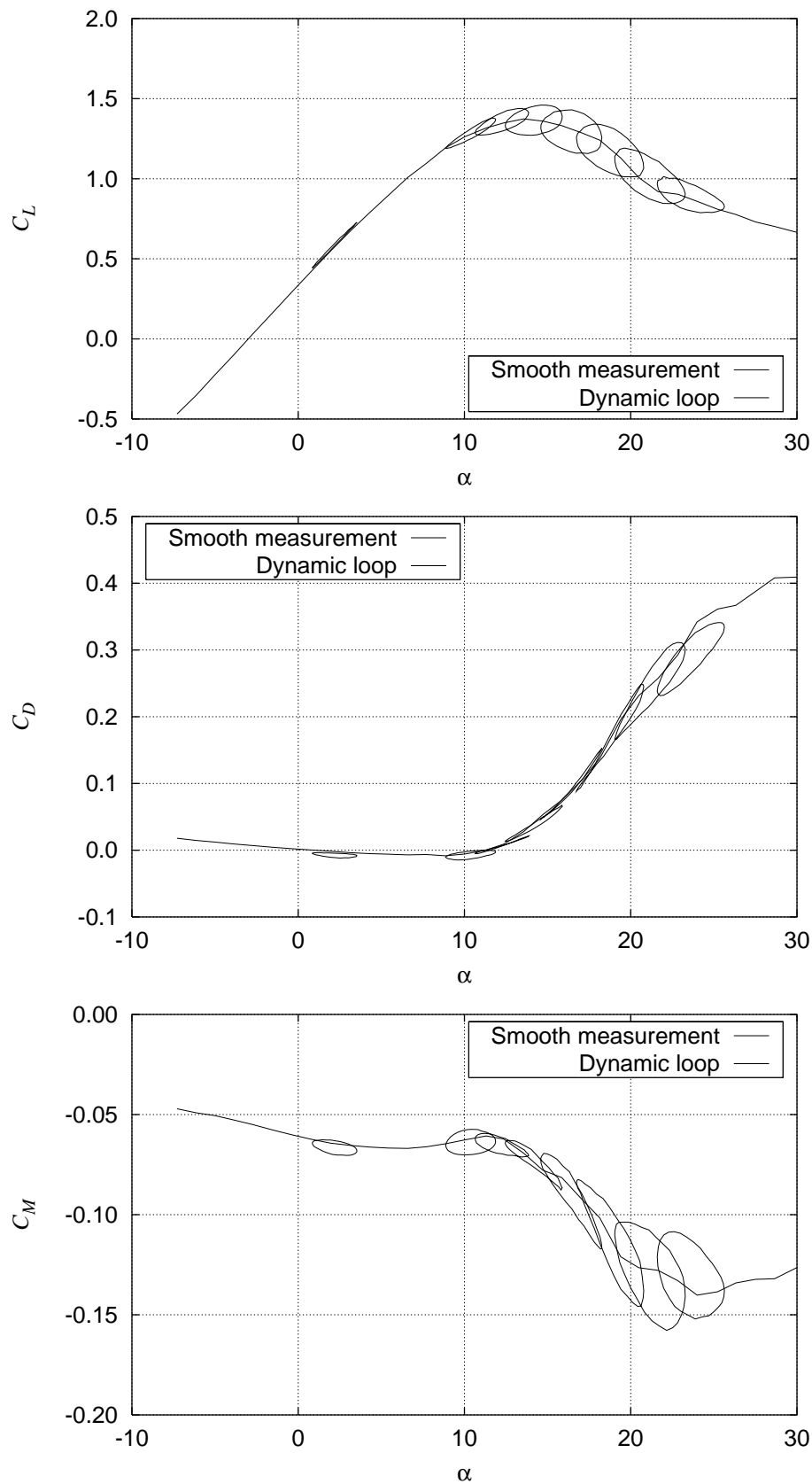
Figure 7-27 C_L, C_D and C_M hysteresis loops for NACA 63-415 smooth measurements at k = 0.092, A between 1.3° and 2.1° (run064)
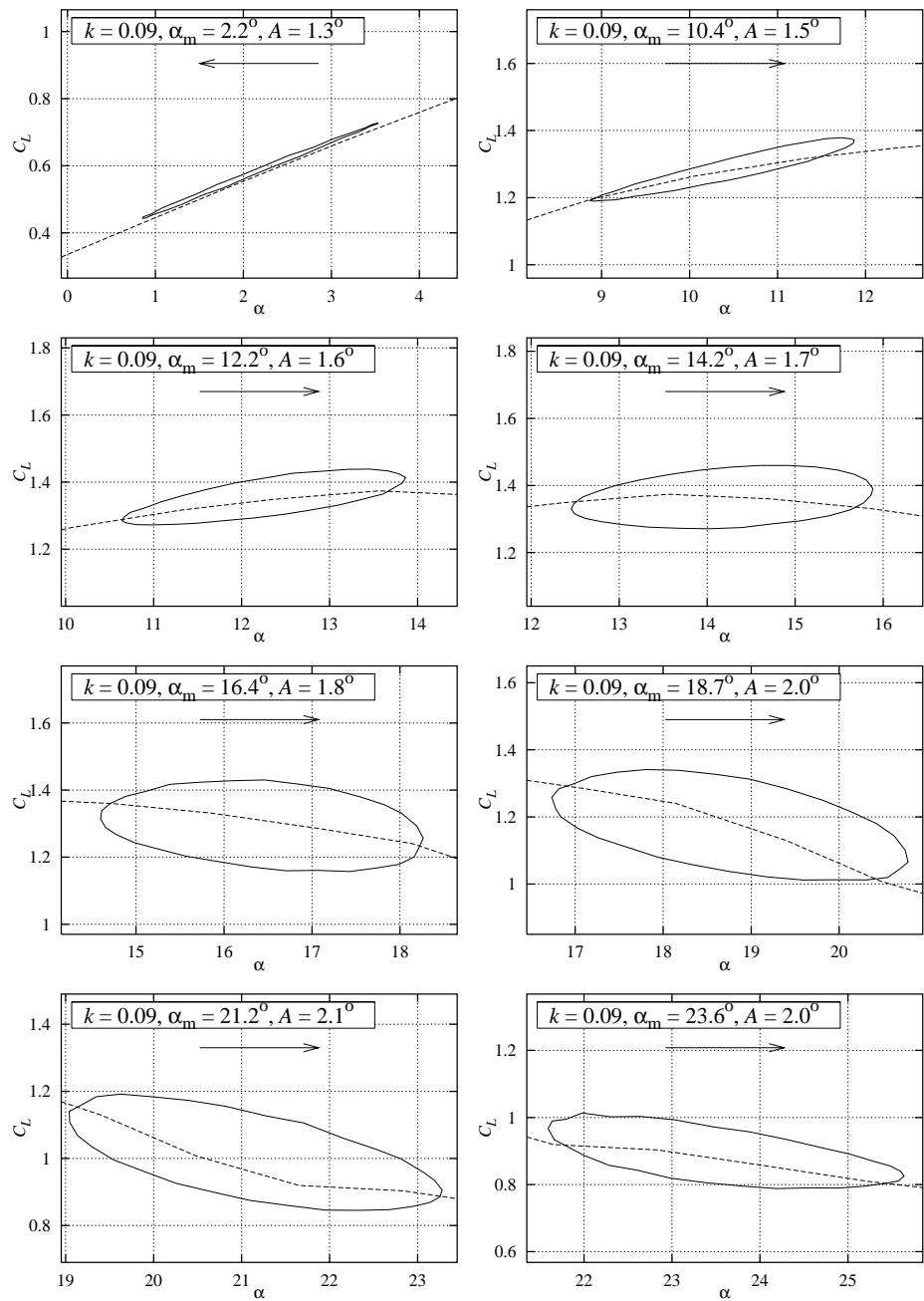
Figure 7-28 C_L hysteresis loops for NACA 63-415-Risø-D smooth measurements at k = 0.09, A between 1.3° and 2.1° (run006).
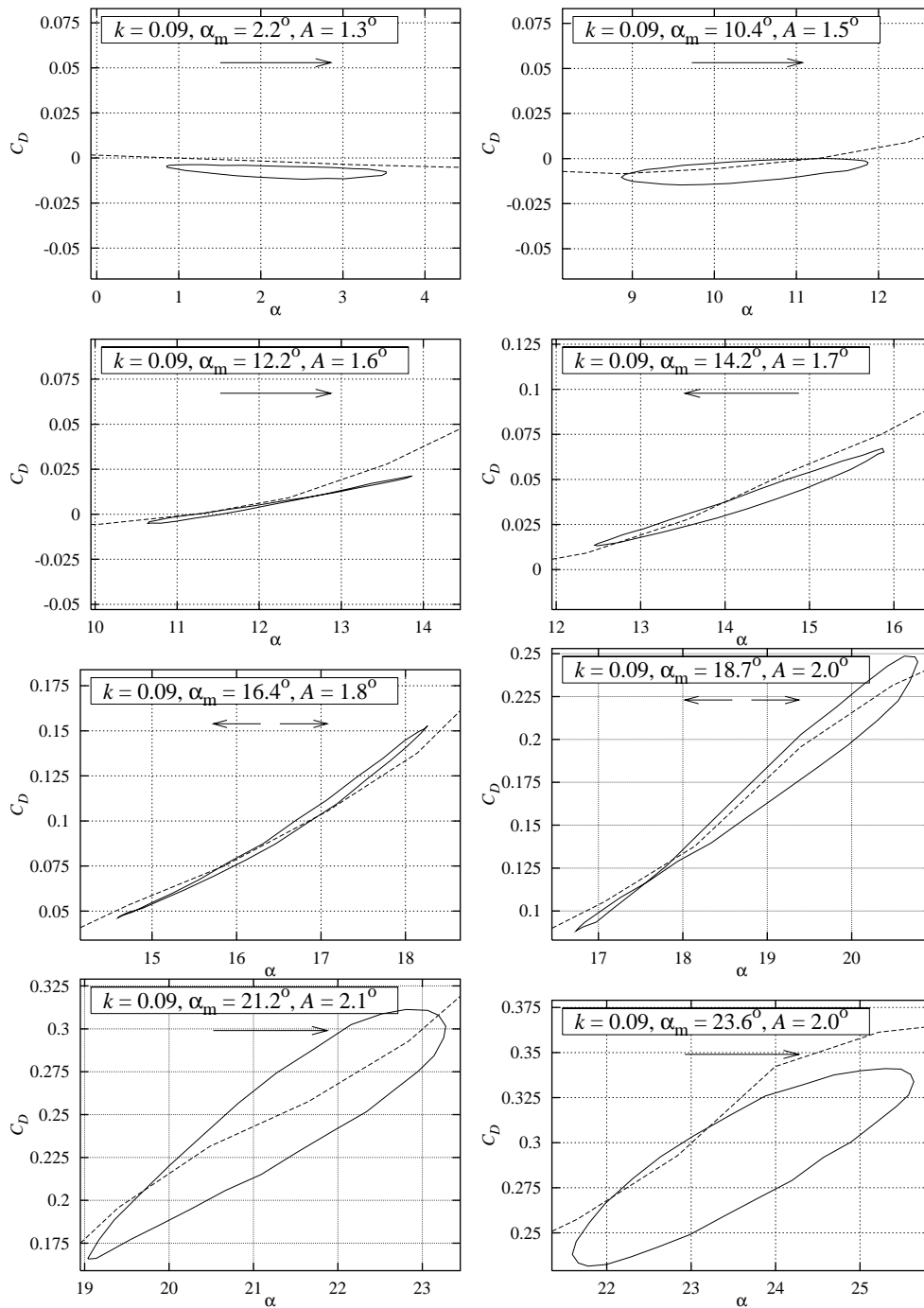
Figure 7-29 C_D hysteresis loops for NACA 63-415-Risø-D smooth measurements at k = 0.09, A between 1.3° and 2.1° (run006).
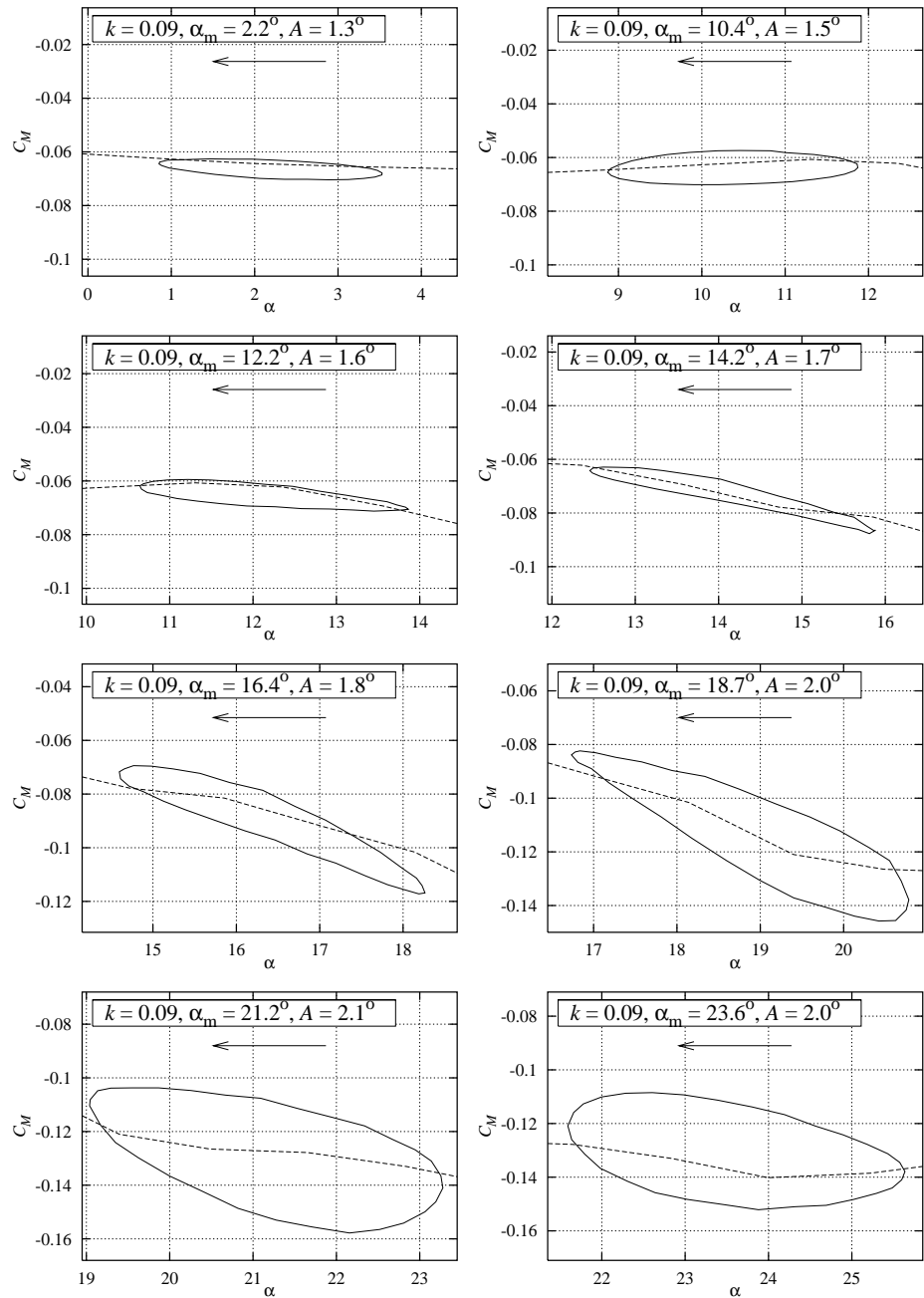
Figure 7-30 C_M hysteresis loops for NACA 63-415-Risø-D smooth measurements at k = 0.09, A between 1.3° and 2.1° (run006).

7.7 NACA 63-415-Risø-D, stall characteristics (run004, 007)
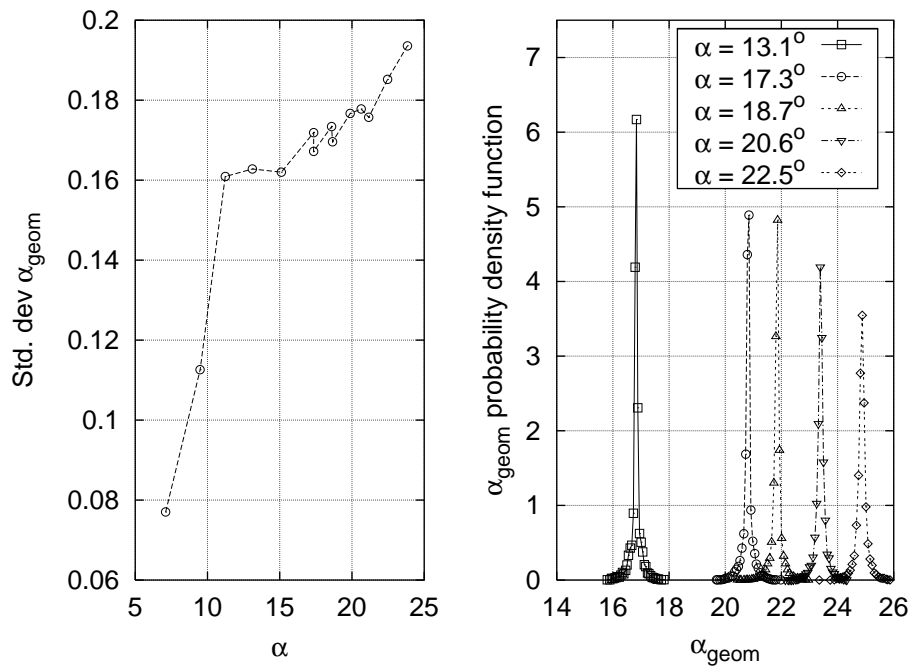
Figure 7-31 NACA 63-415-Risø-D smooth. Left: Standard deviation of geometrical α as function of mean α. Right: Probability density function of geometrical α at different mean α.
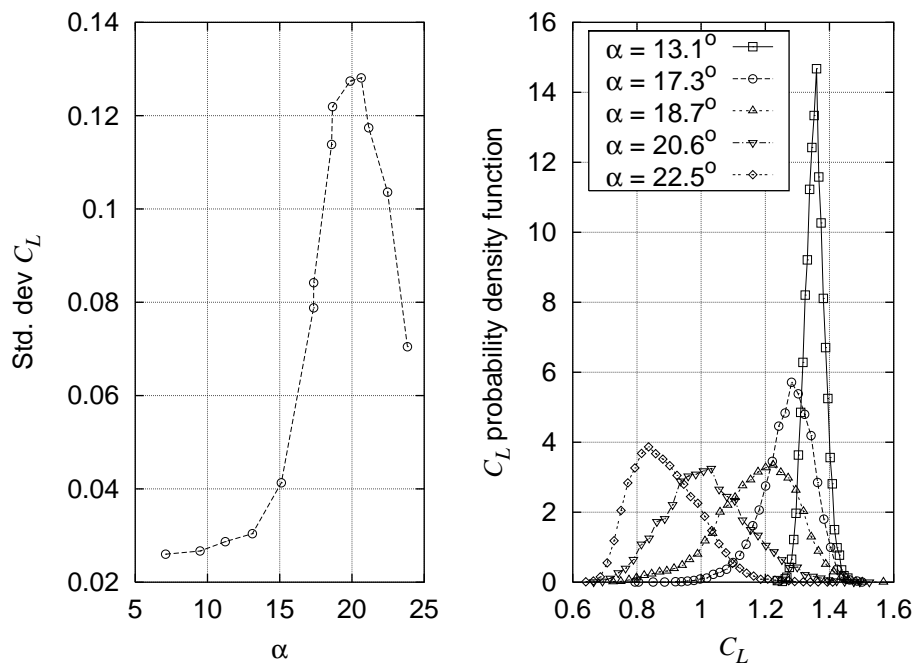
Figure 7-32 NACA 63-415-Risø-D smooth. Left: Standard deviation of C_L as function of mean α. Right: Probability density function of C_L at different mean α.
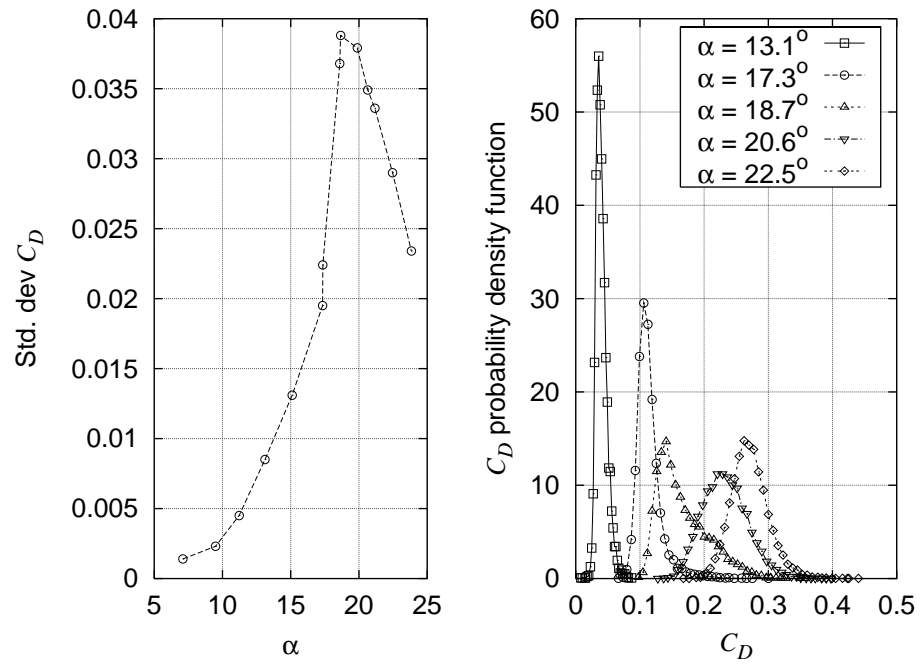
Figure 7-33 NACA 63-415-Risø-D smooth. Left: Standard deviation of C_D as function of mean α. Right: Probability density function of C_D at different mean α.
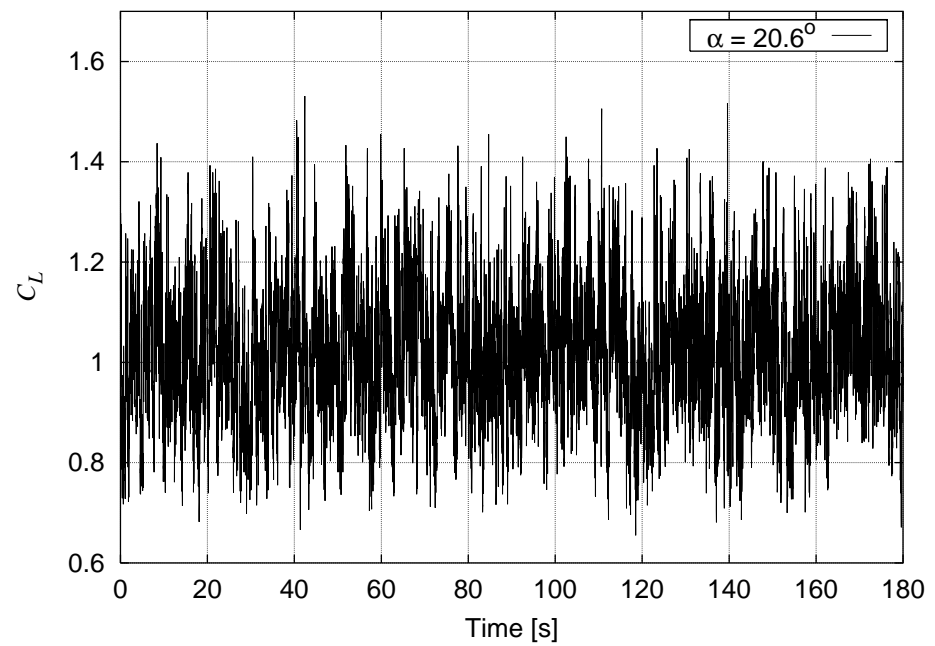
Figure 7-34 NACA 63-415-Risø-D smooth: Time series of C_L for mean α=20.6°.
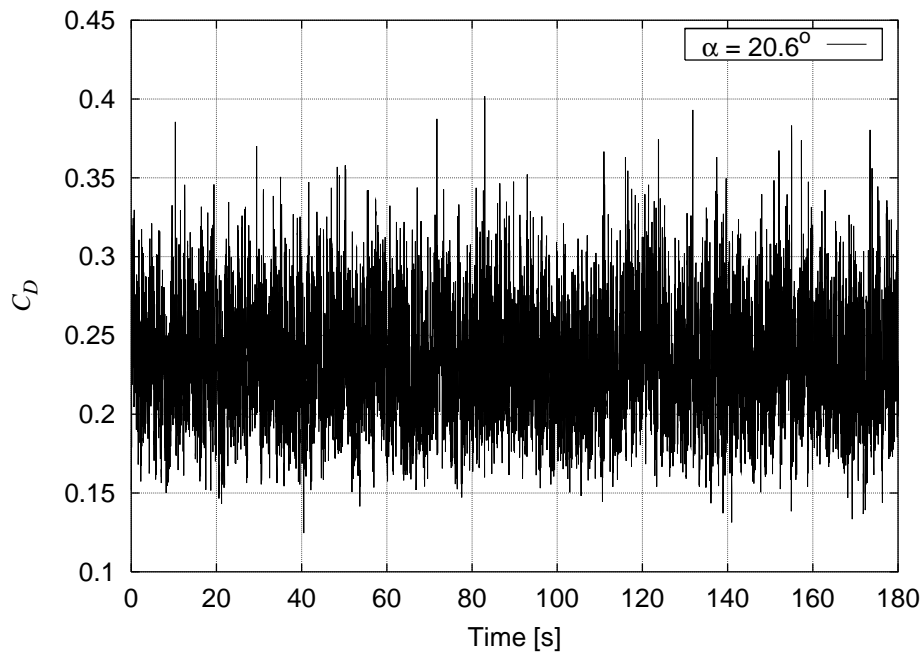
Figure 7-35 NACA 63-415-Risø-D smooth: Time series of C_D for mean α=20.6°.

8 Comparison

8.1 Smooth flow (run024, run002)
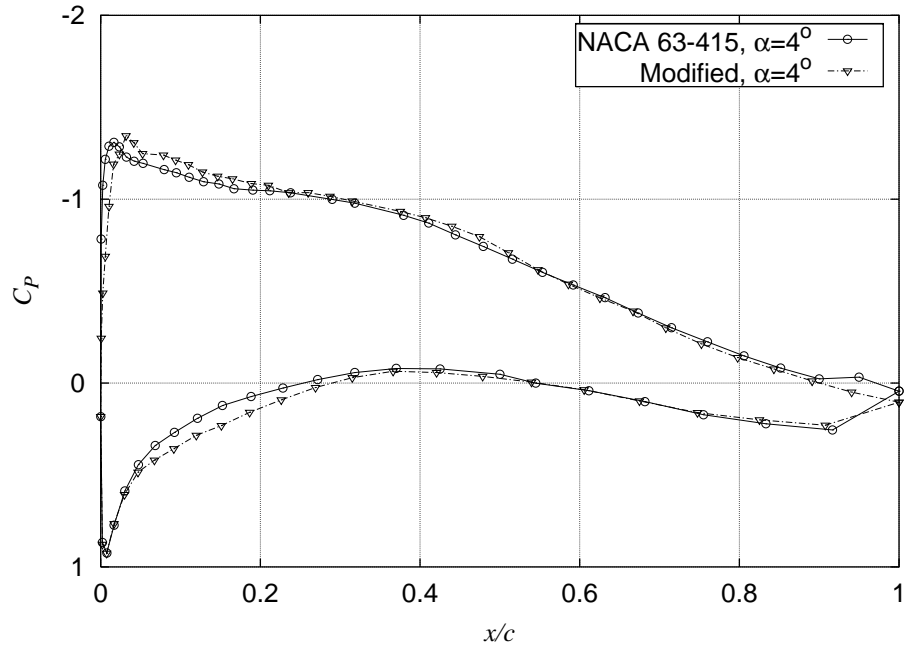
Figure 8-1 C_P at $\alpha = 4°$ for NACA 63-415 and NACA 63-415-Risø-D smooth measurements.
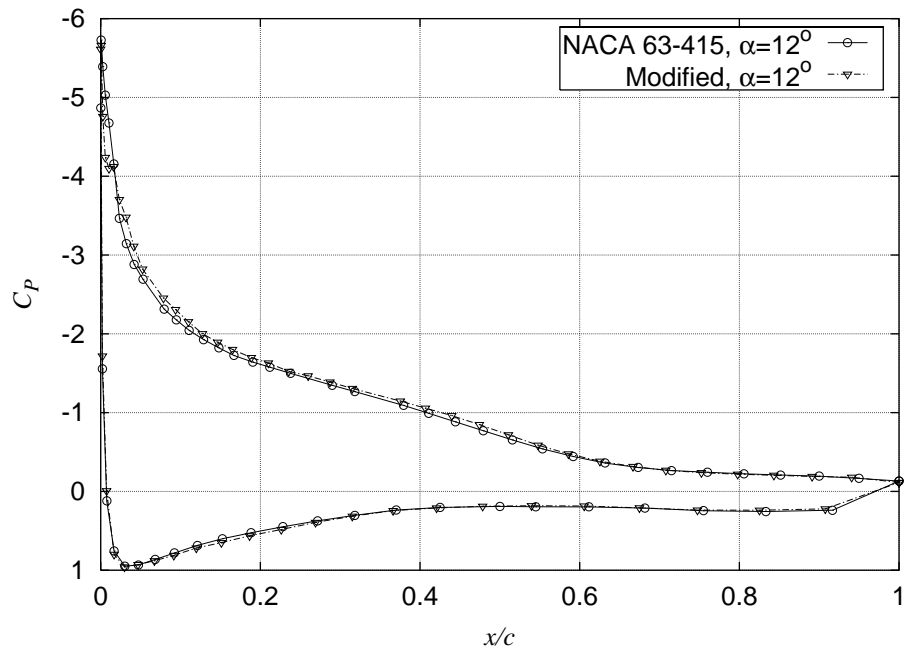
Figure 8-2 C_P at $\alpha = 12°$ for NACA 63-415 and NACA 63-415-Risø-D smooth measurements.
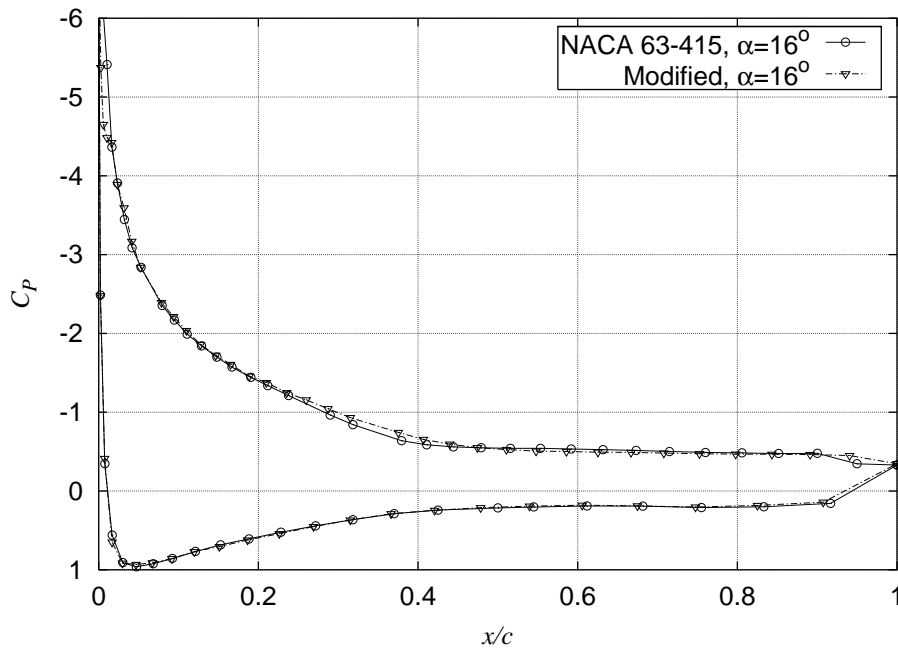
Figure 8-3 C_P at $\alpha = 16°$ for NACA 63-415 and NACA 63-415-Risø-D smooth measurements.
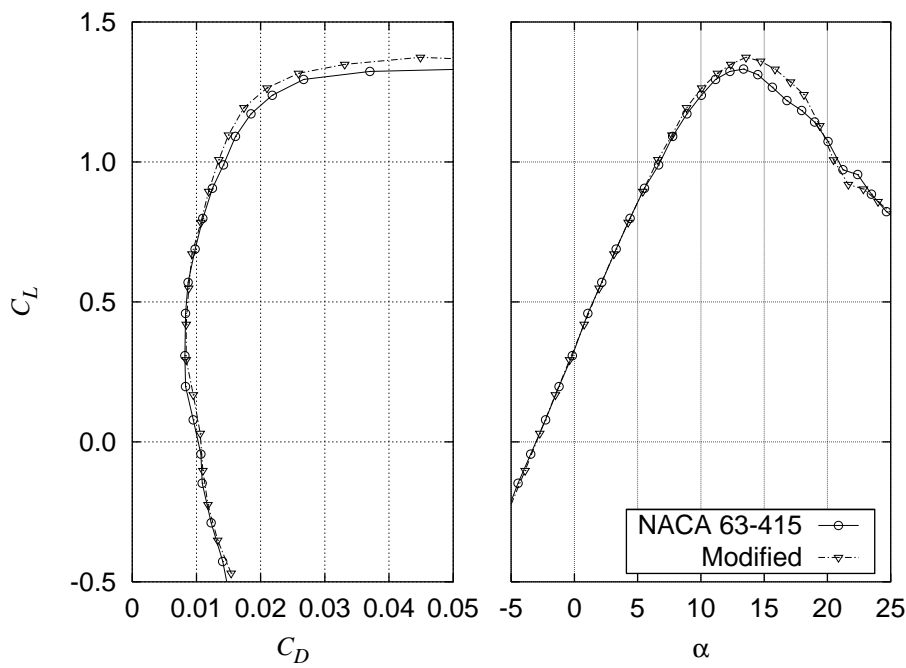
Figure 8-4 C_L-C_D for NACA 63-415 and NACA 63-415-Risø-D smooth measurements.
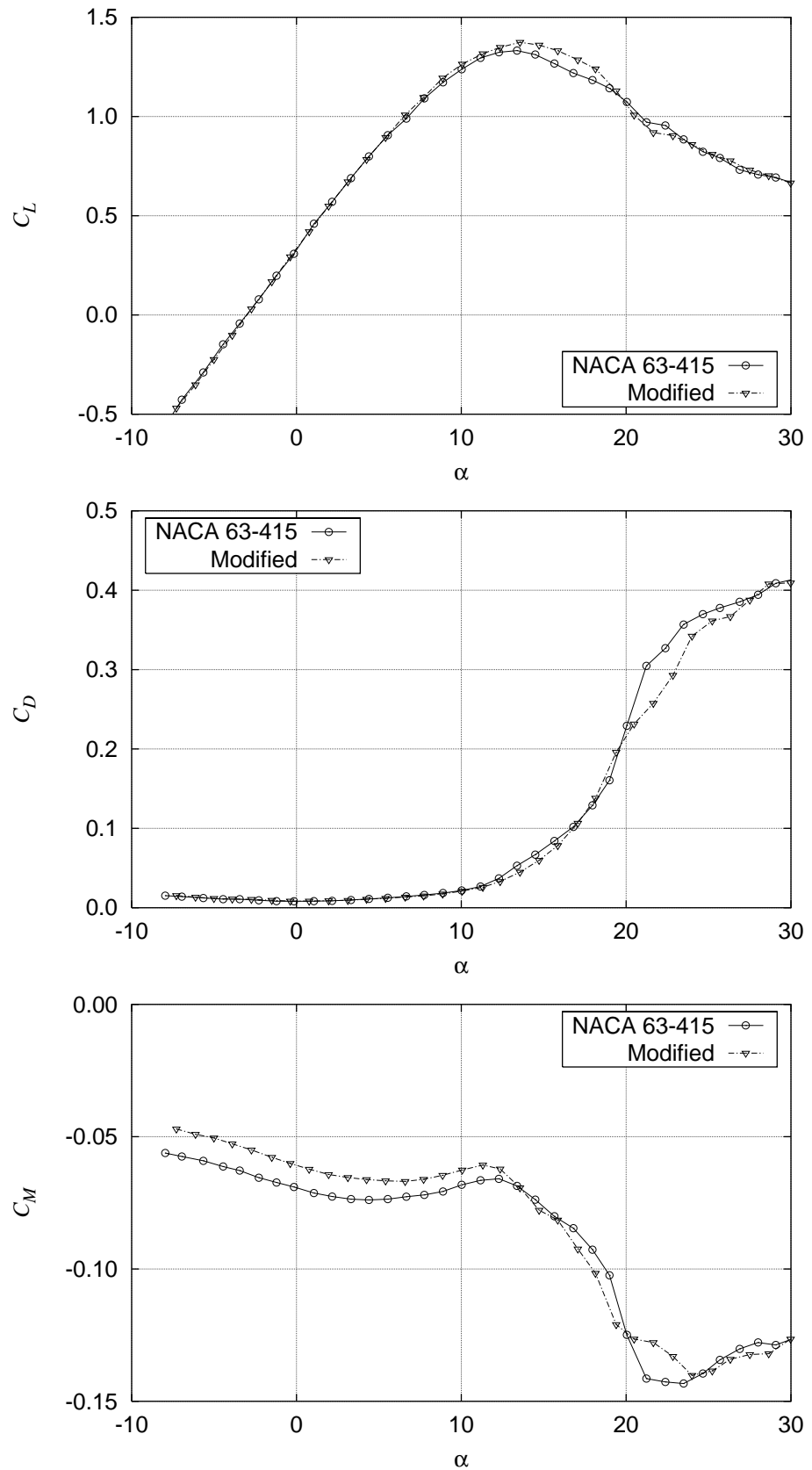
Figure 8-5 C_L, C_D and C_M for NACA 63-415 and NACA 63-415-Risø-D smooth measurements.
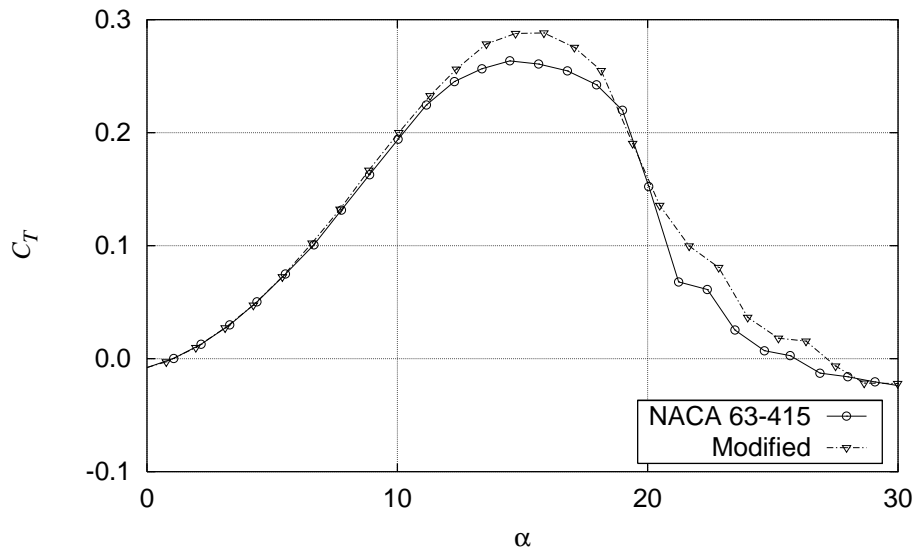
Figure 8-6 C_T for NACA 63-415 and NACA 63-415-Risø-D smooth measurements.
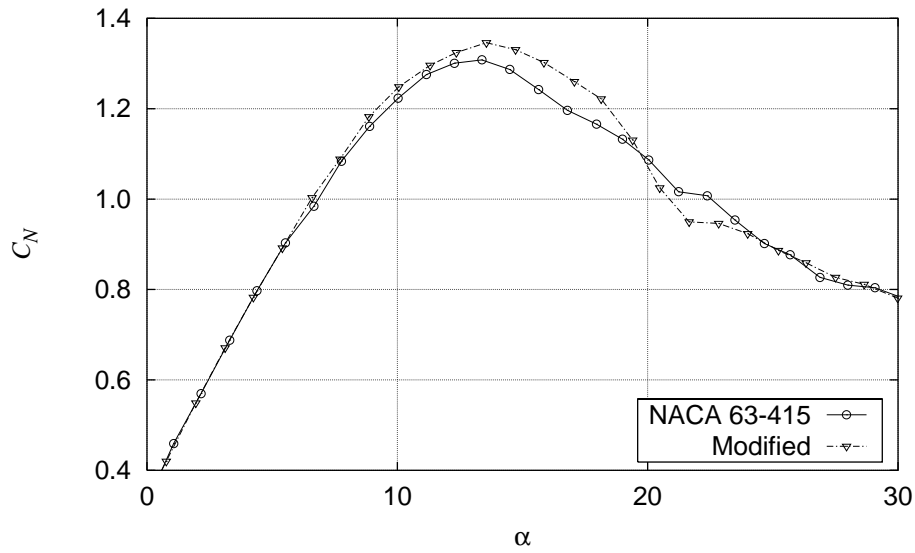
Figure 8-7 C_N for NACA 63-415 and NACA 63-415-Risø-D smooth measurements.

8.2 Leading edge roughness

8.2.1 LER zigzag-tape 90° at 0.05/0.10
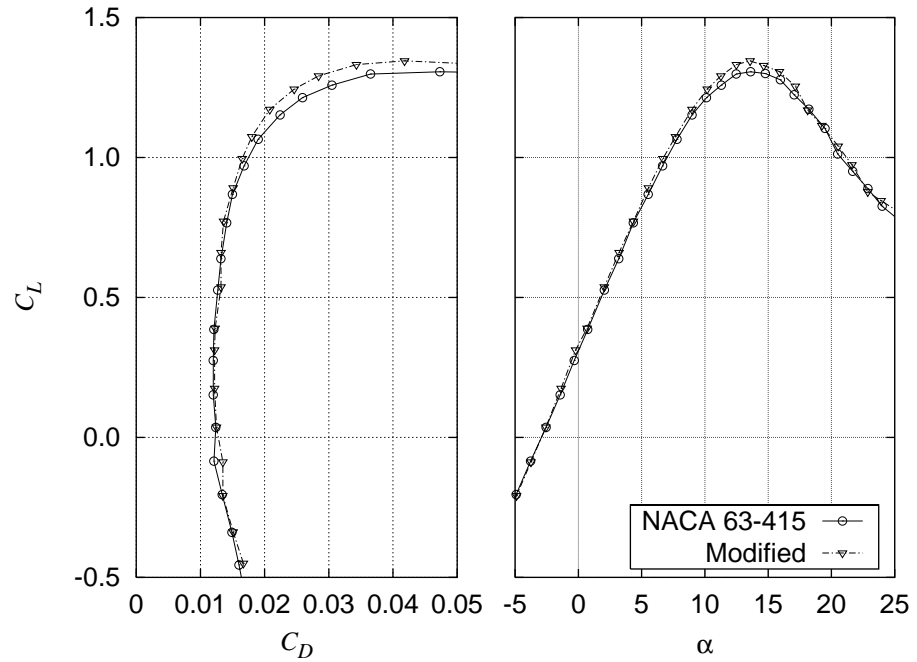
Figure 8-8 C_L-C_D for NACA 63-415 and NACA 63-415-Risø-D LER zigzag 90°, 0.35mm at 0.05/0.10.
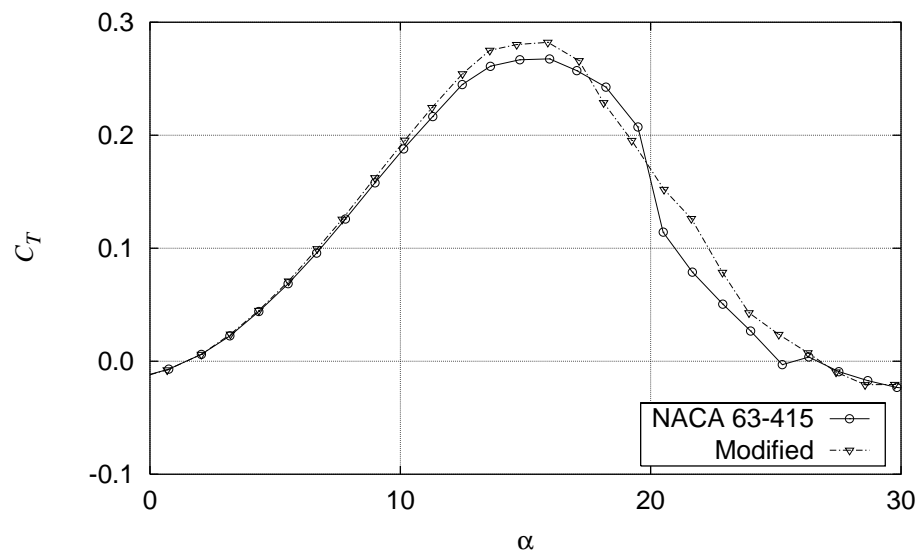
Figure 8-9 C_T for NACA 63-415 and NACA 63-415-Risø-D LER zigzag 90°, 0.35mm at 0.05/ 0.10.

8.2.2 LER zigzag tape 90° at leading edge suction side
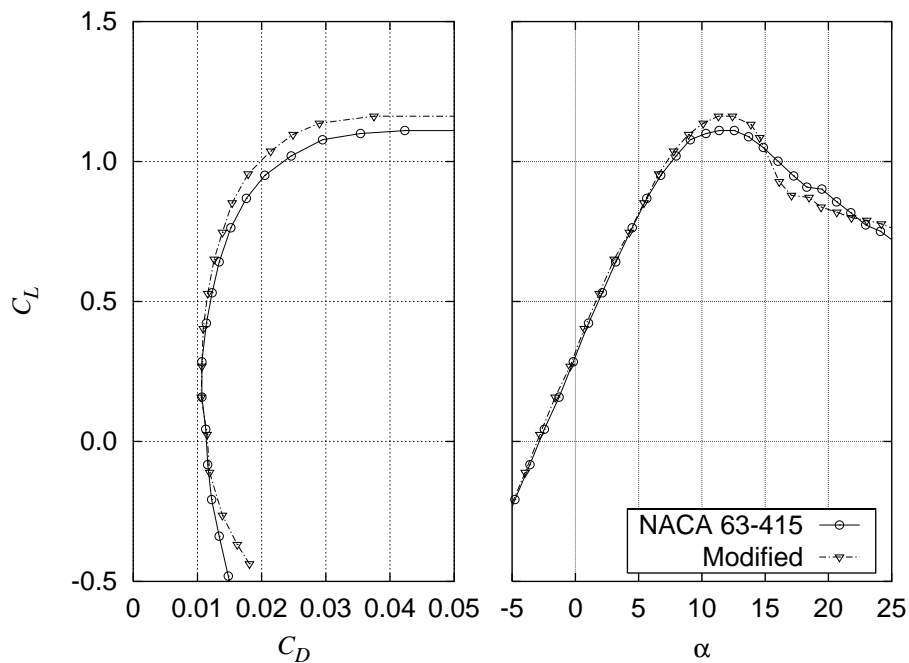
Figure 8-10 C_L-C_D for NACA 63-415 and NACA 63-415-Risø-D LER zigzag 90°, 0.35mm at LE s.s.
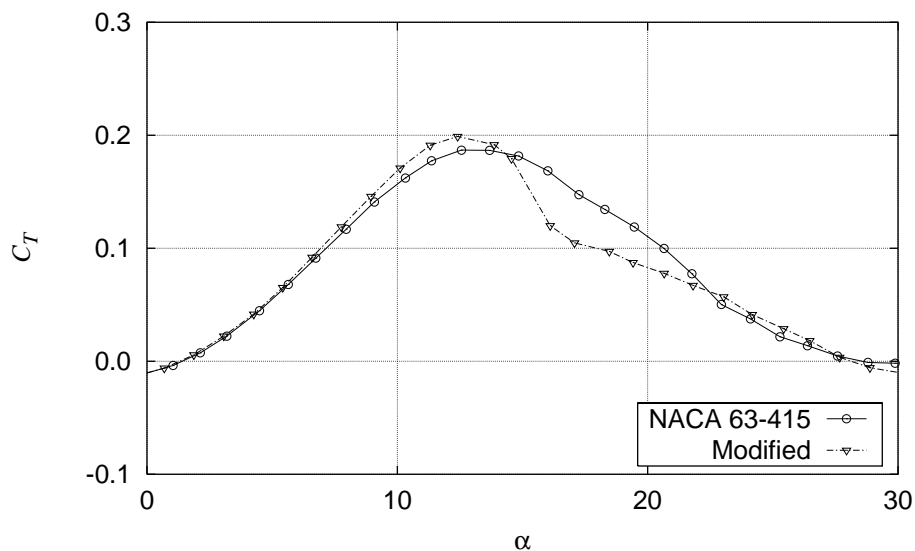
Figure 8-11 C_T for NACA 63-415 and NACA 63-415-Risø-D LER zigzag 90°, 0.35mm at LE s.s.

8.2.3   LER zigzag tape 90° at leading edge pressure side
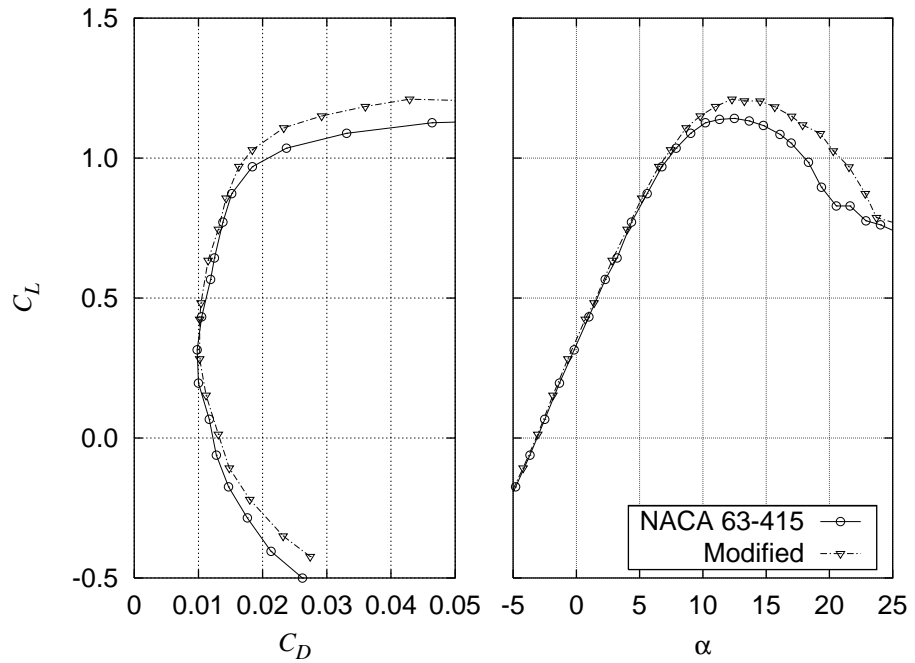
Figure 8-12 C_L-C_D for NACA 63-415 and NACA 63-415-Risø-D LER zigzag 90°, 0.35mm at LE p.s.
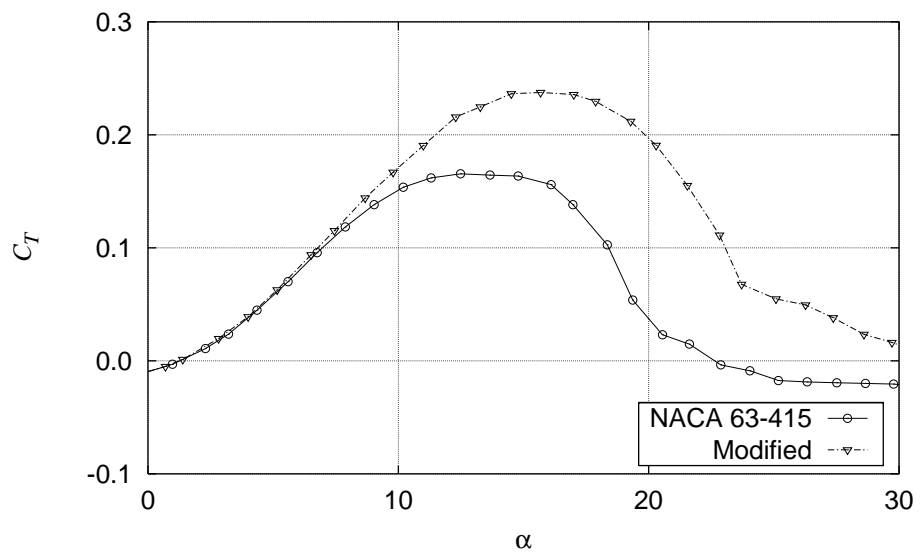
Figure 8-13 C_T for NACA 63-415 and NACA 63-415-Risø-D LER zigzag 90°, 0.35mm at LE p.s.

8.2.4 LER trip tape and zigzag tape 60° at leading edge pressure side
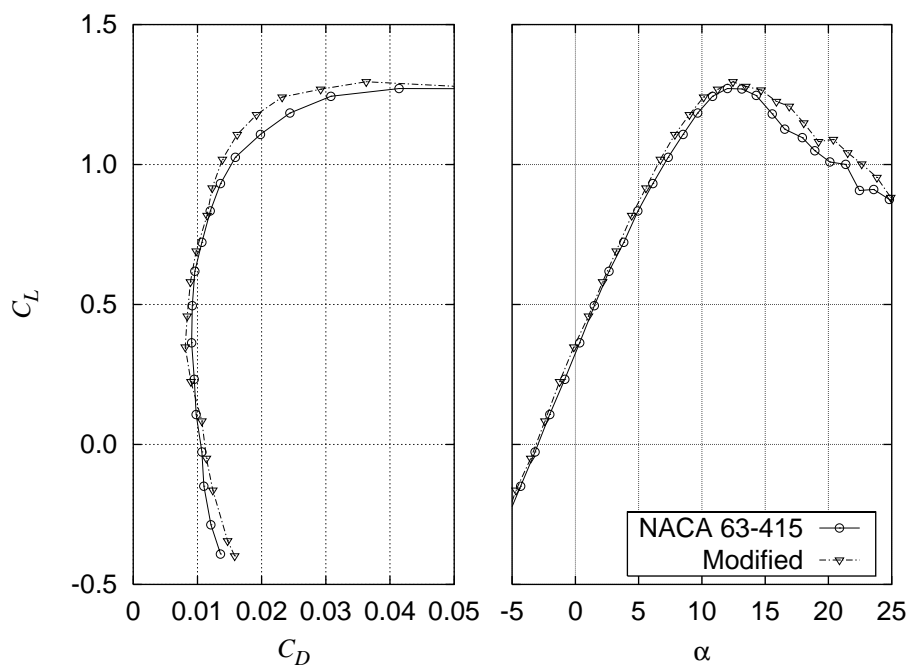
Figure 8-14 C_L-C_D for NACA 63-415 and NACA 63-415-Risø-D LER trip tape at LE p.s.
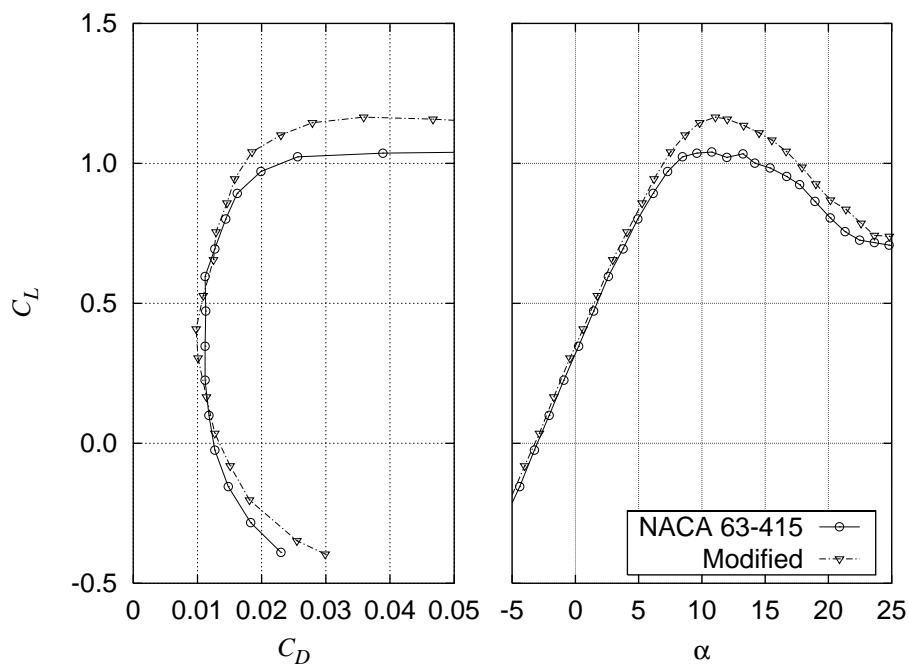
Figure 8-15 C_L-C_D for NACA 63-415 and NACA 63-415-Risø-D LER zigzag 60°, 0.85mm at LE p.s.

8.3 Dynamic stall
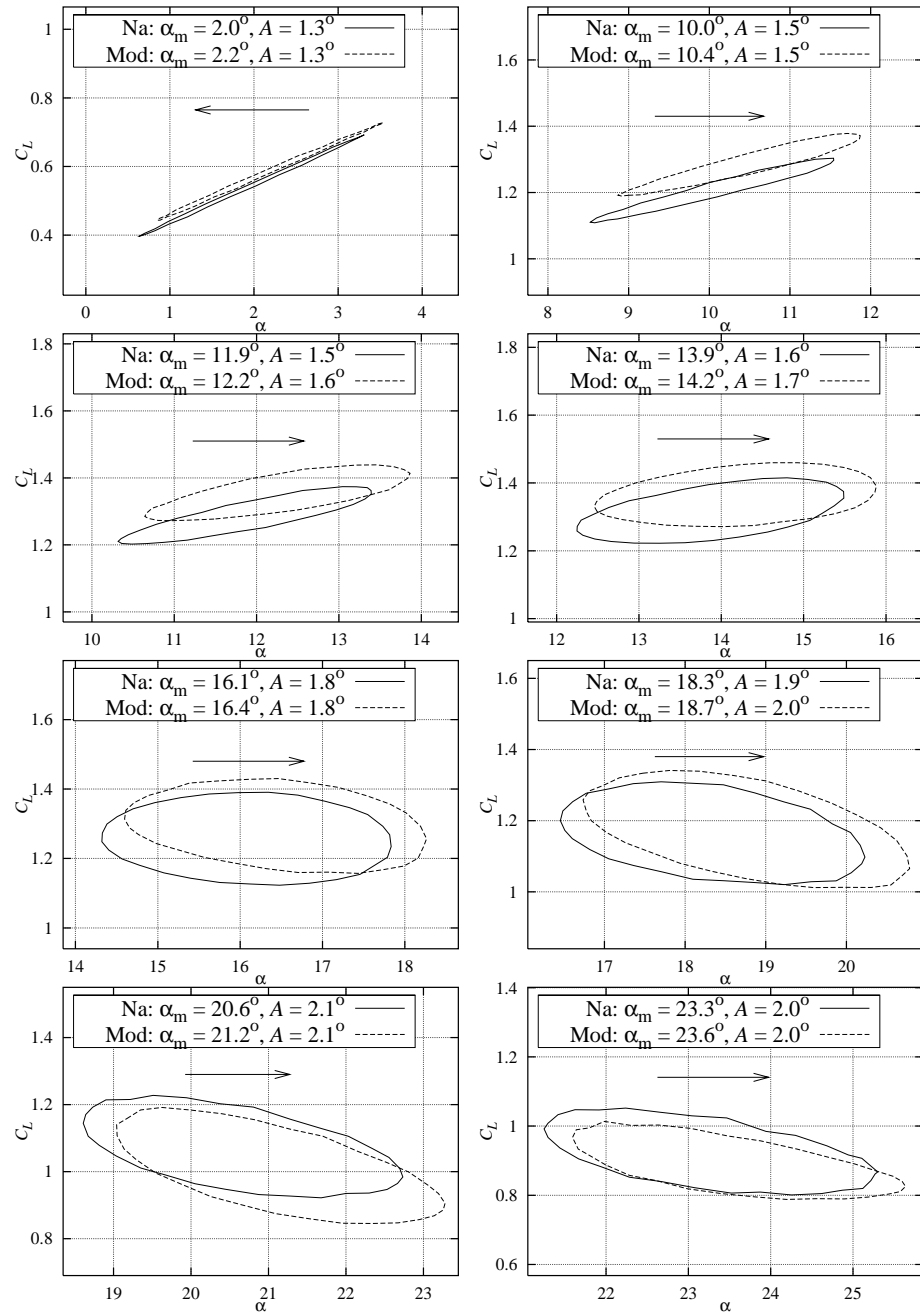
Figure 8-16 C_L hysteresis loops for NACA 63-415 and NACA 63-415-Risø-D smooth measurements at k = 0.09, A between 1.3° and 2.1°. **Na** *and* **Mod** *denotes NACA 63-415 and NACA 63-415-Risø-D, respectively.*
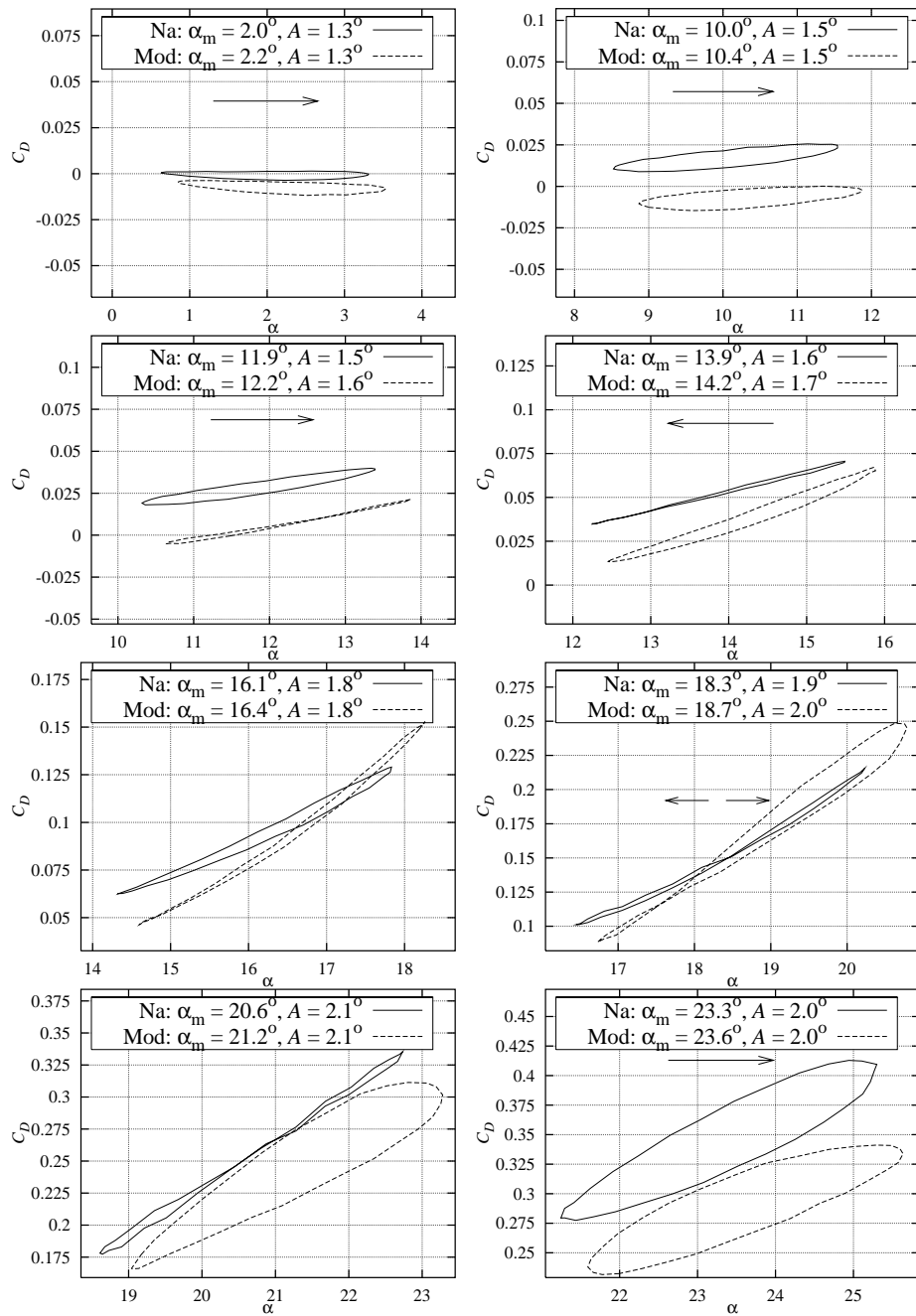
*Figure 8-17 C_D hysteresis loops for NACA 63-415 and NACA 63-415-Risø-D smooth measurements at k = 0.09, A between 1.3° and 2.1°. **Na** and **Mod** denotes NACA 63-415 and NACA 63-415-Risø-D, respectively. If no arrow is present in the plot the directions for the two loops are different.*
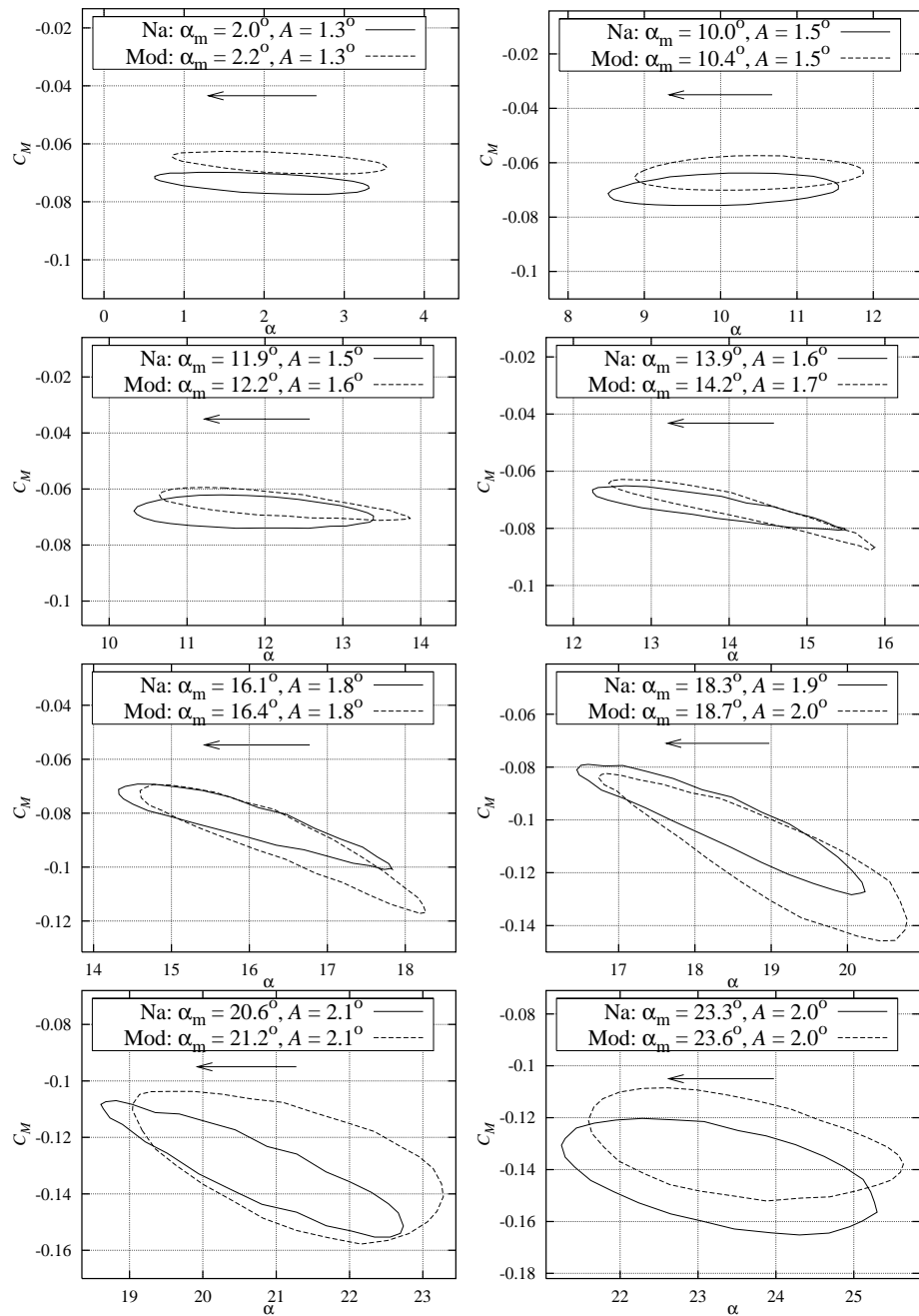
*Figure 8-18 C_M hysteresis loops for NACA 63-415 and NACA 63-415-Risø-D smooth measurements at k = 0.09, A between 1.3° and 2.1°. **Na** and **Mod** denotes NACA 63-415 and NACA 63-415-Risø-D, respectively.*

8.4 Stall characteristics
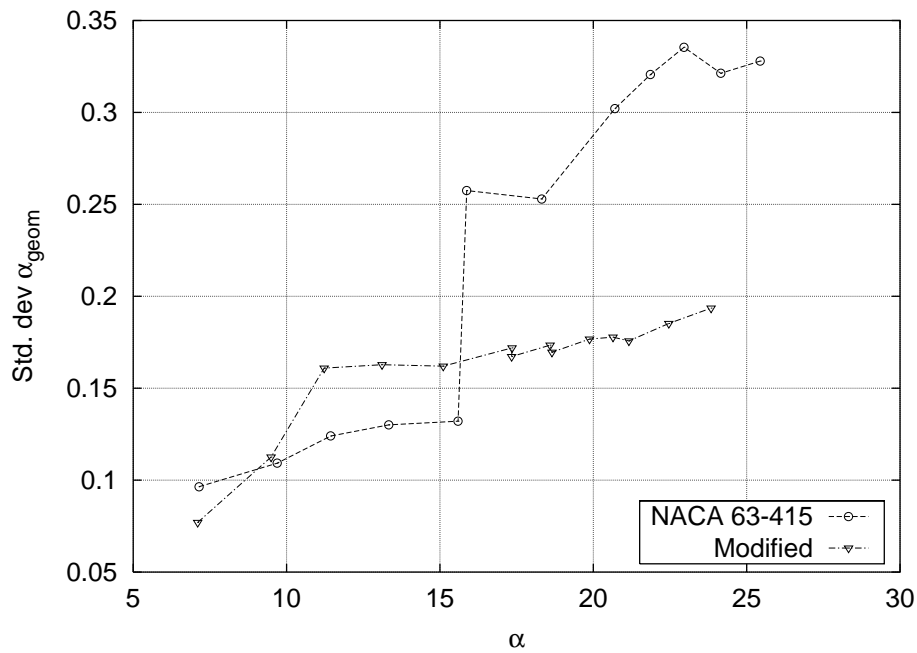
Figure 8-19 Standard deviation of geometrical α as function of mean α. NACA 63-415 and NACA 63-415-Risø-D smooth.
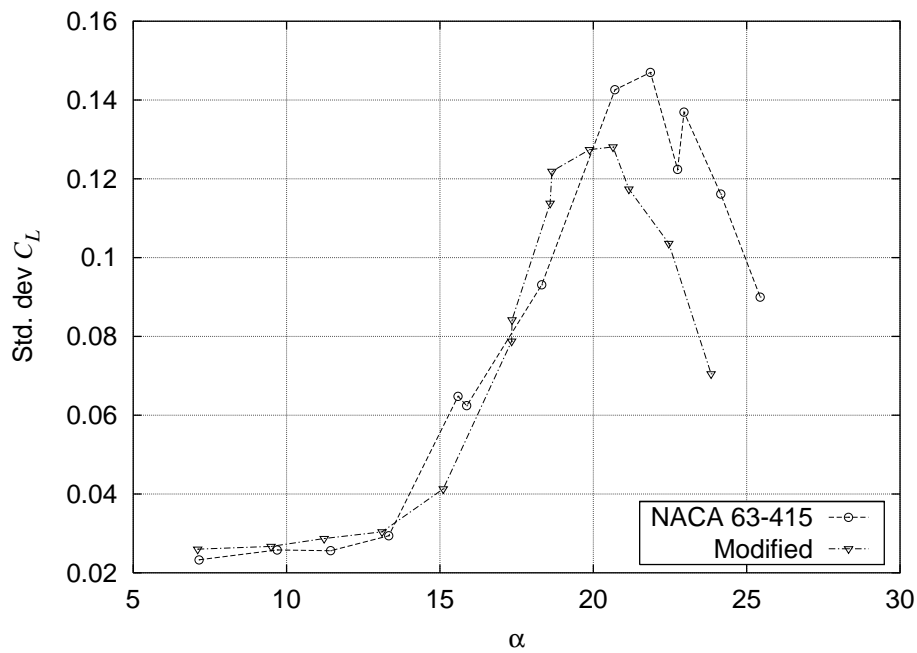
Figure 8-20 Standard deviation of C_L as function of mean α. NACA 63-415 and NACA 63-415-Risø-D smooth
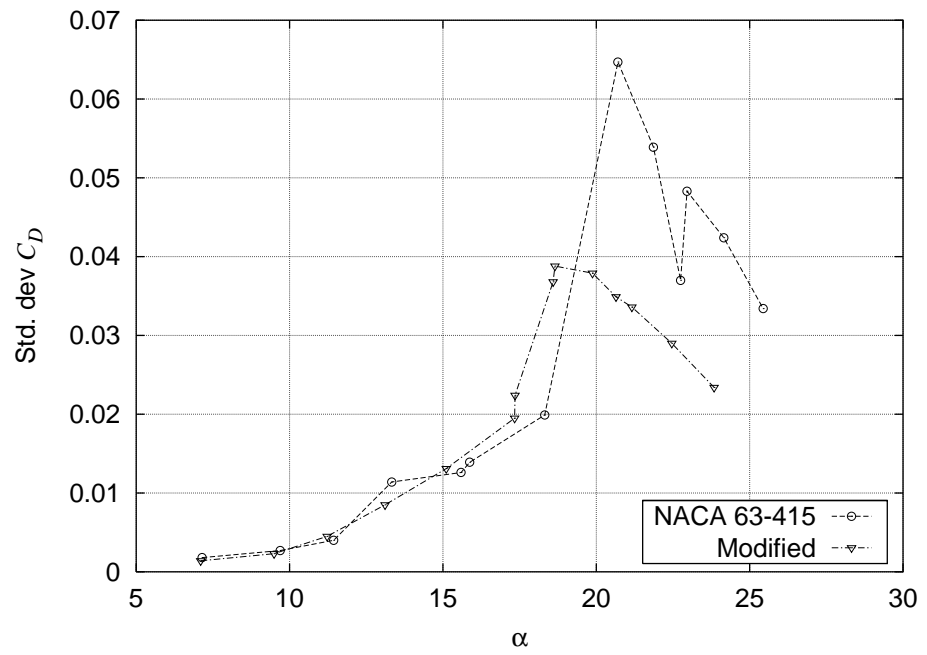
Figure 8-21 Standard deviation of C_D as function of mean α. NACA 63-415 and NACA 63-415-Risø-D smooth

9 Discussion

9.1 NACA 63-415

Measurements of NACA 63-415 are shown in Chapter 6, and main results are shown in Table 9-1.

Table 9-1 C_{Lmax} and C_{Dmin} for NACA 63-415.

		Run	C_{Lmax}	C_{Dmin}
Smooth		024	1.33	0.008
LER	ZZ90^o 0.05/0.10	025	1.31	0.012
	ZZ90^o s.s.	027	1.11	0.011
	ZZ90^o p.s.	028	1.14	0.010
	ZZ60^o p.s.	094	1.04	0.011
	TT p.s.	092	1.27	0.009
SS	7mm, P0,-2	093	1.00	0.011
	7mm, P0,0	085	1.05	0.010
	7mm, P0,2	086	1.03	0.011
	5mm, P0,6	087	1.25	0.011
	5mm, P0,10	089	1.30	0.011
	5mm, P0.14	088	1.31	0.013
VG	Smooth	072	1.74	0.017

Results of the measurements with smooth surface conditions are shown in Section 6.1 together with computations using the Navier-Stokes solver, EllipSys2D. The slope of the measured C_L, Figure 6-6, remains fairly constant until about $\alpha = 9°$ where separation is initiated. C_{Lmax} of about 1.33 is reached at $\alpha = 13^o$. In the post stall area C_L is reduced smoothly until about $\alpha = 20°$ indicating that separation occurs from the trailing edge and progressively approaches the leading edge. At about $\alpha = 20°$ double stall is observed, i.e. sudden shifts between trailing-edge and leading-edge stall, as shown in Section 6.8. Above $\alpha = 20°$ most of the suction side is separated and deep stall takes place as shown in Figure 6-1. The measurement of C_D shows a C_{Dmin} of around 0.008. At $\alpha = 20°$ the slope of C_D is steep indicating a shift from trailing-edge stall to leading-edge stall.

The measurements compare well with computations for low α, Figure 6-5. For a>5° C_L is calculated slightly higher than measured. This is due to the turbulence model in the CFD code. Figure 6-2 to Figure 6-4 show the measured and computed C_p distributions for $\alpha = 4°$, 12° and 16°. At $\alpha = 4°$ good agreement between computations and measurements is obtained. Only a slight deviation is observed at the trailing edge, which is caused by an improper resolution of pressure tabs and an irregular response from one of the pressure tabs due to manufacturing difficulties. At $\alpha = 12°$ the computations slightly over estimate C_L because separation is delayed compared to the measurements. No particular difference is seen between turbulent and transitional computations except at around $x/c = 0.03$ on the suction side, where transition

from laminar to turbulent flow is calculated to take place. At $\alpha = 16°$ the transitional computation does predict a larger separation compared to the turbulent computation. This is due to the existence of a laminar separation bubble at the leading edge. The measured and the predicted $C_{D,min}$, Figure 6-5, and the shape of the C_D curve at low angles of attack are both in fairly good agreement. The transitional computations result in lower drag, which is due to the lower skin friction from the laminar part of the boundary layer.

Measurements with Leading Edge Roughness (LER) using 90° zigzag tape at different positions are shown in Section 6.2. Three configurations are investigated: Roughness at x/c = 0.05 on the suction side and 0.10 on the pressure side (0.05/0.10), roughness at the suction side (s.s.) of the leading edge and roughness at the pressure side (p.s.) of the leading edge.

Pressure distributions are shown at $\alpha = 4°$, 12° and 16° for the three different LER configurations compared with smooth measurements in Figure 6-7 to Figure 6-9. At $\alpha = 4°$, placing the tape at the suction side results in a large local suction peak, which is probably caused by the increased acceleration of the flow due to the tape thickness. For all angles of attack LER at 0.05/010 does not have much influence since laminar separation occurs upstream of $x/c = 0.05$ and because the suction peak is located upstream of $x/c = 0.05$ at $\alpha > 6°$. In Figure 6-9 it is seen that LER at 0.05/010 results in higher suction pressure at $\alpha = 16°$ and thereby in higher C_L and lower C_D than for a smooth airfoil. As seen in C_L and C_D, Figure 6-10, the LER at the very leading edge significantly affects the flow above $\alpha = 8°$ decreasing C_L. Mounting the LER from the very leading edge towards the pressure side results in a large decrease of C_L and increase of C_D. However, the changes of C_L and C_D are even larger if the LER is mounted from the very leading edge towards the suction side.

In Section 6.3 different LER types at the pressure side of the leading edge are compared: 90° zigzag tape, 60° zigzag tape and trip tape with height 0.35 mm, 0.85 mm and 0.12 mm, respectively. Both pressure distributions, Figure 6-12 to Figure 6-14, and C_L and C_D, Figure 6-15 and Figure 6-16, show that higher roughness elements result in lower C_L and higher C_D. Thus, 60° zigzag tape has the most severe effect with $C_{L,max} = 1.04$ and $C_{D,min} = 0.011$, while trip tape has the smallest effect with $C_{L,max} = 1.27$ and $C_{D,min} = 0.009$.

In Section 6.4 measurements with Vortex Generators (VG's) are shown. Pressure distributions at $\alpha = 4°$, 12° and 16° are shown in Figure 6-17 to Figure 6-19. At $\alpha = 4°$ the difference in pressure between the smooth airfoil and the airfoil mounted with VG's is only seen at the very vicinity of the VG's where a decrease in the suction pressure is observed. At $\alpha = 12°$ the difference in pressure with and without VG's is seen from the VG's towards the trailing edge indicating that no separation is present when using VG's. This means that stall is delayed. At $\alpha = 16°$ the difference in pressure with and without VG's is significant showing no separation when using VG's and a separated area from x/c = 0.4 to the trailing edge without VG's. From the polars Figure 6-20 and Figure 6-21 it can be seen that C_L is increased with VG's for $\alpha > 8°$. $C_{L,max}$ is obtained at $\alpha = 13°$ without VG's, but at $\alpha = 18°$ with VG's. Thus, the C_L-α curve indicates that only slight separation occurs until $C_{L,max}$. Above $C_{L,max}$ an abrupt loss of C_L and increase of C_D is seen indicating a sudden shift from trailing-edge stall to leading-edge stall. At $\alpha = 20°$ C_L with and without VG's is similar. For α up to 12° the VG's results in higher C_D increasing $C_{D,min}$ from 0.008 without VG's to 0.017 with VG's.

Measurements with Stall Strips (SS) mounted on the airfoil section are shown in Sections 6.5 and 6.6. Two different SS are placed at six different locations. Measurements with SS are compared to measurements on a smooth airfoil. Placing the SS close to the leading edge significantly lowers C_{Lmax} and the slope of the C_L curve, Figure 6-25. Large differences in the characteristics are seen for SS mounted around $x/c = 0.002$ at the suction side (P0,-2) and the pressure side (P0,2), respectively. Mounting the SS at the suction side position reduces C_L, especially in deep stall, and increases C_D, from $\alpha > 0°$ compared to the position at the pressure side where C_L in deep stall drops less. Furthermore, for $\alpha < 0°$ the increase of C_D is small if the SS is mounted on the suction side, but significant if it is mounted on the leading edge or on the pressure side. From the pressure distributions, Figure 6-22 to Figure 6-24, it can be seen that the different positions of the SS result in very different pressure distributions. With the SS mounted on the leading edge suction side no suction peak can be observed in either of the three pressure distributions. However, a suction peak is present at $\alpha = 12°$ if the SS is mounted at the very leading edge. If the SS is mounted at the leading edge pressure side a suction peak is present even at $\alpha = 16°$. From the pressure distributions and polars it can be seen that the position of the SS at the very leading edge is very important for the resulting airfoil characteristics. Moving the SS downstream on the pressure side the lift-drag polars will approach the smooth curve, Figure 6-30. Mounting the SS at $x/c = 0.01$ at the pressure side will affect the airfoil characteristics resulting in slightly lower C_L and higher C_D compared to a smooth airfoil. If the SS is mounted at $x/c = 0.026$ and 0.041 pressure side the airfoil characteristics only change marginally compared to a smooth airfoil. For $\alpha < 2°$ significant increase of C_D is observed for all positions on the pressure side.

Section 6.7 describes dynamic stall measurements. For angles of attack below $C_{L,max}$, Figure 6-32, the hysteresis loops are seen to be small while the loops are significantly open above $C_{L,max}$. Just at and above $C_{L,max}$ the slopes of the loops is positive while the slope of the polar is zero or negative. However, in deep stall the slopes of loops and the polar are comparable. It should be noted that there is an offset for some of the loops compared to the mean polar. This is due to the pressure calibration causing uncertainty in mean α. Figure 6-33 to Figure 6-35 show the hysteresis loops in detail for C_L, C_D and C_M, respectively. The arrows in the figures show the directions of the loops. Clockwise loops are illustrated by right arrows and anti-clockwise loops by left arrows.

Section 6.8 describes the stall characteristics measurements. Standard deviations for geometrical α, C_L and C_D as function of α, Figure 6-36 to Figure 6-38 left side, show that the standard deviation increases significantly around $\alpha = 15°$. It is also seen that the standard deviation of C_L and C_D has a maximum around $\alpha = 21°$. This coincides with the observation of double stall. Selected probability density functions of geometrical α, C_L and C_D, Figure 6-36 to Figure 6-38 right side, illustrate how the measured values are distributed. It is seen how the distribution for both α, C_L and C_D become lower and wider until $\alpha = 21°$, indicating that the flow becomes more fluctuating for increasing α. The probability density function of C_D at $\alpha = 20.7°$ indicates double stall since two peaks are observed. Time series of C_D, Figure 6-40, show that double stall is present. The appearance of double stall is not clear in the time series for C_L, Figure 6-39, but is seen as larger standard deviations when C_D is on its high level.

9.2 NACA 63-415-Risø-D

Measurements of NACA 63-415-Risø-D are shown in Chapter 7 and main results are shown in Table 9-2.

Table 9-2 C_{Lmax} and C_{Dmin} for NACA 63-415-Risø-D

		Run	C_{Lmax}	C_{Dmin}
Smooth		002	1.37	0.008
LER	ZZ90° 0.05/0.10	008	1.35	0.012
	ZZ90° s.s.	009	1.16	0.011
	ZZ90° p.s.	010	1.21	0.010
	ZZ60° p.s.	017	1.17	0.010
	TT p.s.	019	1.27	0.008
SS	7mm P0,0	012	1.07	0.009
	7mm P0,2	016	1.08	0.009
	7mm P0,6	013	1.23	0.011
	5mm P0,10	014	1.33	0.012
	5mm P0.14	018	1.36	0.012

Results of the measurements with smooth surface conditions are shown in Section 7.1 together with computations using the Navier-Stokes solver, EllipSys2D. The slope of the measured C_L, Figure 7-6, remains fairly constant until about $\alpha = 9°$ where separation is initiated. C_{Lmax} of about 1.37 is reached at $\alpha = 14°$. In the post stall area C_L is reduced smoothly indicating that separation occurs from the trailing edge and progressively approaches the leading edge. Above $\alpha = 20°$ most of the suction side is separated and deep stall is entered. The measurement of C_D shows a C_{Dmin} of around 0.008 and low C_D until separation occurs.

The measurements compare well with computations. Figure 7-2 to Figure 7-4 show the measured and computed C_p distributions for $\alpha = 4°$, 12° and 16°. At $\alpha = 4°$ good agreement between computations and measurements is obtained, only a slight deviation is observed at the trailing edge which is caused by an improper resolution of pressure tabs. At $\alpha = 12°$ the computations predict C_L slightly higher compared to measurements. This is caused by a delayed separation. No particular difference is seen between turbulent and transitional computations except at around $x/c = 0.05$ chord on the suction side, where transition from laminar to turbulent flow is calculated to take place. At $\alpha = 16°$ the computations predict C_L higher compared to measurements because of a delay in the separation, as it was the case at $\alpha = 12°$. No particular difference is seen between turbulent and transitional computations except at around $x/c = 0.02$ chord on the suction side, where transition from laminar to turbulent flow is calculated to take place.

The measured and the predicted C_{Dmin}, Figure 7-5, and the shape of the C_D curve at low angles of attack are both in fairly good agreement. The transitional computations result in lower drag due to the lower skin friction.

Measurements with Leading Edge Roughness (LER) using 90° zigzag tape at different positions are shown in Section 7.2. Three configurations are investigated: Roughness at $x/c = 0.05$ on the suction side and 0.10 on the

pressure side (0.05/0.10), roughness at the suction side (s.s.) of the leading edge and roughness at the pressure side (p.s.) of the leading edge.

Pressure distributions are shown at $\alpha = 4°$, 12° and 16° for the three different LER configurations compared with smooth measurements in Figure 7-7 to Figure 7-9. All pressure distributions show that LER at the very leading edge reduces the suction peak. At $\alpha = 16°$ LER at the very suction side leading edge reduces the suction peak significantly. For all angles of attack the placement of the LER at 0.05/010 does not have much influence since laminar separation takes place in front of $x/c = 0.05$ and because the suction peak is located upstream of $x/c = 0.05$. As seen in C_L and C_D, Figure 7-10, the LER at the very leading edge significantly affects the flow above $\alpha = 8°$ decreasing C_L and increasing C_D. Mounting the LER from the very leading edge towards the pressure side results in a significant decrease of C_L and increase of C_D since it is placed in front of the suction peak. However, the changes of C_L and C_D are much bigger if the LER is mounted from the very leading edge towards the suction side. Thus, placing LER in front of the suction peak results in large reduction of C_L and large increase of C_D.

In Section 7.3 different LER types at the pressure side of the leading edge are compared: 90° zigzag tape, 60° zigzag tape and trip tape with height 0.35 mm, 0.85 mm and 0.12 mm, respectively. Both pressure distributions, Figure 7-12 to Figure 7-14, and C_L and C_D, Figure 7-15, show that higher roughness elements result in lower C_L and higher C_D. Thus, 60° zigzag tape has the most severe influence with $C_{L,max} = 1.17$ and $C_{D,min} = 0.010$, while trip tape has the smallest effect with $C_{L,max} = 1.27$ and $C_{D,min} = 0.008$.

Measurements with stall strips (SS) mounted on the airfoil section are shown in Sections 7.4 and 7.5. Two different SS are placed at five different locations. Measurements with SS are compared to measurements on a smooth airfoil. Placing the SS close to the leading edge will significantly lower C_{Lmax} and the slope of the C_L curve, Figure 7-20. The measurements show that the aerodynamic characteristics change marginally when moving the SS from the very leading edge (P0,0) to the pressure side at the leading edge at $x/c = 0.0003$ (P0,2). Thus, $C_{L,max}$ increases from 1.07 to 1.08. From the pressure distributions, Figure 7-17 to Figure 7-19, it can be seen that the two different positions of the SS result in similar pressure distributions. Also, it can be seen that the shown suction peaks for $\alpha = 4°$, 12° and 16° is lowered significantly resulting in lower C_L and higher C_D. Moving the SS downstream on the pressure side the lift-drag polars will approach the smooth curve, Figure 7-25. Mounting the SS at $x/c = 0.008$ at the pressure side will affect the airfoil characteristics, resulting in lower C_L and higher C_D compared to a smooth airfoil. In this case $C_{L,max} = 1.23$ and $C_{D,min} = 0.011$. If the SS are mounted at $x/c = 0.023$ and 0.045 at the pressure side, the airfoil characteristics only change marginally compared to a smooth airfoil.

Section 7.6 describes dynamic stall measurements. Below $C_{L,max}$, Figure 7-27, the hysteresis loops are seen to be small while the loops are significantly open above $C_{L,max}$. Just at and above $C_{L,max}$ the slopes of the loops is positive while the slope of the polar is zero or negative. However, in deep stall the slopes of both loops and polar are comparable. It should be noted that there is an offset for some of the loops compared to the mean polar. This is due to calibration uncertainties. Figure 7-28 to Figure 7-30 show the hysteresis loops in detail for C_L, C_D and C_M, respectively. The arrows in the figures show the directions.

Clockwise loops are illustrated by right arrows and anti-clockwise loops by left arrows.

Section 7.7 describes the stall characteristics measurements. Standard deviations for geometrical α, C_L and C_D as function of α, Figure 7-31 to Figure 7-33 left side, show that the standard deviation increases significantly around $\alpha = 15°$. It is also seen that the standard deviation for C_L and C_D has a maximum around $\alpha = 20°$. Selected probability density functions of geometrical α, C_L and C_D, Figure 7-31 to Figure 7-33 right side, illustrate how the measured values are distributed. It is seen how the distribution for both geometrical α, C_L and C_D become lower and wider until $\alpha = 20°$, indicating that the flow becomes more fluctuating for increasing α. Time series of C_L and C_D at $\alpha = 20.6°$ are seen in Figure 7-34 and Figure 7-35. No double stall is observed.

9.3 Comparison

Comparisons of measurements of the NACA 63-415 airfoil and the NACA 63-415-Risø-D airfoil are shown in chapter 8.

Measurements on the airfoils with smooth surfaces are shown in section 8.1. Some differences both in the pressure distributions and in C_L and C_D are seen. The pressure distributions at $\alpha = 4°$, 12° and 16°, Figure 8-1 to Figure 8-3, show minor differences. For the NACA 63-415-Risø-D at $\alpha = 4°$ pressure builds up slower with a wider suction peak. At $\alpha = 12°$ and 16° the suction pressure is slightly higher for the NACA 63-415-Risø-D airfoil except for the suction peak which is lower. C_L and C_D are shown in Figure 8-4. It is seen that C_L is higher and C_D is lower for $\alpha > 6°$ for the NACA 63-415-Risø-D airfoil compared to the original airfoil. This might be due to a delay in the generation of a laminar separation bubble at the leading edge on the NACA 63-415-Risø-D airfoil. This was one of the objectives in the design of the airfoil. For $\alpha > 20°$ a lower C_D for the NACA 63-415-Risø-D airfoil is observed, Figure 8-5. This is due to more stable stall conditions which was the primary design objective of the modified airfoil. In the interpretation of C_L and C_D it is important to note that the coefficients are based on the same chord, $c = 600$ mm, even though the chord for NACA 63-415-Risø-D airfoil was $c = 606$ mm. Thus, a reduction of 1% of C_L and C_D would be the result if a chord of $c = 606$ mm was used instead of $c = 600$ mm.

The normalised rotor driving force for a wind turbine, C_T, for both airfoils is shown in Figure 8-6. Maximum C_T increases from 0.26 to 0.29 for the modified airfoil, which is an increase of around 10 %. C_T for the NACA 63-415-Risø-D airfoil is higher at all angles of attack compared to the NACA 63-415 airfoil. The normalised force normal to the rotor plane for a wind turbine, C_N, for both airfoils is shown in Figure 8-7. Maximum C_N increases from 1.31 to 1.35 for the modified airfoil, which is an increase of around 3 %. C_N for the NACA 63-415-Risø-D airfoil is higher from $\alpha = 6°$ to $\alpha = 20°$ compared to the NACA 63-415 airfoil. For $\alpha > 20°$ C_N for the modified airfoil is lower.

Measurements with leading edge roughness (LER) are seen in section 8.2. C_L and C_D for airfoils with 90° zigzag tape with 0.35 mm thickness mounted at x/c = 0.05 and 0.10 on the suction side and pressure side, respectively, are shown in Figure 8-8. As it was the case for the airfoils with smooth surfaces C_L is higher and C_D is lower for the modified airfoil for $\alpha > 6°$. This is probably due to a

delay in a laminar separation bubble at the leading edge since the zigzag tape is mounted downstream of the suction peak and the location at which transition from laminar to turbulent flow takes place. Thus, this kind of LER has practically no influence on the aerodynamic characteristics.

In Figure 8-10 C_L and C_D are seen for airfoils with 90° zigzag tape of 0.35 mm thickness mounted from the leading edge towards the suction side. C_L is higher and C_D is lower for the modified airfoil for $\alpha > 0°$ probably caused by a wider suction peak. For $\alpha > 15°$ C_L is lower and C_D is higher for the modified airfoil. This is also reflected in Figure 8-11 where C_T is seen. C_T for the modified airfoil is higher until $\alpha = 15°$. Above $\alpha = 15°$ it is lower compared to the NACA 63-415 airfoil. Thus, with LER on the leading edge suction side the modified airfoil was partially improved compared to the NACA 63-415 airfoil.

If the same zigzag tape is mounted from the leading edge towards the pressure side C_L is higher for $\alpha > 7°$ and C_D is lower for $\alpha > 6°$ for the modified airfoil, Figure 8-12. The improvement is significant since maximum C_T has increased from 0.17 to 0.24, Figure 8-13, i.e., an increase of around 40 %. The increase is even higher in deep stall.

If trip tape of 0.12 mm thickness is mounted at the same location at the leading edge pressure side the difference is small as seen in Figure 8-14. From $\alpha > 4°$ C_L is slightly higher and C_D is slightly lower for the modified airfoil compared to the NACA 63-415 airfoil. In deep stall the higher level of C_L is more significant.

If 60° zigzag tape with 0.85 mm thickness is mounted at the same location at the leading edge pressure side the difference is even bigger than found using 90° zigzag tape. This is seen in Figure 8-15 where C_L is higher and C_D is lower for $\alpha > 5°$ for the modified airfoil.

Thus, for wind turbines exposed to LER the influence on the power and especially the peak power will vary depending on the height and the location of the LER. Increasing roughness thickness seems to result in decreasing power. If roughness accumulates on the pressure side the modified airfoil is much more resistant to LER than the original NACA 63-415 airfoil.

Comparing dynamic stall for the NACA 63-415 and the NACA 63-415-Risø-D airfoil no significant differences appear in the loops for C_L as shown in Figure 8-16. However, the loops for C_D shown in Figure 8-17 reflect some differences. The loops around $\alpha = 16°$ have different directions and the slope for the modified airfoil is somewhat steeper. For the loops around $\alpha = 18°$ the slope is slightly steeper as well for the modified airfoil and the loop is slightly more open too. A much more open loop for the modified airfoil is also the case for the loops around $\alpha = 21°$, but in this case the slope is slightly less steep for the modified airfoil. Dynamic stall loops for C_M are seen in Figure 8-18. Here some differences occur around $\alpha = 18°$ and 21° where the loop for the modified airfoil is slightly more open. Except for the mentioned loops the airfoils have the same dynamic stall characteristics.

Differences in stall characteristics are seen in Figure 8-19 to Figure 8-21 where the standard deviation of geometrical α, C_L and C_D is seen. The most significant difference is seen for $\alpha > 18°$. Maximum standard deviation for C_L is lower from around 0.15 for the NACA 63-415 airfoil to 0.13 for the modified airfoil,

a decrease of 13 %. The maximum moves from around $\alpha = 22°$ to $\alpha = 20°$. For $\alpha < 20°$ the standard deviation for C_L is similar for the two airfoils. This is also the case for the standard deviation for C_D where the maximum standard deviation is reduced from 0.065 to 0.039, which is a reduction of 40 %. The maximum moves from 21° for the NACA 63-415 airfoil to 18° for the modified airfoil. This significant decrease is due to double stall from around $\alpha = 20°$ on the NACA 63-415 airfoil. This is not present for the NACA 63-415-Risø-D airfoil. Minor differences are seen for lower angles of attack where the standard deviations for the modified airfoil compared to the NACA 63-415 airfoil is slightly higher until $\alpha = 15°$ and is lower for α above 15°.

10 Conclusions

This report describes 2D measurements on the NACA 63-415 airfoil and a modified NACA 63-415 airfoil, also called NACA 63-415-Risø-D. The NACA 63-415 airfoil is designed for use on aeroplanes but it is also used for wind turbines. Since double stall is observed on this airfoil and since it has showed sensitivity to leading edge roughness a modification of the leading edge has been designed with operational Reynolds numbers around 3.0 million. With the modification double stall should be avoided and the airfoil should be more insensitive to leading edge roughness. Furthermore, the lift-drag ratio just before stall should be improved.

To address the agreement between the design characteristics and the actual airfoil performance the NACA 63-415 and the NACA 63-415-Risø-D airfoil were tested in a wind tunnel. The testing conditions corresponded to the maximum flow velocity of 45 m/s giving a Reynolds number of, $Re = 1.6 \times 10^6$ compared with the design Reynolds numbers around $Re = 3.0 \times 10^6$. The tunnel has a background turbulence level of 1 %.

For smooth surface conditions the modified airfoil had the expected characteristics compared to the NACA 63-415 airfoil. Higher lift-drag ratio was observed from $\alpha = 6°$. At $\alpha = 8°$ the lift-drag ratio increased from 67 to 72. Furthermore, no double stall was observed in contrast to the NACA 63-415 airfoil. The maximum lift coefficient for the modified airfoil was increased from 1.33 to 1.37. The minimum drag coefficient was 0.008 for both airfoils.

Tests on the airfoil sections mounted with 90° zigzag tape of 0.35 mm thickness to simulate leading edge roughness showed that if the zigzag tape was mounted at 5 % and 10 % chord length at the suction side and pressure side, respectively, only very little influence was observed compared to smooth airfoils. Thus, better ways to simulate leading edge roughness should be used.

Mounting the airfoil sections with the 90° zigzag tape located on the pressure side leading edge showed that the modified airfoil had significantly improved the roughness insensitivity. The maximum lift coefficient for the modified airfoil was increased from 1.10 to 1.21. The minimum drag coefficient was 0.010 for both airfoils. In terms of the maximum driving force coefficient of a wind turbine rotor the modified airfoil was improved from 0.17 to 0.24, which is an increase of 40 %.

If the 90° zigzag tape was located on the suction side leading edge the improvement in airfoil characteristics were smaller. The maximum lift coefficient for the modified airfoil was 1.16 compared with 1.11 for the original airfoil. The minimum drag coefficient was 0.011 for both airfoils. In terms of the maximum driving force coefficient of a wind turbine rotor the modification improved the airfoil from 0.19 to 0.20, i.e. an increase of 5 %. However, the coefficient became lower for the modified airfoil than for the NACA 63-415 airfoil for angles of attack above 15°.

Dynamic stall experiments showed only small differences between the two airfoils. At 16°, 18° and 20° angles of attack the slope of the loops and the opening of the loops changed slightly for C_D and C_M. Furthermore, the directions of the loops changed for C_D at 16° and 20°. However, in general the dynamic stall characteristics for the two airfoils did not change.

Static stall characteristics measured with fixed angle of attack improved for the modified airfoil compared to the NACA 63-415 airfoil. Lower standard deviations for both C_L and C_D was observed in stall indicating smoother and more stable stall conditions for the modified airfoil. These flow conditions are connected to double stall which was avoided for the modified airfoil.

Mounting of stall strips on the NACA 63-415 airfoil showed that the biggest reduction in maximum lift and the biggest increase in minimum drag were obtained if the stall strips were located around the very leading edge. Locating the stall strips at the stagnation point for -2° angles of attack most significantly affected the aerodynamic coefficients. Maximum lift was decreased from 1.33 to 1.00 and minimum drag increased from 0.008 to 0.010.

For stall strip locations at stagnation point for 0° and 2° angles of attack the influence from stall strips was still big, but not as big as if the stall strips were mounted at the stagnation point at -2° angles of attack. Thus, the airfoil characteristics had a strong dependency of the exact location of the stall strips at the leading edge. A minor influence was seen if stall strips were mounted at the stagnation point for 6° angles of attack. The stall strips could be neglected when located at the stagnation point for 10° angles of attack and above if only positive angles of attack were considered.

Vortex generators mounted at 20 % chord length at the suction side of the NACA 63-415 airfoil showed a significant increase of $C_{L,max}$ from 1.33 at 13° angles of attack without vortex generators to 1.74 at 18° angles of attack with vortex generators. Using vortex generators $C_{L,max}$ was followed by an abrupt loss of C_L, so that C_L for the airfoil with and without vortex generators was similar for angles of attack above 20°. Furthermore, the presence of the vortex generators increased the minimum drag from 0.008 without vortex generators to 0.017 with vortex generators.

References

[1] Abbott, I.H, and Doenhoff, E.v., 'Theory of Wing Sections', Dover Publications, Inc., New York (1959)

[2] Fuglsang, P., Bak, C., ' Modification of the NACA 63-415 leading edge to avoid double stall', Proc. of the 13th IEA Symposium on the Aerodynamics of Wind Turbines, Stockholm, Sweden (1999).

[3] Fuglsang, P., Antoniou, I., Sørensen, N.N., Madsen, H. Aa., 'Validation of a Wind Tunnel Testing Facility for Blade Surface Pressure Measurements.' Risø-R-981(EN), Risø National Laboratory, Denmark (1998)

[4] Rae Jr., W.H., Pope, A., 'Low-Speed Wind Tunnel Testing', SE, John Wiley & Sons, ISBN 0-471-87402-7. (1984).

[5] Brooks, T.F. and Marcolini, M.A., 'Airfoil Trailing Edge Flow Measurements and Comparison with Theory Incorporating Open Wind Tunnel Corrections', AIAA-84-2266, AIAA/NASA 9th Aeroacoustic Conference (1984).

[6] Hoerner, S.F. and Borst, H.V., 'Fluid-Dynamic Lift', Hoerner Fluid Dynamics, P.O. Box 342, Brick Town, N.J. 08723, USA (1975).

[7] Timmer, W.A., 'The design and testing of airfoil DU 91-W2-250', Proc. IEA Joint Action. Aerodynamics of Wind Turbines. 6th Symposium (1992).

[8] Sørensen, N.N., 'General Purpose Flow Solver Applied to Flow over Hills', Risø-R-827(EN), Risø National Laboratory, Denmark (1995).

[9] Menter, F.R., 'Zonal Two Equation k-ω Turbulence Models for Aerodynamic Flows', AIAA Paper 93-2906 (1993).

[10] Michel, R., 'Etude de la transition sur les profiles d'aile', ONERA Report 1/1578-A. See White F.M., Viscous fluid flow, p. 442 (1952).

[11] Bak, C., Madsen, H.A., Fuglsang, P., Rasmussen, F., 'Observations and Hypothesis of Double Stall', Wind Energy, **2**, 195-210 (1999).

A   Measurement survey

This appendix describes the performed measurements in detail to make the measurements stored on CD available for subsequent exploitation. The different measurement types are described and the naming convention for the data files is explained. The format of the data files is given and each performed measurement is listed and described.

A.1   List of symbols

h	[cm]	Wake rake vertical position, positive toward floor, origin at wake rake top
k		Reduced frequency
p	[Pa]	Static pressure
p_o	[Pa]	Total pressure head
p_{atm}	[Pa]	Atmospheric pressure
q	[Pa]	Dynamic pressure
x		Airfoil chordwise co-ordinate relative to chord, positive toward trailing edge, origin at leading edge
y		Airfoil vertical co-ordinate relative to chord, positive toward ceiling, origin at leading edge
A	[°]	Pitch motion amplitude
C_D		Drag coefficient
C_L		Lift coefficient
C_M		Moment coefficient
C_P		Airfoil pressure coefficient
Re		Reynolds number
t	[°C]	Air temperature
α	[°]	Angle of attack
ρ	[kg/m^3]	Air density
Subscripts		
c		Corrected value
p		Pressure measurement (opposite to wake rake measurement)
w		Wake rake measurement
∞		Reference for normalisation of airfoil forces

A.2   Measurement types

There are four different basic types of measurements of the airfoil flow as shown in Table A-1:
- STEP
- CONT
- STAT
- PITCH

Table A-1 Overview of the different types of measurements that have been performed.

STEP
The lift, drag and moment polar versus angle of attack.
• Discrete measurements at different angles of attack. • Angle of attack range: -6° to 35°. • Interval between different angles: 1° to 4°. • Time series length: 20 s. • Sampling frequency: 5 Hz.
CONT
The lift, drag and moment polar versus angle of attack. (shorter measurement time compared to 'STEP')
• Continuous measurements at different angles of attack. • Angle of attack range: -6° to 35°. • Rate of change of angle of attack: 0.1°/s to 0.5°/s (manually changed). • Time series length app: 250 s. • Sampling frequency: 50 Hz.
STAT
Time series of airfoil flow at different angles of attack, usually in stall.
• Stationary measurements at different angles of attack. • Time series length: 60 s and 180 s. • Sampling frequency: 100 Hz.
PITCH
Time series of unsteady airfoil flow from pitching motion for determination of hysteresis loops for lift, drag and moment at different pitching frequencies and amplitudes.
• Dynamic measurements at different mean angles of attack with the airfoil in pitching motion. • Pitching amplitude: 2° • Reduced frequency: 0.09 • Time series length: 30s. • Sampling frequency: 100 Hz.

The following table contains a list of all the data files that are available for each type of measurement. A detailed description of the data files is given in Section A.4.

Table A-2 Overview of the available data files for each measurement type.

STEP	
rxx.pol	Average general results where the average of each sub measurement is written in rows, Table A-4. Well suited to obtain C_L and C_D versus α.
cp.pol	Average C_P distributions where the average of each sub measurement is written in columns. Well suited to obtain C_P distributions at different angles of attack (from rxx.pol).
v_w.pol	Average wake rake velocity distributions where the average of each sub measurement is written in columns.
rxx-5hz.nnn	Raw data as rows in general data file with frames of 5 Hz, Table A-4.
cp-5hz.nnn	C_P distribution in columns with frames of 5 Hz.
v_w-5hz.nnn	Wake velocity distribution in columns with frames of 5 Hz.
CONT	
rxx.bin	Average results where raw data are sorted in bins of the angle of attack, Table A-6. Well suited to obtain C_L, C_D and C_M versus α.
rxx.pol	Raw data as rows in general data file with frames of 50 Hz. First 15 columns of data file described in Table A-4. All sub measurements are merged together in one file
rxx-1hz.nnn	Raw data as rows in general data file reduced to frames of 1 Hz, Table A-4.
rxx-10hz.nnn	Raw data as rows in general data file reduced to frames of 10 Hz, Table A-4.
rxx-50hz.nnn	Raw data as rows in general data file with frames of 50 Hz, Table A-4.
cp-1hz.nnn	C_P distribution in columns reduced to frames of 1 Hz.
v_w-1hz.nnn	Wake velocity distribution in columns reduced to frames of 1 Hz.
STAT	
rxx.nnn	Raw data as rows in data file with frames of 50 Hz, Table A-5.
rxx-1hz.nnn	Raw data as rows in general data file reduced to frames of 1 Hz, Table A-4.
rxx-10hz.nnn	Raw data as rows in general data file reduced to frames of 10 Hz, Table A-4.
rxx-50hz.nnn	Raw data as rows in general data file with frames of 50 Hz, Table A-4.
cp-1hz.nnn	C_P distribution in columns reduced to frames of 1 Hz.
v_w-1hz.nnn	Wake velocity distribution in columns reduced to frames of 1 Hz.
PITCH	
rxx-loop.bin	Average results where raw data are sorted in bins of the phase angle of the hysteresis loop, Table A-7 Well suited to obtain hysteresis loops of C_L and C_D and C_M versus α.
rxx.nnn	Raw data as rows in data file with frames of 100 Hz, Table A-5.
rxx-100hz.nnn	Raw data as rows in general data file with frames of 100 Hz, Table A-4.

Where
- xx is the measurement run number
- yy is the frame resolution in Hz
- nnn is the sub measurement number

A.3   Data file naming convention

The different data files are stored in the following directory structure:
- The name of the airfoil.
- The measurement run name.

The naming and the format of the data files is explained in Table A-3.

A.4   Data file formats

The different data files are shown in Table A-3.

Table A-3 Available data files.

pol-xxhz.nnn	
xx	Frame average frequency: 100, 50, 10, 5 or 1
nnn	measurement sub number
General data file with each measurement frame/average formatted in rows. The first two rows contain the column number and the sensor name. The format of the data files is described in Table A-4	
STEP	Measurements are given with 5 Hz frame resolution
CONT	Measurements are given with 50 Hz, 10 Hz and 1 Hz frame resolutions respectively
STAT	Measurements are given with 100 Hz, 10 Hz and 1 Hz frame resolutions respectively
PITCH	Measurements are given with 100 Hz resolution

pol.nnn	
nnn	measurement sub number
Raw data file with each measurement frame/average formatted in rows. The first two rows contain the column number and the sensor name. The format of the data files is described in Table A-5.	
PITCH	Measurements are given with 100 Hz frame resolution

pol.dat	
General data file with overall average values of each sub measurement formatted in rows, as above. All sub measurement for a given measurement run are assembled into one single file. The format of the data files is described in Table A-4.	
STEP	Measurements are given with a 20 s average value for each sub measurement
PITCH	Measurements are given with a 30 s average value for each sub measurement
STAT	Measurements are given with a 60 s or 180 s average value for each sub measurement

pol.dat	
General data file with each measurement frame formatted in rows, as above. All sub measurement for a given measurement run are assembled into one single file. The format of the data files is described in Table A-4, but the files contain only the first 15 collumns.	
CONT	Measurements are given with 50 Hz resolution, only column 1 to 15.

pol.bin	
Post processed data file where the frames from all sub measurements are sorted in bins of the angle of attack to obtain the polar curves. The format of the data files is described in Table A-6.	
CONT	Measurements where the 50 Hz frames from all sub measurements are sorted in bins of α_c. The angle of attack range is divided into 30 bins.

loop.nnn	
nnn	Measurement sub number
Post processed data file where the frames from all sub measurements are sorted in bins of the phase of the hysteresis loop. The format of the data files is described in Table A-7.	
PITCH	Measurements where the 100 Hz frams from all sub measurements are sorted in bins of the phase of the hysteresis loop. The phase range is divided into 30 bins.

cp-yyhz.nnn	
yy	Frame average frequency: 5 or 1
nnn	measurement sub number
Data file with each frame/average formatted in columns. The first column contains the x-coordinates of the pressure tabs. The subsequent columns contain the C_P distributions for the different frames. The angle of attack for the frames can be found in the corresponding, rxx-yyhz.nnn file.	
CONT	Measurements are given with 1 Hz frame resolution
STAT	Measurements are given with 1 Hz frame resolution
PITCH	Measurements are given with 100 Hz frame resolution

cp.dat	
Data file with each average formatted in columns. The first column contains the x-coordinates of the pressure tabs. The subsequent columns contain the average C_P distributions for each sub measurement. The angle of attack for the frames can be found in the corresponding, rxx.pol file.	
STEP	Measurements are given as 20 s average values

v_w-yyhz.nnn	
yy	Frame average frequency: 5 or 1
nnn	measurement sub number
Data file with each frame/average formatted in columns. The first column contains the coordinates of the wake rake total pressure tabs. The subsequent columns contain the wake rake velocity for the different frames. The angle of attack for the frames can be found in the corresponding, rxx-yyhz.nnn file.	
CONT	Measurements are given with 1 Hz frame resolution
STAT	Measurements are given with 1 Hz frame resolution

v_w.dat	
Data file with each average formatted in columns. The first column contains the coordinates of the wake rake total pressure tabs. The subsequent columns contain the average wake rake velocity distributions for each sub measurement. The angle of attack for the frames can be found in the corresponding, rxx.pol file.	
STEP	Measurements are given as 20 s average values

Table A-4 The content of the columns in the general data file.

Col.	Symbol	Sensor	Unit	Description
1	α_c	αc	°	Corrected angle of attack
2	C_L	cl	-	Lift coefficient (pressure)
3	C_{Dc}	cdc	-	Corrected drag coefficient (wake rake + pressure)
4	C_{Mc}	cmc	-	Corrected moment coefficient (pressure)
5	C_{Dpc}	cdpc	-	Corrected drag coefficient (pressure)
6[*]	C_{Dw}	cdw		Drag coefficient (wake rake)
7	α	α	°	Raw angle of attack
8	C_D	cd	-	Raw drag coefficient (wake rake + pressure)
9	C_{Dp}	cdp		Raw drag coefficient (pressure)
10	C_M	cm	-	Raw moment coefficient (pressure)
11	Re	re		Free stream Reynolds Number
12	q_∞	qref	Pa	Free stream dynamic pressure
13	p_∞	ps,ref	Pa	Free stream static pressure
14	T	t	°	Tunnel temperature
15	p_{atm}	patm	mBar	Atmospheric pressure
16-71[**]	C_P	cp(x)		Pressure coefficients corresponding to the coordinates in top row
72-74	p_{1-3}	ps,Pitot()	Pa	Pitot tube static pressures
75-77	p_{o1-3}	pt,Pitot()	Pa	Pitot tube total pressures
78-82[*]	p_w	ps,wake	Pa	Wake rake static pressures corresponding to the coordinates in top row
83-136[*]	p_{ow}	pt,wake	Pa	Wake rake total pressures corresponding to the coordinates in top row

*) At the 'PITCH' type measurements, the wake rake was not used. C_{DW} was set to C_{DP} and p_w and p_{ow} were not written in the data files

**) In some measurements one or more of the airfoil pressure sensors were excluded because of unstable calibration or because the pressure hole was blocked by vortex generators or roughness elements. The corresponding column in the file was then removed and the number of subsequent sensors changed.

Table A-5 The content of the columns in the raw data files.

Col.	Symbol	Sensor	Unit	Description
1	t	t	s	Running time
2	α	α	°	Raw angle of attack
3	C_L	cl	-	Lift coefficient (pressure)
4	C_{Dpc}	cdc	-	Corrected drag coefficient (wake rake + pressure)
54	C_{Mc}	cmc	-	Corrected moment coefficient (pressure)
6	αc	aoa_c	-	Corrected angle of attack
7[*]	r	ramp	rad	Hysteresis loop phase angle

*) At the 'STAT' type measurements, the hysteresis loop phase angle was not used.

Table A-6 The content of the columns in the post processed data files sorted in bins of the angle of attack.

Col.	Symbol	Sensor	Unit	Description
1	α_c	αc	°	Corrected angle of attack
2	C_L	cl	-	Lift coefficient (pressure)
3	C_{Dc}	cdc	-	Corrected drag coefficient (wake rake + pressure)
4	C_{Mc}	cmc	-	Corrected moment coefficient (pressure)
5	C_{Dpc}	cdpc	-	Corrected drag coefficient (pressure)

Table A-7 The content of the columns in the post processed data files sorted in bins of the phase angle of the hysteresis loop.

Col.	Symbol	Sensor	Unit	Description
1	α_c	αc	°	Corrected angle of attack
2	C_L	cl	-	Lift coefficient (pressure)
3	C_{Dpc}	cdpc	-	Corrected drag coefficient (pressure)
4	C_{Mc}	cmc	-	Corrected moment coefficient (pressure)

A.5 Performed measurements

Table A-8 to Table A-10 contain a list of the performed measurements for the different airfoil sections.

Table A-8 Performed measurements for modified NACA 63-415

Run	Type	Surface conditions	Remarks
002	CONT	Smooth	
003	STEP	Smooth	
004	STAT	Smooth	
006	PITCH	Smooth	$k = 0.09$, $1.3° < A < 2.1°$
007	STAT	Smooth	
008	CONT	90° zigzag tape at x/c = 0.05 suction side and 0.10 pressure side	
009	CONT	90° zigzag tape from leading edge towards suction side	
010	CONT	90° zigzag tape from leading edge towards pressure side	
011	STAT	90° zigzag tape from leading edge towards pressure side	
012	CONT	Stall strip (7 mm) at the leading edge	
013	CONT	Stall strip (5 mm) at 6° stagnation point	
014	CONT	Stall strip (5 mm) at 10° stagnation point	
015	PITCH	Stall strip (5 mm) at 10° stagnation point	$k = 0.09$ $1.3° < A < 2.0°$
016	CONT	Stall strip (7 mm) at 2° stagnation point	
017	CONT	60° zigzag tape from leading edge towards pressure side	
018	CONT	Stall strip (5 mm) at 14° stagnation point	
019	CONT	Trip tape from leading edge towards pressure side	

Table A-9 Performed measurements for NACA 63-415

Run	Type	Surface conditions	Remarks
023	STEP	Smooth	
024	CONT	Smooth	
025	CONT	90° zigzag tape at x/c = 0.05 suction side and 0.10 pressure side	
027	CONT	90° zigzag tape from leading edge towards suction side	
028	CONT	90° zigzag tape from leading edge towards pressure side	
064	PITCH	Smooth	$k = 0.09$, $1.3° < A < 2.1°$
065	STAT	Smooth	
072	CONT	Vortex generators at $x/c = 0.20$ suction side	
085	CONT	Stall strip (7 mm) at the leading edge	
086	CONT	Stall strip (7 mm) at 2° stagnation point	
087	CONT	Stall strip (5 mm) at 6° stagnation point	
088	CONT	Stall strip (5 mm) at 14° stagnation point	
089	CONT	Stall strip (5 mm) at 10° stagnation point	
091	PITCH	Stall strip (5 mm) at 10° stagnation point	$k = 0.09$, $1.6° < A < 2.2°$
092	CONT	Trip tape from leading edge towards pressure side	
093	CONT	Stall strip (7 mm) at -2° stagnation point	
094	CONT	60° zigzag tape from leading edge towards pressure side	
095	STAT	60° zigzag tape from leading edge towards pressure side	
096	STAT	Smooth flow	

Wind Tunnel Tests of the NACA 63-415 and a Modified NACA 63-415 Airfoil

Christian Bak, Peter Fuglsang, Jeppe Johansen, Ioannis Antoniou

Abstract (max. 2000 characters)

This report contains 2D measurements of the NACA 63-415 and a NACA 63-415 airfoil with modified leading edge called NACA 63-415-Risø-D. The aerodynamic properties were derived from pressure measurements on the airfoil surface and in the wake. The VELUX open jet wind tunnel was used having a background turbulence intensity of 1%, an inlet flow velocity of 40 m/s which resulted in a Reynolds number of 1.6×10^6. The airfoil sections had a chord of 0.600 m and 0.606 m for NACA 63-415 and NACA 63-415-Risø-D, respectively. The span was 1.9 m and end plates were used to minimise 3D flow effects. The measurements comprised both static and dynamic inflow where dynamic inflow was obtained by pitching the airfoil in a harmonic motion. We tested the influence of leading edge roughness, stall strips and vortex generators.

For smooth surface conditions the modified airfoil showed an increase in lift-drag ratio before stall at α=8° from 67 to 72. Furthermore, the maximum lift increased from 1.33 to 1.37 while the minimum drag was maintained. Double stall was observed on the NACA 63-415 airfoil, but not on the modified airfoil. This was reflected in the standard deviation of both lift and drag in stall which was significantly lower for the modified airfoil indicating smooth and stable stall conditions. No significant differences were observed for dynamic stall. Test on both airfoil sections with zigzag tape at the leading edge towards the pressure side showed that the insensitivity to roughness was improved significantly for the modified airfoil. However, if zigzag tape was mounted at the leading edge towards the suction side less improvement was observed. Mounting of stall strips at and near the leading edge showed that only if they were mounted at the very vicinity of the leading edge the airfoil characteristics were affected significantly. If the stall strips were mounted on the pressure side downstream of approximately 1 % chord length only little influence was seen for positive angles of attack.

Descriptors INIS/EDB

AERODYNAMICS; AIRFOILS; DRAG; STALL; TEST FACILITIES; TESTING; TURBINE BLADES; TURBULENT FLOW; TWO-DIMENSIONAL CALCULATIONS; WIND TUNNELS; WIND TURBINES